

Manufacturing, installation, commissioning, and first results with the 3D low-temperature co-fired ceramic high-frequency magnetic sensors on the Tokamak à Configuration Variable

Cite as: Rev. Sci. Instrum. **91**, 081401 (2020); <https://doi.org/10.1063/1.5115004>
Submitted: 17 June 2019 . Accepted: 21 July 2020 . Published Online: 13 August 2020

D. Testa , EUROfusion MST1 Team, and TCV Team



View Online



Export Citation



CrossMark

ARTICLES YOU MAY BE INTERESTED IN

[A new Collinear Apparatus for Laser Spectroscopy and Applied Science \(COALA\)](#)

Review of Scientific Instruments **91**, 081301 (2020); <https://doi.org/10.1063/5.0010903>

[An angle-scanned cryogenic Fabry-Pérot interferometer for far-infrared astronomy](#)

Review of Scientific Instruments **91**, 083108 (2020); <https://doi.org/10.1063/5.0012432>

[Design and performance of high-temperature furnace and cell holder for in situ spectroscopic, electrochemical, and radiolytic investigations of molten salts](#)

Review of Scientific Instruments **91**, 083105 (2020); <https://doi.org/10.1063/1.5140463>



Vacuum solutions from a single source

Pfeiffer Vacuum stands for innovative and custom vacuum solutions worldwide, technological perfection, competent advice and reliable service.

[Learn more!](#)



Manufacturing, installation, commissioning, and first results with the 3D low-temperature co-fired ceramic high-frequency magnetic sensors on the Tokamak à Configuration Variable

Cite as: Rev. Sci. Instrum. 91, 081401 (2020); doi: 10.1063/1.5115004

Submitted: 17 June 2019 • Accepted: 21 July 2020 •

Published Online: 13 August 2020



View Online



Export Citation



CrossMark

D. Testa,^{a)}  EUROfusion MST1 Team,^{b)} and TCV Team^{c)}

AFFILIATIONS

Ecole Polytechnique Fédérale de Lausanne (EPFL), Swiss Plasma Center (SPC), CH-1015 Lausanne, Switzerland

^{a)} Author to whom correspondence should be addressed: duccio.testa@epfl.ch

^{b)} See the author list of H. Meyer *et al.*, "Overview of progress in European Medium Sized Tokamaks toward an integrated plasma-edge/wall solution," Nucl. Fusion **57**, 102014 (2017).

^{c)} See the author list of S. Coda *et al.*, "Overview of the TCV tokamak program: Scientific progress and facility upgrades," Nucl. Fusion **57**, 102011 (2017).

ABSTRACT

Innovative high-frequency magnetic sensors have been designed and manufactured in-house for installation on the Tokamak à Configuration Variable (TCV), which are now routinely operational during the TCV experimental campaigns. These sensors combine the Low Temperature Co-fired Ceramic (LTCC) and the classical thick-film technologies and are in various aspects similar to the majority of the in-vessel inductive magnetic sensors foreseen for ITER (around 450 out of the 505 currently being procured are of the LTCC-1D type). The TCV LTCC-3D magnetic sensors provide measurements in the frequency range up to 1 MHz of the perturbations to the wall-aligned toroidal (δB_{TOR}), vertical (δB_{VER}), and radial (δB_{RAD}) magnetic field components. Knowledge of the equilibrium at the last closed flux-surface allows us to then obtain the field-aligned parallel ($\delta B_{\text{PAR}} \sim \delta B_{\text{TOR}}$), poloidal (δB_{POL}), and normal (δB_{NOR}) components, the latter being in most cases rather different from the vertical and radial components, respectively. The main design principles were aimed at increasing the effective area and reducing the self-inductance of the sensor in each of the three measurement axes, which are centered at the same position on each sensor, while reducing the mutual and parasitic coupling between them by optimizing the on-board wiring. The physics requirements are set by the installation of two high-power/high-energy neutral beam injection systems on TCV, i.e., studying fast ions physics, coherent instabilities, and turbulence in the (super-)Alfvénic frequency range. In this paper, we report the manufacturing, installation, and commissioning work for these high-frequency LTCC-3D magnetic sensors and conclude with an overview of illustrative experimental results obtained with this system. The LTCC-3D data provide new insights into the δB_{POL} coherent (eigenmodes, up to ~ 400 kHz) and in-coherent background turbulent fluctuations in the higher frequency range up to ~ 1 MHz, which were not previously available with the TCV Mirnov sensors. Furthermore, the LTCC-3D δB_{POL} measurements allow us to cross-check the data obtained with the standard Mirnov coils and have led to the identification of large electromagnetic (EM) noise pick-up for the Mirnov data acquisition (DAQ). When the sources of EM noise pick-up on the Mirnov DAQ are removed, the LTCC-3D data for δB_{POL} are in good overall agreement, i.e., within the expected measurement uncertainties, with those obtained with the standard Mirnov sensors located at the same poloidal position in the frequency range where the respective data acquisition overlap, routinely up to 125 kHz and up to 250 kHz in some discharges. The LTCC-3D δB_{PAR} measurements (not previously available in TCV or elsewhere) provide evidence that certain instabilities have a finite parallel δB at the wall, hence at the LCFS, consistent with the recent theoretical results for pressure-driven modes. The LTCC-3D δB_{NOR} measurements improve significantly on the corresponding measurements with the saddle loops, which are mounted onto the wall and have a bandwidth of ~ 3 kHz (due to the wall penetration time). A detailed end-to-end system modeling tool has been developed and applied to test on the simulated data the actual measurement capabilities of this new diagnostic system and obtain the ensuing estimates of the intrinsic measurement uncertainties. A detailed error

analysis is then performed so that, finally, fully calibrated, absolute measurements of the frequency-dependent amplitude and spectral breaks of coherent eigenmodes and in-coherent broadband magnetic fluctuations are provided for the first time in physical units with quantitative uncertainties.

© 2020 Author(s). All article content, except where otherwise noted, is licensed under a Creative Commons Attribution (CC BY) license (<http://creativecommons.org/licenses/by/4.0/>). <https://doi.org/10.1063/1.5115004>

I. INTRODUCTION

The Low-Temperature Co-fired Ceramic (LTCC) technology is a well-known industry standard widely used in harsh environmental conditions, such as high-temperature, high-vacuum, and high-radiation, covering a large spectrum of applications.¹ Based on the prototyping work performed mostly in-house at the Ecole Polytechnique Fédérale de Lausanne (EPFL)^{2–6} that started in 2007, the majority of the ITER in-vessel inductive magnetic sensors (around 450 out of 505⁷) currently being procured are of the LTCC-1D technology. Various examples of LTCC magnetic sensors have been designed and manufactured at the EPFL during the course of this 10-year project. Concurrently with the design and prototyping work for ITER and the work, described here, for our in-house Tokamak à Configuration Variable (TCV),⁸ LTCC sensors have already been produced by EPFL for installation, and are currently operational, in different tokamaks, namely, LTCC-1D sensors in FTU (Frascati, Italy⁹) and LTCC-2D sensors in WEST (Cadarache, France¹⁰). These ex-house activities will be reported in a separate publication. Additionally, LTCC-1D sensors of our design are also being currently considered for installation in the Divertor Test Tokamak facility¹¹ and in a prototype compact tokamak facility that is being developed by Tokamak Energy Ltd., a private UK company,¹² and by the European Space Agency for installation on micro-satellites.¹³ Moreover, in the framework of a testing program for DEMO,¹⁴ LTCC-1D and LTCC-3D sensors manufactured in-house are currently being prepared for shipment to the Compass-U facility (Praha, Czech Republic), and design activities have recently started with the purpose of producing a fully integrated multi-dimensional LTCC + Hall sensor.

Innovative LTCC-3D high-frequency (HF) magnetic sensors have been designed and manufactured in-house, were installed, and are currently operational for the TCV experimental campaigns. An initial reporting of the manufacturing work for these sensors was presented at the 2014 Symposium on Fusion Technology and in the ensuing paper published in Fusion Engineering and Design.¹⁵ A further report on this work was then presented at the 2018 Symposium on Fusion Technology and in the ensuing paper published in Fusion Engineering and Design,¹⁶ with the primary focus being on the lessons learnt for ITER. These two earlier contributions provide a starting point for some aspects of this presentation, which provides extended details of the actual installation and commissioning of this diagnostic system and a selection of some illustrative results.

The TCV LTCC-3D sensors are mounted on the inside of the vacuum wall and, when considering the toroidal coordinate system (\mathbf{e}_ϕ , \mathbf{e}_z , \mathbf{e}_r), provide measurements of the perturbation to the toroidal ($\delta B_{\text{TOR}}||\mathbf{e}_\phi$), vertical ($\delta B_{\text{VER}}||\mathbf{e}_z$), and radial ($\delta B_{\text{RAD}}||\mathbf{e}_r$) magnetic field components in the frequency range up to 1 MHz, the data acquisition (DAQ) sampling frequency being 2 MHz.

Figure 1 shows the position of the LTCC-3D sensor with respect to the wall and the ex-vessel coils of TCV, also providing a geometrical overview of the TCV convention for the toroidal coordinate system.

Knowledge of the equilibrium topology at the Last Closed Flux Surface (LCFS) allows us to transform the geometrical, wall-aligned measurements into the corresponding field-aligned ones ($\mathbf{e}_||$, \mathbf{e}_θ , \mathbf{e}_p), namely, the parallel ($\delta B_{\text{PAR}}||\mathbf{e}_||$), poloidal ($\delta B_{\text{POL}}||\mathbf{e}_\theta$), and normal ($\delta B_{\text{NOR}}||\mathbf{e}_p$) components.⁵³ To optimize the volume occupation in-vessel for the desired effective area and self-inductance, the sensors are based on combining the LTCC and the classical thick-film technologies. The design constraints are set by the measurement and installation requirements.

The scientific objective is the study of fast ions, MHD, and magnetic turbulence physics in the presence of a population of supra-thermal ions due to the high-power/high-energy Neutral Beam Injection (NBI) on TCV.¹⁷ Magnetic perturbations with (super-)Alfvénic frequencies >100 kHz and covering a spectrum in the perpendicular wavenumber k_\perp extending upwards of $k_\perp \rho_{\text{FAST}} > 0.1$, where ρ_{FAST} is the Larmor radius of the fast ions, should

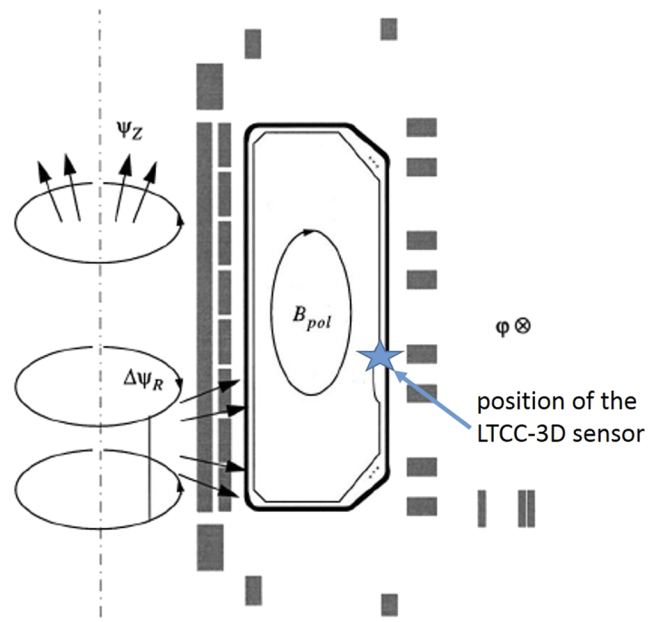


FIG. 1. The position of the LTCC-3D sensor with respect to the wall and the ex-vessel coils of TCV (multiple gray rectangular boxes), also providing a geometrical overview of the TCV convention for the toroidal coordinate system in terms of the magnetic field B_{POL} and the vertical (ψ_z) and the radial ($\Delta\psi_r$) fluxes.

be detectable. The Mirnov sensors currently installed on TCV for measuring δB_{POL} have a bandwidth of around 90 kHz,¹⁸ which is, however, reduced to ~ 50 kHz due to a much deteriorating Common Mode Rejection Ratio (CMRR) and pick-up of EM noise from various ex-vessel sources. These Mirnov sensors are then not well-suited for these high-frequency, high- k_{\perp} measurements and additionally do not provide measurements of δB_{TOR} or δB_{RAD} . Similarly, the saddle loops currently installed on TCV for measuring δB_{RAD} have a bandwidth of around 3 kHz,¹⁸ as the loops are mounted directly on the TCV metal vacuum vessel.

For the installation requirements, the planar size of the LTCC-3D sensor is limited to $[7 \times 7] \text{ cm}^2$ (the TCV Mirnov sensors have a planar size of $\sim [3.6 \times 3.8] \text{ cm}^2$), while its depth must remain under 1 cm (as per the Mirnov sensors) to fit between the protection tiles and the vacuum vessel. Furthermore, the 3D measurement axes are intended to be centered at the same position on each sensor for simplicity in the data interpretation.

Three LTCC-3D sensors have been installed at the same vertical position but in different and not equi-spaced toroidal sectors to provide the same measurements at different toroidal locations so that analysis of these data provides information on possible toroidal asymmetries in the fluctuating spectra. Due to installation constraints, the sensors are located on the Low-Field Side (LFS) of TCV and sit at the vertical position $Z = Z_{GEO} - 115 \text{ mm}$, where $Z_{GEO} = 0$ is the tokamak's geometric center. This is optimal for two of the three most used TCV plasmas, which have a vertical position of the magnetic axis $Z_{MAG} = [Z_{GEO}, Z_{GEO} - 230 \text{ mm}]$, but limits the detection capabilities for the plasmas centered at $Z_{MAG} = Z_{GEO} + 230 \text{ mm}$ and does not allow the comparison of these 3D measurements of the fluctuating magnetic fields on the LFS and High-Field Side (HFS), preventing characterizing their high-frequency, high- k_{\perp} spectral components as ballooning or anti-ballooning (this can be done for the lower-frequency, hence low- k_{\perp} spectral components of δB_{POL} using the Mirnov sensors that cover the entire poloidal cross section on four different toroidal sectors). Finally, when combining the LTCC and the Mirnov δB_{POL} measurements and using a spatial signal decomposition based on the *Sparse Representation of Signals* (SRS) (the so-called *SparSpec* code¹⁹), the resolution in toroidal mode numbers (n) on the LFS of TCV is extended to $|n| \sim 30$ (not spatially Nyquist limited) from a maximum $|n| \leq 8$ (spatially Nyquist limited, as we have 16 equi-spaced + 1 not equi-spaced sensors) when using only the Mirnov data. Note that in the following, when {toroidal, poloidal} mode numbers are quoted for any measured mode, these have been always determined using the *SparSpec* code.

For each individual measurement axis, the design principles aim at increasing the effective area NA_{EFF} while reducing the self-inductance L_{SELF} and the *parasitic* and *mutual*⁵⁴ coupling between the different axes. The target requirements for the three measurement axes are $NA_{EFF} > 200 \text{ cm}^2$ (i.e., at least twice as much the effective area of the Mirnov sensors to improve the detection of the higher frequency components) and an end-to-end (i.e., including the sensor and all the cabling up to the front-end electronics) resonant frequency $\omega_{RES}/2\pi > 1 \text{ MHz}$ (above the resonance, there is a well-known drastic reduction in the measurement sensitivity). As the total length of the cabling (in-vessel + ex-vessel) is such that its capacitance C_{CABLE} by far exceeds the sensor's self-capacitance C_{SELF} , we have that $\omega_{RES} \sim 1/(L_{SELF}C_{CABLE})^{1/2}$. An optimization

algorithm for $\{L_{SELF}, NA_{EFF}\}$ is used for the design of these LTCC-3D sensors based on that previously developed for the LTCC-1D sensors.⁶ This algorithm maximizes NA_{EFF} while minimizing L_{SELF} using an iteration on the winding patterns, namely, on the number of *layers* and the number of *turns* per layer (see Sec. II for the definition of these two terms). The δB_{RAD} measurement is then obtained through a single planar coil on an alumina base substrate, while the δB_{TOR} and δB_{VER} measurements are obtained by arraying in a balanced, centered, four-quadrant series 2 groups of $10 \times$ identical multilayer LTCC-1D modules with coils perpendicular to the alumina base for each of these measurements.

While it is expected that higher frequency modes will be excited in TCV when a second, higher-energy NBI source will be installed (tentatively within the next couple of years), the currently developed operating scenarios in TCV show discrete eigenmodes only up to $\sim 400 \text{ kHz}$. At the same time, it is well-known that high-frequency magnetic fluctuations in the multi-hundred kHz range are now (and have been for a while, see, for instance, Ref. 20) a routine measurement in many devices, so it is legitimate to ask what is the novelty and added value of this contribution, in addition to showing that a diagnostic system has already been put in place for future measurements.

First, looking at the literature on the experimental aspects of detecting high frequency magnetic fluctuations, it is immediate to remark that these measurements are most often provided in arbitrary/relative or digitizer ($=V$) units, with only some tentative attempts at providing values in physical units ($=T$) based on just scaling the measured voltage with respect to the frequency of the mode and the effective area of the sensors. Consequently, no quantitative estimate of the measurement uncertainties is ever provided and no attempt is seriously made at determining the contribution of diagnostic noise to the signal at that frequency. By obtaining and applying the full end-to-end calibration with the ensuing errors, and by measuring and explicitly accounting for the frequency-dependent EM noise pick-up, we are able to overcome this first set of drawbacks, namely, providing fully calibrated, absolute measurements in physical units with quantitative error estimates that include the contribution of frequency-dependent EM noise pick-up. Given that codes that use such magnetic fluctuations as input for the calculations do so most often with quantities in arbitrary/relative units, and then have to re-normalize various results based on additional data, it is clear that providing absolute measurements in physical units with quantitative errors can only help in improving the accuracy and reliability of the deliverables of these codes.

Second, and somewhat related, it is most often claimed that a magnetic measurement system has MHz capabilities because its acquisition frequency is 2 MHz or above, i.e., a *nominal bandwidth* as defined by the acquisition Nyquist frequency, while practically not considering at all the analog end-to-end transfer function. However, and beyond its basic electrical engineering definition, we consider that the *actual bandwidth* of a high-frequency magnetic diagnostic system should be defined by the frequency range where (a) the signal amplitude can be obtained in absolute units (i.e., not in digitizer voltage or arbitrary units) with a much smaller error-bar, (b) different magnetic sensors produce signal amplitudes that are equivalent and can be correlated in a straightforward manner, (c) the CMRR remains sufficiently high at those higher frequencies,

and (d) all the sources of diagnostic noise are quantitatively known so that the measured signal amplitude is a correct representation of the magnetic perturbation in the plasma, not the superposition of different and un-identified sources of signals. Therefore, it is argued that due to the lack of some of, if not all, these elements, only *qualitative* measurements of magnetic fluctuations have so far been obtained, even if these have been proven to be very useful for great advancements in theoretical and operational understanding of fusion plasma physics. We believe that diagnosticians working on high-frequency magnetic fluctuations should now strive to provide quantitative and thus much more constraining measurements up to the desired actual bandwidth, and in this contribution, we highlight and demonstrate all the steps that in our view are needed toward this goal. To our knowledge, some of these steps, for instance, the end-to-end system modeling tools, have never been used or presented before this work.

Third, a hot topic in the theoretical and modeling literature has now been for a while the interaction between energetic ions and background high-frequency broadband turbulent fluctuations,^{21–30} both ES and EM, which actually started with the actual measurements on the JET tokamak.^{31,32} This interaction has been shown to significantly affect fast ion confinement and overall turbulent transport mechanisms in certain operating regimes, with important consequences already measured for JET DT plasmas^{31,32} and foreseen for ITER and DEMO.^{21–23,28} Again looking at the literature, it is clear that only qualitative models for the background turbulent fluctuations are taken for and produced by the simulations. Therefore, and in order to progress with quantitative analyses and calculations, it is important to provide absolute measurements also for the relevant quantities describing these broadband EM turbulent fields, something that was not at all considered in previous work on high-frequency magnetic fluctuations.

The most important aspects of the work intended at optimizing the measurement performance of a high-frequency magnetic diagnostic system lie in having (a) an end-to-end acquisition line (namely, the sensor itself, the signal transmission line, and all data processing and acquisition cards) with the highest possible system resonant frequency and (b) an analog response that is as simple as possible in {amplitude, phase} vs frequency. While (a) guarantees that any attenuation of the signal above the system resonant frequency only moderately affects the higher frequency components, (b) allows us to significantly simplify the end-to-end system characterization and thus reducing the uncertainties associated with the modeling of the analog transfer function into the digital signal domain. Then, specifically for our LTCC-3D sensors, it is essential (c) to make sure that the single-axis equivalent measurements are efficiently and correctly decoupled from each other. This work is therefore to be intended essentially as a practical tutorial for our younger colleagues on how to build such a diagnostic system, capable of providing quantitative measurements of magnetic fluctuations, in general, in absolute units and with error bars, up to the ~1 MHz range. While it is obvious that some elements are really and only TCV-specific (such as where to place the front-end electronics), most are not (such as the end-to-end frequency calibration and the end-to-end system modeling tools), and it is expected that the latter will provide the intended guidance. To achieve this goal, a lot of materials need to be shown, which some could

(quite understandably) call a *tedious description of logbook-style*. Therefore, the majority of these elements are provided in the [supplementary material](#).

This paper is organized as follows: In Sec. II, we briefly present the main elements of the design, manufacturing, and installation work for these LTCC-3D sensors. Section III then focuses on the data acquisition system, which was optimized for high-frequency (i.e., not for equilibrium reconstruction) measurements above ~20 kHz. Section IV shows the measurement of the electrical properties and effective area of the as built LTCC-3D sensors, leading to Sec. V, which describes the main steps for the end-to-end system commissioning. Section VI focuses on the main steps in the data processing. Section VII then focuses on the overall system measurement performance, whenever possible drawing comparisons with the results obtained with the Mirnov sensors also used on TCV. Finally, Sec. VIII presents some initial results obtained with these LTCC-3D sensors, and Sec. IX provides a summary and conclusions, focusing on the main lessons learnt from these activities. Note that Secs. II and IV largely use excerpts of the material previously presented in Refs. 6, 15, and 16 in order to simplify the writing of this contribution.

II. SENSOR DESIGN, MANUFACTURING, AND INSTALLATION

Following the previously presented description of the design and manufacturing work for LTCC-1D⁶ and LTCC-3D^{15,16} sensors, these activities have been performed around four main stages. First, we have designed and produced in-house a number of LTCC-1D (for all three components: { δB_{TOR} , δB_{VER} , δB_{RAD} }), LTCC-2D (combining LTCC-1D sensors for either the δB_{TOR} or the δB_{VER} measurements, mounted on the alumina substrate used for the δB_{RAD} measurement, and then LTCC-1D sensors for the δB_{TOR} and δB_{VER} measurements mounted on a alumina substrate without windings), and finally complete LTCC-3D sensors with systematic variations in various design features around a baseline design to assess the effect of these design options on the frequency response of the 3D sensor. Second, we have measured the effective area NA_{EFF} and the impedance Z_{MEAS} of these sensors to extract their electrical properties, specifically the self-inductance L_{SELF} . Third, these electrical data were analyzed using a previously developed method⁶ to develop the equivalent circuit model for the sensor. Additionally, for the multi-D sensors, the mutual inductance L_{MUT} and parasitic area NA_{PAR} between the different measurement axes were also determined, and the algorithm leading to the equivalent circuit model was adapted to account for the mutual coupling between the different measurement axes. Fourth, the success of this measurement vs simulation exercise has allowed us to produce scaling laws for the main electrical properties of the LTCC-3D sensors so that the final sensor can be designed and built with much greater confidence in its predicted frequency response.

The main manufacturing steps for ceramic encapsulated sensors, such as those built using the LTCC technology, are described in detail in Refs. 6, 15, and 16 and are only briefly summarized here. Additional details, general and specific to the LTCC-3D sensors used in this work, are provided in the [supplementary material](#) (Sec. A).

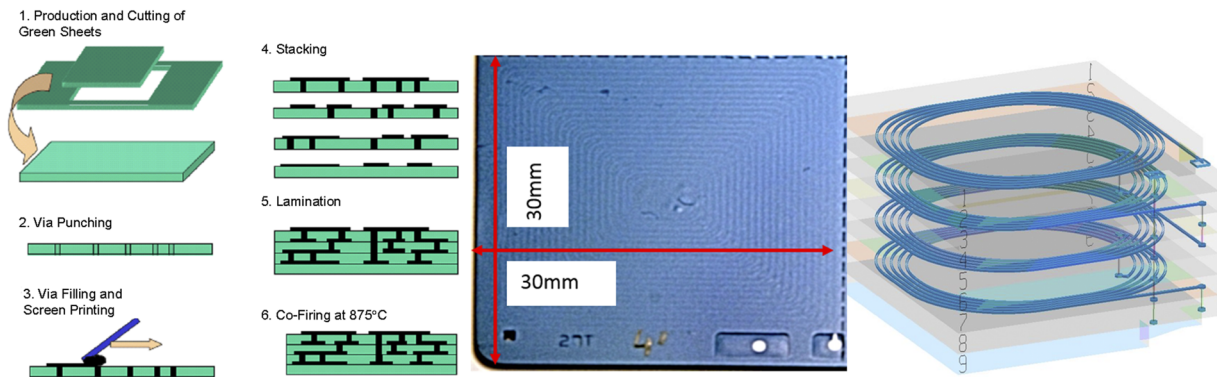


FIG. 2. (Left) The main steps for the manufacturing of the LTCC ceramic substrates. (Middle) An x-ray view of one LTCC-1D sensor, with contrast enhanced to show the turns in the top layer. (Right) A 3D model view of a LTCC-1D sensor, showing the windings spiraling across the layers and the inter-layer connection through the vias. [Figure partially reproduced with permission from D. Testa *et al.*, "Prototyping a high frequency inductive magnetic sensor using the non-conventional, low temperature co-fired ceramics technology for use in ITER," *Fusion Sci. Technol.* **59**(2), 376–396 (2011). Copyright 2011 Taylor & Francis Ltd.].

A ceramic encapsulated sensor is built up from thin ceramic tapes (*layers* in what follows), with an unfired thickness in the range of $\sim(100\text{--}400)\text{ }\mu\text{m}$, onto which a metallic ink is screen printed to form windings (*turns*) and ensure interlayer electrical connection through *via* holes. Figure 2 shows the main manufacturing steps for LTCC sensors, starting with the unfired ceramic base, the *green* sheets.

The three-axis (XYZ) LTCC-3D magnetic sensor is composed of three different parts: (1) a single-layer alumina substrate used as the sensor base and comprising the Z-axis coil, which provides the δB_{RAD} measurement, and all the on-board wiring used to connect the LTCC-1D modules and to bring the 3D measurements out to the electrical connection pads; (2) two groups of $10\times$ identical multi-layer LTCC-1D modules for the {X, Y}-axes, attached to the alumina substrate and connected using a balanced/four-quadrant series to provide the δB_{TOR} and δB_{VER} measurements, respectively; and (3) $6\times$ elongated rectangular alumina bars, used for the connection to the ex-sensor cables. Finally, the sensor is entirely covered with an insulating ceramic (alumina) casing to provide mechanical protection for the LTCC-1D modules and increase the overall robustness.

For the 3D sensor, it is very important to minimize the *mutual*, i.e., due to L_{MUT} , and *parasitic*, i.e., due to N_{PAR} , coupling between the different measurement axes. The mutual coupling effectively adds mostly to the sensor's self-inductance, namely, $L_{\text{SELF}} \rightarrow L_{\text{SELF}} + L_{\text{MUT}}$, therefore reducing the actual measurement bandwidth. The parasitic coupling mostly pollutes the measurements, namely, for the 3-axes {i, j, k} $\delta B_i \rightarrow \delta B_i + \alpha_{ij}\delta B_j + \beta_{ik}\delta B_k$. The L_{MUT} minimization is obtained by optimizing the on-board screen-printed wiring used to connect in series the different LTCC-1D modules and to bring the 3D measurements out to the electrical connection pads, which also contributes to reducing N_{PAR} . The main N_{PAR} minimization is actually obtained by pre-applying the required low-temperature brazing separately onto the alumina substrate and the LTCC-1D modules and then mounting the LTCC-1D modules onto the alumina substrate using a special comb to ensure that each LTCC-1D module sits perpendicularly onto the alumina base.

As one of the main scientific objectives of this project is that of extending the frequency range for the measurements of magnetic instabilities, and since the signal is strongly attenuated after the main system resonance at $f_{\text{RES}} \sim 1/(L_{\text{SELF}}C_{\text{CABLE}})^{1/2}/(2\pi)$, particular attention was devoted to optimizing the in-vessel and ex-vessel cabling, namely, reducing as much as possible its overall length and choosing cables with the lower capacitance/meter. Essentially, the main improvement was obtained by moving the whole acquisition electronics (including the Ethernet connection to the Model Data System (MDS) data repository) from the signal processing room outside the tokamak hall (as for the Mirnov sensors) to inside and as close as possible to the tokamak. With this, the total length of the ex-vessel cabling for the LTCC-3D sensors is then $\sim 3.5\text{ m}$, with $C_{\text{CABLE}} \sim 280\text{ pF}$ (which includes the capacitance of the $\sim 1.5\text{ m}$ of in-vessel cabling), compared to $\sim 35\text{ m}$ for the Mirnov sensors, with $C_{\text{CABLE}} \sim 1.2\text{ nF}$. More details of this work are provided in the [supplementary material](#) (see Sec. B for the in-vessel cabling and Sec. C for the ex-vessel cabling).

For both the in-vessel and the ex-vessel cabling, a female pin has to be connected to the ex-vessel male end of a molybdenum pin at the feedthrough. The pre-existing and almost fully occupied feedthroughs were used for the LTCC-3D sensors, and this complex operation became even more problematic. Two δB_{TOR} measurements (in sectors 14B and 16A) turned out to be affected by poor screening to ground.

III. DATA ACQUISITION ELECTRONICS

The data acquisition (DAQ) electronics sits in a crate in the tokamak hall and is built on a single printed circuit board (PCB) card of in-house design, which allows multiple functionalities, such as screening to ground, over-voltage and over-current protection, and frequency filtering and amplification. The output of this module is then directly fed to a D-TACQ Solutions® acquisition card, the ACQ132CPCI digitizer board, which also sits in the same crate. The DAQ output is then fed to the MDS repository using a screened Ethernet connection, directly from this crate without additional

cabling. Note that this crate is locally grounded at the Torus potential, with all other additional connections (for instance the Ethernet) completely GND-screened through isolation transformers. Some additional details of the DAQ for the LTCC-3D measurements are provided in the [supplementary material](#) (Sec. D).

A first version of the DAQ was installed using a set gain = 20: this choice proved unwise as the raw data were almost always in saturation during the Neutral Beam Heating (NBH) phase of the discharge, partly due to a large pick-up of the low-frequency signal from power supplies in the two δB_{TOR} measurements for which the screening to ground was poor. The DAQ was then modified adding an input protection filter and reducing the overall acquisition gain from =20 to =4. This second version of the DAQ is currently working without problems.

IV. SENSOR ELECTRICAL CHARACTERIZATION

The electrical characteristics of the HF LTCC-3D sensor can be extracted from the measurement of its impedance (the Z_{PROBE} data) and its voltage output (the V_{MEAS} data) when set in a Helmholtz coil configuration using the numerical techniques described in detail in Refs. 6, 18, and 33. Only the main steps of this method and the results of this analysis are briefly presented here to facilitate the reading of this contribution, while additional details are presented in the [supplementary material](#) (Sec. E).

The AC response curve of an HF magnetic sensor is, in general, non-trivial as the probe circuit is non-ideal. When working in Fourier space, the nominal response function of an HF magnetic sensor

$$V_{\text{PROBE}}(\omega) = N_{\text{EFF}}(\omega) \times i\omega \times B_{\text{MEAS}}(\omega) \quad (1)$$

is altered due to the probe's electrical characteristics. The simplest circuit model that can reasonably account for the probe's series inductance (L_{SELF}) and resistance (R_{SELF}), and its parallel capacitance (C_{SELF}) and admittance (P_{SELF}), is a one-pole circuit. In this case, the AC impedance is

$$\begin{aligned} Z_{\text{PROBE}}(s) &= \frac{R_{\text{SELF}} + sL_{\text{SELF}}}{1 + (R_{\text{SELF}} + sL_{\text{SELF}})(P_{\text{SELF}} + sC_{\text{SELF}})} \\ \Rightarrow Z_{\text{FIT}}(s) &= \frac{N_{\text{FIT}}(s)}{D_{\text{FIT}}(s)}, \end{aligned} \quad (2)$$

where $N_{\text{FIT}}(s)$ and $D_{\text{FIT}}(s)$ are polynomials in Laplace space $s = i\omega$ representing the numerator and denominator of $Z_{\text{PROBE}}(\omega)$ in its fitted representation $Z_{\text{FIT}}(s)$. Hence, the actual voltage measured by the sensor involves the probe's transfer function $H_{\text{PROBE}}(s)$,

$$\begin{aligned} V_{\text{MEAS}}(\omega) &= H_{\text{PROBE}}(\omega) V_{\text{PROBE}}(\omega) \\ &= [i\omega H_{\text{PROBE}}(\omega) N_{\text{EFF}}(\omega)] \times B_{\text{MEAS}}(\omega). \end{aligned} \quad (3)$$

The impedance measurements for each individual measurement axis of the LTCC-3D sensor were obtained using an impedance meter in the frequency range [10 Hz \rightarrow 13 MHz]. These measurements are compared with numerical fits obtained through Eq. (2) and the data obtained using the 1D and 3D versions of the LTCC electrical characterization algorithm presented in Ref. 6.

The measurements of the frequency-dependent effective $N_{\text{EFF}}(\omega)$ and parasitic $N_{\text{PAR}}(\omega)$ areas are obtained in a 3D

Helmholtz coil assembly system in the frequency range [10 Hz \rightarrow 50 kHz]. Due to the distributed nature of the LTCC-3D sensor, occupying a finite portion of the Helmholtz assembly, the direct output voltage measurement V_{OUT} from the sensor is modeled using the exact geometry of the Helmholtz assembly and of the sensor (both frequency-independent), taking into account the positioning of the different elements. Thus, a frequency dependent scaling factor can be obtained between the model and the actually measured V_{OUT} , leading to a scaling factor for converting the measured $N_{\text{EFF}}(\omega)$ and $N_{\text{PAR}}(\omega)$ into those for the equivalent non-distributed, *point-localized* sensor positioned at the geometrical center of the LTCC-3D assembly.

As $N_{\text{EFF}}(\omega)$ is only measured up to 50 kHz, with no phase information, while the LTCC-3D DAQ acquires at 2 MHz, the actual measurements are then fitted using a Padé approximation of a not-truly rational function $N_{\text{FIT}}(\omega)$ of order k ,

$$\begin{aligned} N_{\text{EFF}}(\omega) &\approx N_{\text{FIT}}(\omega) \\ &= N_{\text{EFF,DC}} \Pi_k \left| \left(1 + i\omega/\omega_{zk} \right)^{\beta_k} / \left(1 + i\omega/\omega_{pk} \right)^{\gamma_k} \right|, \end{aligned} \quad (4)$$

where $N_{\text{EFF,DC}}$ is a frequency-independent value determined as the measurements' mean value in the frequency range [100 Hz \rightarrow 10 kHz], $\{\beta_k, \gamma_k\}$ are positive rational (i.e., not necessarily integer as for a truly rational), and $\{\omega_{zk}, \omega_{pk}\}$ are the zeros and poles of k th order in $N_{\text{FIT}}(\omega)$, respectively. Typically, the poles are $\omega_{p1} \approx 2\pi \times \{25, 20, 15\}$ Hz and $\omega_{p2} \approx 2\pi \times \{125, 135, 85\}$ kHz, and the zero is $\omega_{z1} \approx 2\pi \times \{28, 26, 22\}$ Hz for the $\{X, Y, Z\}$ -axes. The fit error $|N_{\text{ERR}}(\omega)| = |N_{\text{EFF}}(\omega)| - |N_{\text{FIT}}(\omega)|$ determined in the entire frequency range [10 Hz \rightarrow 50 kHz] is extrapolated to 1 MHz and used in the ensuing data analysis. The rms value of $|N_{\text{ERR}}(\omega)|$ in the frequency range [10 Hz \rightarrow 50 kHz] is also used as a frequency-independent error estimate in the ensuing data analysis, specifically for the parasitic coupling calculations.

For $N_{\text{PAR}}(\omega)$, we use in the data analysis the frequency independent value $N_{\text{PAR,0}}$ determined as the mean value of the measurements in the frequency range [100 Hz \rightarrow 10 kHz]. The rms difference between $N_{\text{PAR}}(\omega)$ and $N_{\text{PAR,0}}$ over the entire frequency range of the measurements is then used as an error estimate on the parasitic coupling.

Table I summarizes the most important electrical data, namely, $\{R_{\text{SELF}}, L_{\text{SELF}}, L_{\text{MUT}}, N_{\text{EFF,DC}}, N_{\text{PAR}}\}$ for the fully assembled LTCC-3D sensors.

From the description of the sensor as given in Sec. II and from Fig. S1 of the [supplementary material](#), it is immediate to realize that the selected arrangement of the $\{X, Y\}$ measurement axes allows us to sum the effective areas of each LTCC-1D module. Conversely, the self-inductances of each LTCC-1D module do not sum up as $L_{\text{SELF}} \propto \text{ff} \times (N \times N_{\text{TURN}})^2 \times L_{\text{TURN}}$, where ff is the solenoid filling factor³⁴ and L_{TURN} is the inductance of each turn in the LTCC-1D module, i.e., the value for a single solenoid coil made with N fully joined LTCC-1D sub-assemblies with N_{TURN} each. For our distributed assembly, we have $L_{\text{SELF}} \propto \text{ff} \times N \times (N_{\text{TURN}})^2 \times L_{\text{TURN}} + L_{\text{MUT}}$, since there is an incomplete flux-linking between consecutive LTCC-1D modules *tuned* to the same resonant frequency. A significant design effort has yielded $L_{\text{MUT}} \ll \text{ff} \times L_{\text{TURN}} \times (N \times N_{\text{TURN}})$, and therefore, $\omega_{\text{RES}} \propto (L_{\text{SELF}})^{-1/2}$ is much higher than that for a single solenoid coil with the same N_{EFF} .

TABLE I. Measured electrical characteristics for the fully assembled LTCC-3D sensors, including the protection cover, and statistics over the 11 modules available for in-vessel installation. The value of the mutual inductance L_{MUT} is that between the different measurement axes: for the {X, Y}-axes, the contribution due to the coupling between the different LTCC-1D modules is already included in L_{SELF} , with this term accounting for $\sim 35 \mu\text{H}$ in the total value of $L_{\text{SELF}} \sim 160 \mu\text{H}$.

	$R_{\text{SELF}} (\Omega)$	$L_{\text{SELF}} (\mu\text{H})$	$L_{\text{MUT}} (\mu\text{H})$	$NA_{\text{EFF,DC}} (\text{cm}^2) (0.1 \text{ kHz} - 10 \text{ kHz})$	$NA_{\text{PAR}} (\text{cm}^2) (0.1 \text{ kHz} - 10 \text{ kHz})$
X-axis (δB_{VER})	126.75 ± 0.89	157.28 ± 4.03	[XY = 3.70, XZ = 0.33]	298.00 ± 4.32	3.44 ± 1.21
Y-axis (δB_{TOR})	127.16 ± 1.26	159.33 ± 3.34	[YX = 3.70, YZ = 0.35]	264.73 ± 5.31	3.41 ± 1.06
Z-axis (δB_{RAD})	18.23 ± 0.82	7.57 ± 0.10	[ZX = 0.33, ZY = 0.35]	216.18 ± 3.61	2.84 ± 1.14

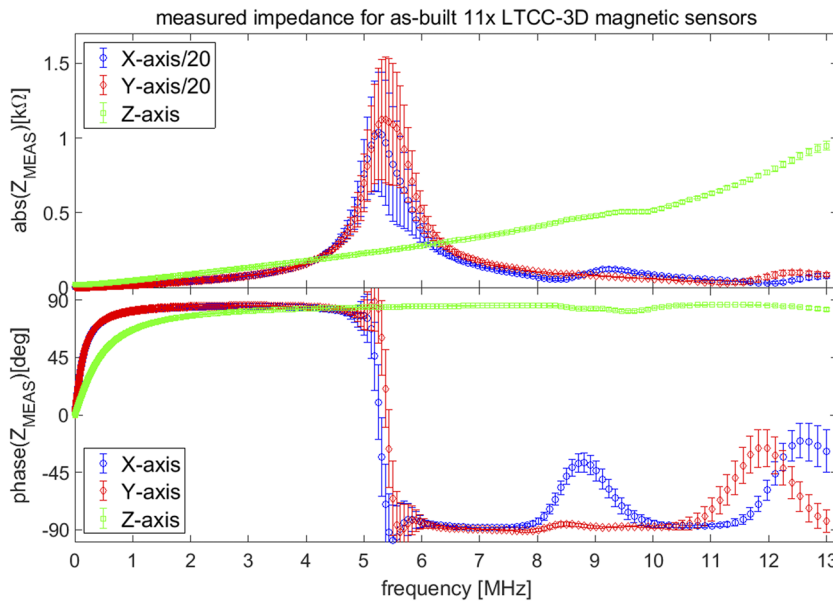


FIG. 3. The measured impedance data for all the as-built LTCC-3D sensors that include the output connection bars and the ceramic protection cover but not yet the ex-sensor/in-vessel cabling. The symbols indicate the average of the measurements over the 11 fully assembled 3D sensors, while the error bars indicate the scatter of the data.

This design conjecture is demonstrated by the Z_{PROBE} measurements for the final 3D sensor, which includes all the on-board wiring, the output connection bars, and the fully ceramic (thus insulating) protection cover (which sits all around the sensor), the data being shown in Fig. 3. The additional features in the measured Z_{PROBE} , particularly evident in the phase, are due to the mutual coupling between the different measurement axes. For the X-axis, these features occur in the frequency range $\sim [8 \rightarrow 10]$ MHz and >12 MHz. For the Y-axis, the most notable features are in the frequency range $\sim [11 \rightarrow 13]$ MHz. The effect of the mutual coupling is much less evident for the Z-axis and only appears as a small variation in the phase in the frequency range $\sim [9 \rightarrow 10]$ MHz. These features are then used to further constrain the estimate of L_{MUT} , which initially comes from the difference between L_{SELF} for each individual axis separately and that for the full 3D assembly.

We conclude that our most important design choice, i.e., producing the {X, Y}-axes using a balanced, four-quadrant, centered connection of well-separated $10 \times$ LTCC-1D modules, instead of one single solenoid-like coil, has delivered its goal, i.e., producing the same total effective area while reducing the total sensor's inductance [for more details, see the [supplementary material](#) (Secs. A and E)]. The overall very small parasitic effective area is due to a careful design of the wiring connections between the different LTCC

modules in the 3D sensor, allowing to center the output of all three measurement axes in the middle of the alumina board while reducing the on-board wiring loops required to bring the output of the three axes to the same cable connection area.

Comparing all the results for the electrical characteristics of the fully assembled LTCC-3D sensors, it is clear that some *ranking* can be established, namely, a preferred subset should be installed, while the others are kept as spares. The selection criteria are first the smallest L_{SELF} , then the largest NA_{EFF} , and then the smallest NA_{PAR} for all three measurement axes. With these criteria, sensor No. 3, No. 6, and No. 8 were finally selected for installation, and the ex-sensor/in-vessel cables with the smallest capacitance/meter were brazed onto these sensors.

V. END-TO-END SYSTEM COMMISSIONING

The end-to-end system commissioning takes place in different phases, essentially separating the passive in-vessel and ex-vessel components up to the input of the front-end electronics and then all the remaining active ex-vessel components up to the data as stored in the MDS repository. Different transfer functions are obtained for all these elements, which are then combined into the overall calibration steps for the LTCC-3D measurements.

For the first set of components, which include the sensor and in-vessel cabling, the feedthrough and the ex-vessel cabling up to the input of the front-end electronics, called the *sensor + cabling* section in this work, we write the bench measurements of $NA_{EFF}(\omega) = H_0(\omega)NA_{EFF,DC}$ and measure the line impedance to deduce the corresponding transfer function $H_1(\omega)$. For the second set of components, which includes all the elements of the DAQ and the Ethernet connection up to the data as stored in the MDS repository, we use a function generator to provide a voltage input for a frequency sweep in the relevant range. A reference signal, which does not pass through the DAQ but goes directly to the MDS repository, is collected together with the output voltages from the DAQ, the ratio of the two giving the second transfer function $H_2(\omega)$. Thus, Eq. (3) finally gives, in Fourier space,

$$\begin{aligned} V_{MEAS}(\omega) &= V_{PROBE}(\omega)H_1(\omega)H_2(\omega) \\ &= [i\omega \times NA_{EFF,DC} \times H_0(\omega)H_1(\omega)H_2(\omega)] \times \delta B_{MEAS}(\omega) \\ &= H_{E2E}(\omega) \times \delta B_{MEAS}(\omega). \end{aligned} \quad (5a)$$

Here, $H_{E2E}(\omega)$ is the end-to-end, frequency-dependent system's sensitivity, providing the calibration factor in physical units [V/T] between the input magnetic field $\delta B_{MEAS}(\omega)$ and the output measured voltage $V_{MEAS}(\omega)$ at each frequency point in Fourier space. For an ideal system, all $\{H_0, H_1, H_2\}$ have absolute value = 1 and phase shift = 0 up to frequencies much larger than the DAQ Nyquist frequency $f_{NYQ} = f_{sDAQ}/2$ (i.e., not only up to f_{NYQ} : it will be apparent why this is the case when considering the digital calibration and the end-to-end system modeling tools). Any departures from the linear scaling $H_{E2E}(\omega) \propto \omega$ indicate the system's (in)ability to measure a certain portion of the frequency spectrum.

The numerical methods associated with the extraction of a rational function $H(s)$ in Laplace space from the actual measurements obtained in the time/frequency domain are described in full in

Refs. 6, 18, 33, and 35: only the final results of this work are reported in Subsections V A–V D. Section V E briefly presents the main steps and different methods that are available for the conversion of the (measured, modeled, best-fit) end-to-end transfer function $TF_{E2E}(\omega) = H_0(\omega) \times H_1(\omega) \times H_2(\omega) \rightarrow TF_{E2E}(z)$ between the continuous analog Laplace $s = i\omega$ and the discretized digital $z = e^{sT}$ domains (T being the sampling time), $TF_{E2E}(z)$ being that actually used for the end-to-end calibration of the measurements. This last step also allows simulating the end-to-end hardware system's response to a known input signal, which is most useful to further evaluate the system's measurement bandwidth. Finally, and following up from our brief discussion in Sec. I on the most important aspects of the work intended at optimizing the measurement performance of a high-frequency magnetic diagnostic system, Sec. V F presents a summary and conclusions of this work to specifically illustrate what we have achieved.

A. Transfer function for the probe effective area, Laplace s-domain

Our aim is to determine $H_0(\omega)$ and $NA_{EFF,DC}$ using the measurement of the probe's effective area $NA_{EFF}(\omega)$ performed in our Helmholtz coil system for the fully assembled LTCC-3D sensors. The measurements were obtained up to 50 kHz, and therefore, we need to extrapolate the data up to the DAQ acquisition frequency = 2 MHz using the best fit to the data, similarly to the approach shown in Eq. (4). For this step of the analysis, we only show the data for the three sensors that were actually installed in-vessel, namely, sensor No. 3, No. 6, and No. 8.

Figure 4 shows the measurement of the absolute value of $NA_{EFF}(\omega)$ and its two best fits $|NA_{FIT1,2}(\omega)|$ for the X-axis of sensor No. 3, corresponding to the δB_{POL} measurements, which was installed in TCV in sector 02B. The corresponding data for the

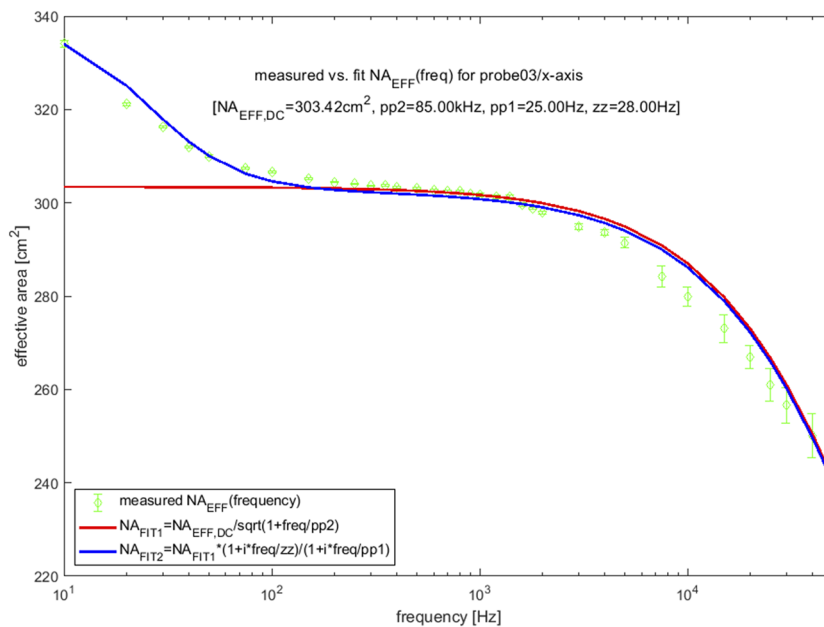


FIG. 4. The measurement $NA_{EFF}(\omega)$ and the best rational function fit $NA_{FIT}(\omega)$ for the effective area for the X-axis for sensor No. 3, which was installed in TCV in sector 02B. While $NA_{FIT1}(\omega)$ considers only the higher frequency dependent of $NA_{EFF}(\omega)$, i.e., the single pole ω_{p2} in Eq. (4), $NA_{FIT2}(\omega)$ also uses the first pair of pole and zero $\{\omega_{z1}, \omega_{p1}\}$.

Y-axis and the Z-axis are shown in the [supplementary material](#) (Sec. E3). The error bars on $|N_{\text{EFF}}(\omega)|$ come from the propagation of the expected measurement error on the current flowing in the Helmholtz coil assembly and the ensuing calculation of the magnetic field over the area of the sensor. The value of $N_{\text{EFF,DC}}$ used in the fits is taken as the average of the measurements in the frequency range [100 Hz \rightarrow 10 kHz]. Two fits are shown, but only the first, which keeps a constant $N_{\text{EFF}}(\omega)$ for frequencies below 50 Hz, is used for the end-to-end system's calibration. The second fit reproduces very well the apparent linear increase in $N_{\text{EFF}}(\omega)$ for frequencies below 50 Hz, which is due to the specific electrical features of our Helmholtz coil assembly and, therefore, is of no relevance for the end-to-end system's calibration.

In addition, for sensor No. 3, [Table II](#) shows the extrapolated values of $N_{\text{EFF}}(\omega = 0) = N_{\text{EFF,DC}}$ taken from $N_{\text{FIT1}}(\omega)$, the single zero and the two pole frequencies used to fit the data, and the frequency-independent value for N_{PAR} , taken as the average of the actual measurements in the frequency range [100 Hz \rightarrow 10 kHz]. Finally, the rms difference between $|N_{\text{EFF}}(\omega)|$ and $|N_{\text{FIT1}}(\omega)|$ in the frequency range of the measurements [10 Hz \rightarrow 50 kHz] estimates the magnitude error on $H_0(\omega)$. As there was no direct measurement of the phase of $N_{\text{EFF}}(\omega)$, the phase error on $H_0(\omega)$ is set to a nominal value $= 0.1 \times \pi/2$ [rad]. The data presented in [Fig. 4](#) and [Table II](#) for probe No. 3 are provided in the [supplementary material](#) (Sec. E) for the other two sensors installed in TCV.

B. Transfer function for the sensor + cabling section, Laplace s-domain

Our aim is to determine $H_1(\omega)$ using the measurement of the line impedance $Z_{\text{MEAS}}(\omega)$ from the input of the front-end electronics back to the in-vessel sensor. [Figure 5\(a\)](#) shows the summary measurements for the Z-data: the line impedance is measured from the input of the front-end electronics, which sits in the tokamak hall ~ 3.5 m away from the feedthrough, back toward the sensor in-vessel. Hence, the difference with respect to Z_{MEAS} for the sensor alone is due to the cabling and the feedthrough connection. The measurements for the δB_{VER} and δB_{TOR} components are all very similar, as expected, with notable differences only appearing at frequencies > 3 MHz. For these measurement axes, the resonant frequency sits

at around 600 kHz, well below the intended value $f_{\text{RES}} = 1$ MHz, and has a bandwidth $\gamma_{\text{RES}} \sim 300$ kHz. The resonant frequency is also below the value $f_{\text{RES}} = 0.67$ MHz predicted from the design. This is due to the fact that in our estimation we did not consider the contribution of the feedthrough (a pair of 10 cm-long molybdenum pins), adding some inductance and capacitance. The δB_{RAD} measurements have a resonance at a much higher frequency $f_{\text{RES}} \sim 2.7$ MHz and a similar bandwidth to that for the $\{\delta B_{\text{VER}}, \delta B_{\text{TOR}}\}$ measurements.

[Figure 5\(b\)](#) shows the H_1 -data for all nine δB components. The H_1 -data are obtained using a best fit to the Z-data, which uses one single pole and, therefore, does not account for the series resonances or the mutual coupling terms that are apparent in the measured Z-data much above the resonant frequency. In principle, we expect the δB_{VER} and δB_{TOR} measurements to have all a very similar transfer function, as they are obtained with a nominally equivalent arrangement on the 3D sensor: this is indeed observed up to frequencies ~ 3 MHz, notable differences only appearing at much higher frequencies. For the δB_{VER} and δB_{TOR} components, $H_1(\omega)$ only drops to $H_1(\omega) \sim 0.5$ at 1 MHz from the resonant value $H_1(\omega) \sim 4.2$ at ~ 600 kHz and then $H_1(\omega) = 1$ at ~ 830 kHz. Although our specification of an end-to-end $f_{\text{RES}} = 1$ MHz is clearly not met, the loss in sensitivity due to the sensor + cabling impedance is relatively minimal up to $f_{\text{NYQ}} = 1$ MHz, essentially because the resonance width is quite large ($\gamma_{\text{RES}} \sim 300$ kHz). For the δB_{RAD} components, we have that $H_1(\omega) \geq 1$ in the entire frequency range of the DAQ measurements, up to 1 MHz, with a resonant value $H_1(\omega) \sim 4.7$ at ~ 2.75 MHz.

Finally, the resonant value of $H_1 < 5$ at frequencies > 600 kHz and the very large bandwidth for all measurement axes were not expected to contribute to the saturation of the signal acquired by the DAQ, as, in this frequency range, the actual δB was expected to be very small from extrapolation of the Mirnov data. For this reason, we initially set up a rather large value $= 20$ of the DC gain for the DAQ, so as to increase the overall measurement sensitivity for the higher-frequency components > 600 kHz, which unfortunately proved unwise as the data were initially almost always in saturation.

Following the approach described in [Ref. 35](#), from the best fit $H_1(\omega)$, an equivalent circuit model can be reconstructed for which the impedance Z_{MODEL} can then be compared with the

TABLE II. The extrapolated values of $N_{\text{EFF}}(\omega = 0) = N_{\text{EFF,DC}}$ and its estimated error evaluated using the fit $N_{\text{FIT1}}(\omega)$ to the Helmholtz coil measurements $N_{\text{EFF}}(\omega)$, the rms error on $H_0(\omega)$, the zero and pole frequencies used to fit the measurements, and N_{PAR} , for the sensor No. 3, installed in TCV in sector 02B. For the rms error on $H_0(\omega)$, we take the value in the entire frequency range of the measurements [10 Hz \rightarrow 50 kHz], while for N_{PAR} , we take the average value in the frequency range [100 Hz \rightarrow 10 kHz]. The extrapolated values of $N_{\text{EFF,DC}}$ and the zero and pole frequencies are very close to the measured values obtained in the frequency range [100 Hz \rightarrow 10 kHz] for the individual axes.

Sensor-03	X-axis (δB_{VER})	Y-axis (δB_{TOR})	Z-axis (δB_{RAD})
$N_{\text{EFF,DC}}$ (cm ²)	303.42 ± 4.99	270.01 ± 3.07	223.11 ± 2.29
rms [error(H_0)]	3.15×10^{-2}	2.31×10^{-2}	2.28×10^{-2}
freqZero (1,1) (Hz)	28.00	25.00	20.00
freqPole (1,1) (Hz)	25.00	20.00	15.00
freqPole (1,2) (Hz)	135×10^3	125×10^3	85×10^3
N_{PAR} (cm ²)	[XY = 2.79, XZ = 1.47]	[YX = 3.15, YZ = 2.23]	[ZX = 2.13, ZY = 3.12]

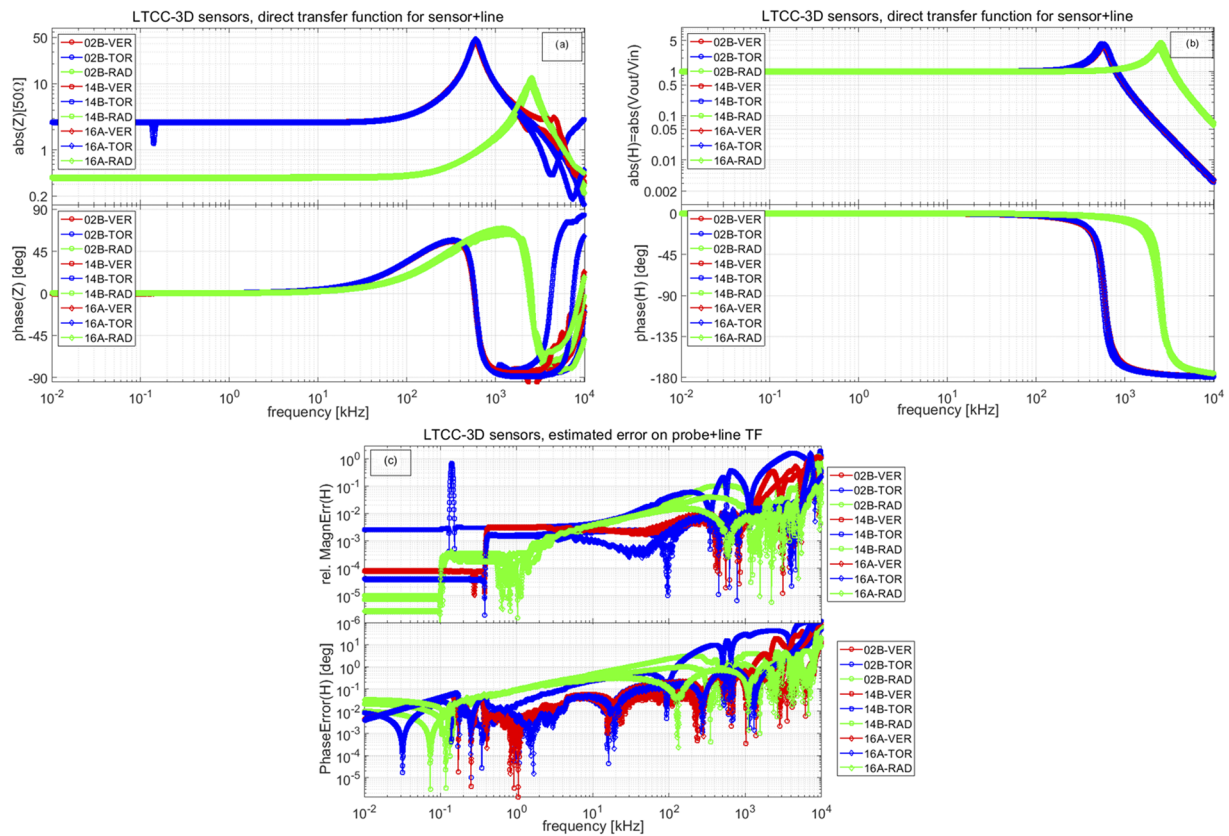


FIG. 5. (a) The measured impedance data for the three LTCC-3D sensors installed in-vessel: the sensors {No. 3, No. 6, and No. 8} are installed in the sectors {02B, 14B, 16A}, and the {X, Y, Z}-axes provide the $\{\delta B_{VER}, \delta B_{TOR}, \delta B_{RAD}\}$ measurements, respectively. The intrinsic $\sim 1\%$ variability in Z_{MEAS} is not shown, as it is comparable to the size of the symbols. (b) The transfer function $H_1(\omega)$ for the sensor + cabling section up to the input of the front-end electronics, extracted from the impedance measurements shown in (a). (c) The estimated error on the transfer function $H_1(\omega)$ for the sensor + cabling section up to the input of the front-end electronics, extracted from the best fitting to the impedance measurements shown in (a). The error on the magnitude is relative, while the error on the phase is absolute.

measurement Z_{MEAS} and its best fit Z_{PROBE} . The difference between Z_{MODEL} and $\{Z_{MEAS}, Z_{PROBE}\}$ then provides an error estimate for $H_1(\omega)$ as a complex function (amplitude and phase), which can be frequency-dependent (more cumbersome to use, but, in principle, more accurate) or tabulated so as to be able to take an rms value over a relevant frequency range. Figure 5(c) shows the estimated relative error on the amplitude and absolute error on the phase of $H_1(\omega)$. We clearly note that the two toroidal sensors (δB_{TOR} in sectors 14B and 16A) for which we had cabling issues during the installation show a much larger calibration error than the others. Otherwise, for frequencies below f_{NYQ} , the calibration error is rather small, below $\sim 20\%$ on the magnitude and below $\sim 10^\circ$ on the phase. Note that the sharply increasing error at frequencies above the resonance is essentially due to having used a best fit with one single pole for the impedance data, which does not account for the series resonances or the mutual coupling terms. This fit is, however, more robust for frequencies up to f_{NYQ} and, therefore, is preferred for data processing, despite the slightly larger ensuing error at frequencies above $f_{sDAQ}/2$.

C. Transfer function for the data acquisition electronics, Laplace s-domain

Our aim is to determine $H_2(\omega)$ using a voltage source as the input for the DAQ, collecting the reference signal over the *same* electrical path length: the phase distortion, not only the amplitude variation, can then be directly estimated from the ratio between the DAQ output and the reference. As indicated in Sec. III, two different DAQs were used: Fig. 6(a) shows the measured and modeled transfer functions for the current setup, and Fig. 6(b) shows the estimated amplitude and phase error on $H_2(\omega)$; the corresponding data for the initial DAQ are provided in the [supplementary material](#) (Sec. D).

In the current setup, the end-to-end DAQ TF is well modeled with a simple low-pass filter with a cut-off frequency at ~ 780 kHz and a DC gain of ~ 0.93 . As the measurements for all nine channels are very similar, with differences essentially comparable to the bit-noise error (the output signal obtained with input = 0 V), finally, we only use one single $H_2(\omega)$ for all the DAQ channels. The phase

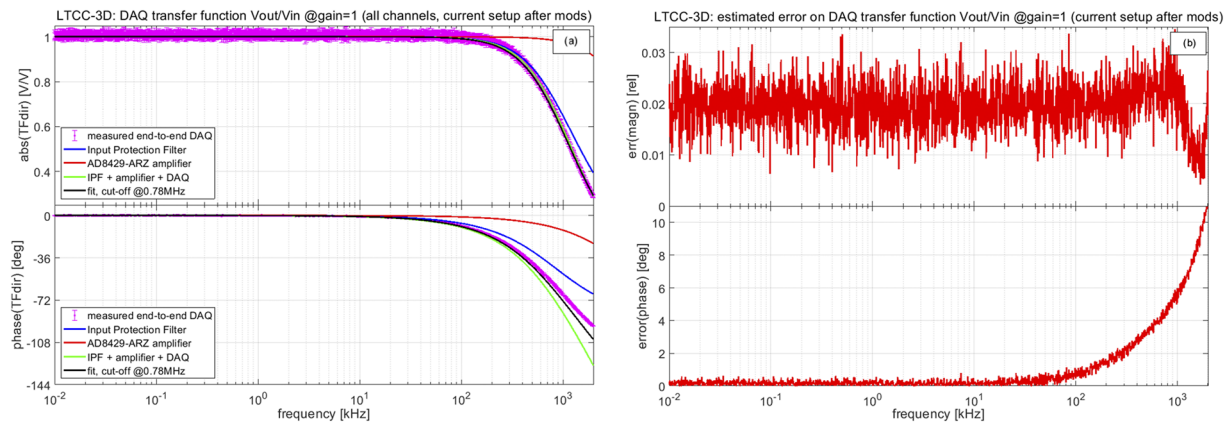


FIG. 6. (a) The transfer function $H_2(\omega)$ for the current DAQ, after modifications to the input protection. The data were collected using the nominal gain = 1 in the AD8429-ARZ ADCs. The measurements are very similar for all nine channels and are therefore plotted as their average value: the error bar indicates the standard deviation over all datasets. (b) The estimated complex error on $H_2(\omega)$ for the current DAQ, after modifications to the input protection. The error is relative for the amplitude and absolute for the phase.

shift is not well modeled with this simple low-pass filter, but as the rms difference between the measurement and this single-channel model is essentially the same for all nine acquisition channels of the DAQ, we accept this as a systematic error in the ensuing data processing.

The difference between the measurement and fitted $H_2(\omega)$ up to the DAQ acquisition frequency = 2 MHz provides an estimate of the error on this TF as a complex function (amplitude and phase). Similarly to the error on $H_1(\omega)$, this can be frequency-dependent (more cumbersome to use, but, in principle, more accurate) or taken as an rms value over a relevant frequency range. This error is rather small, of the order of $\sim 2\%$ for the amplitude (relative) and $< 10^\circ$ for the phase.

D. End-to-end transfer function in Laplace space, comparison with Mirnov probes

Having determined the individual elements of the TF(s) for all nine LTCC-3D measurements, we can now construct the end-to-end TF(s) combining them. An insightful representation is obtained when combining all terms appearing in the square bracket in Eq. (4), namely, constructing the end-to-end system's sensitivity $H_{E2E}(\omega) = \omega N_{A_{EFF,DC}} \times H_0(\omega)H_1(\omega)H_2(\omega)$ for the nominal DC gain = 1. Since $H_{E2E}(\omega) \times \delta B(\omega) = V_{MEAS}(\omega)$, $H_{E2E}(\omega)$ indicates the hardware's (in-)ability to measure the frequency spectrum of the perturbations to the different magnetic field components. The overall error on $H_{E2E}(\omega)$ is obtained via Gaussian propagation of the complex errors (amplitude and phase) estimated on each of its element as a frequency-dependent function and as an rms value in a relevant frequency range.

Figure 7 compares H_{E2E} for the nine LTCC measurements and one representative Mirnov sensor in both cases for the nominal DC gain = 1 in the DAQ (note that the Mirnov sensors are acquired with a typical DC gain = 32, while for LTCC-3D, this DC gain was ~ 20 and now is ~ 4). In TCV, the essential difference in $H_{E2E}(\omega)$ between the LTCC-3D and the Mirnov measurements comes from the

different setup of the DAQ, which, for the latter, is mostly common with that used for the equilibrium analysis¹⁸ and, therefore, is optimized for a 5 kHz bandwidth (the equilibrium DAQ sampling is at 10 kHz), and, thus, has a first set of pole/zero at $f_p \sim 90$ Hz and $f_z \sim 3.5$ kHz. We immediately note that in both cases, the linear scaling vs ω is clearly the dominant factor, as it is to be expected for an inductive sensor, with a (only partial for the LTCC-3D sensors) rollover in $H_{E2E}(\omega)$ at ~ 150 kHz due to $H_0(\omega)$, mostly evident for the Mirnov sensor [since $H_0(\omega) \propto 1/\omega$] and only partially for the LTCC-3D sensors [since $H_0(\omega) \propto 1/\sqrt{\omega}$]. Also note that the much higher sensitivity⁵⁵ for the LTCC-3D measurements (as an example a factor of ~ 100 at 100 kHz), particularly at high-frequencies, of which only a factor of ~ 3 (for δB_{VER} and δB_{TOR}) and a factor of ~ 2.5 (for δB_{RAD}), comes from the larger DC effective area.

For the LTCC-3D sensors, the data presented in Fig. 7 conclusively show that all our efforts in attempting to increase the measurement bandwidth toward 1 MHz have paid off, namely, we only have a relatively moderate drop in $H_{E2E}(\omega)$ with respect to the linear scaling $H_{E2E}(\omega) \propto \omega$ for higher frequencies > 200 kHz and up to the MHz range. Note that this positive feature of the measurement setup, together with a stronger crosstalking between channels and GND reference in the first version of the DAQ, and a much slower-than-expected (from extrapolation of the Mirnov data) power-law scaling for $\delta B(\omega) \propto \omega^{-\alpha}$ had one unintended and rather unfortunate consequence for the LTCC-3D measurements, namely, the almost routine saturation of the data before modifications to the input protection and the reduction in its DC gain from $20 \rightarrow 4$.

E. End-to-end transfer function in the digital z-domain

Having completed the measurement and modeling in Laplace space of the end-to-end TF(s) for the LTCC-3D data, we must now convert it to the digital z-domain, namely, obtaining the simulation of the complete measurement hardware, giving the system's

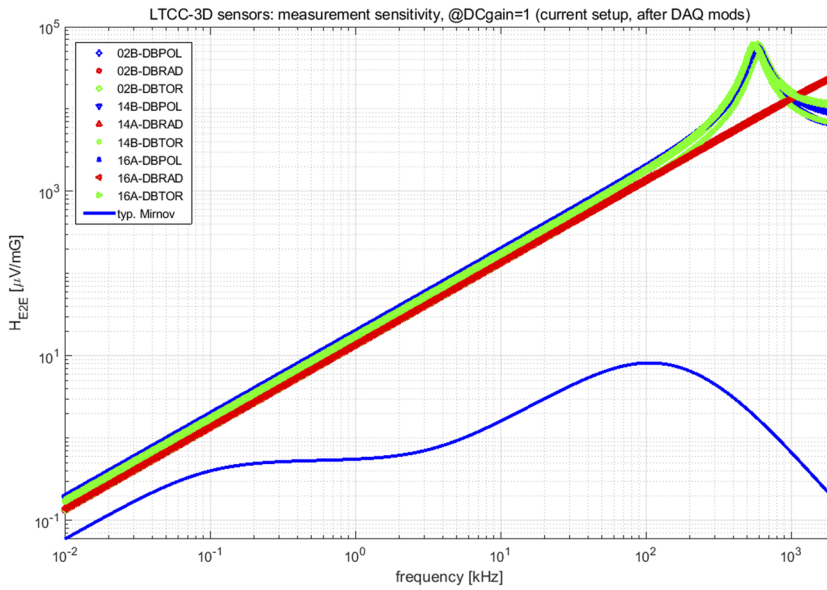


FIG. 7. The end-to-end measurement sensitivity $H_{EZE}(\omega) = H_0(\omega)H_1(\omega)H_2(\omega) \times \omega N_{\text{EFF}}(\text{DC})$ at the nominal DAQ DC gain = 1, such that $V_{\text{MEAS}}(\omega) = H_{EZE}(\omega) \times \delta B(\omega)$, and hence, the units are in ($\mu\text{V}/\text{mG}$). The data are shown for all nine LTCC-3D and one representative Mirnov measurements installed on TCV in the frequency range between 10 Hz and 2 MHz.

end-to-end response to an input signal. While mathematically the conversion from the s -domain to the z -domain is uniquely and exactly defined by $z = e^{sT}$, there are at least three different methods that perform numerically this conversion. Our preferred and routine choice (the reason to be presented below) is what we call the *LDS* method^{36,37} from the name of its original proponents. Two other methods (the bilinear discretization *BIL* and the impulse-invariant discretization *IID*) rely on using a first-order *bilinear* approximation to $z = e^{sT}$, hence $s = (1/T)\log(z)$ and its approximations,³⁸ namely,

$$z = \exp(sT) = \frac{\exp(sT/2)}{\exp(-sT/2)} \approx \frac{1 + sT/2}{1 - sT/2}, \quad (5b)$$

$$s = \frac{1}{T} \log(z) = \frac{2}{T} \sum_{j=0}^{\infty} \frac{1}{2j+1} \left(\frac{z-1}{z+1} \right)^{2j+1} \approx \frac{2}{T} \frac{z-1}{z+1}. \quad (5c)$$

Briefly reviewing the mathematical basis of the calibration in the z -domain, to determine the frequency response of a continuous-time filter, the analog transfer function $H_A(s)$ is evaluated on the imaginary axis $s = i\omega$, while the digital transfer function $H_D(z)$, with $z = \exp(sT)$, evaluates the frequency response of a discrete-time filter on the unit circle $|z| = 1$. The $s(=i\omega_A) \rightarrow z(=\exp(i\omega_D T))$ transform maps the entire $-\infty < \omega_A < +\infty$ axis of the analog s -domain repeatedly around the unit circle of the digital z -domain such that $-\pi/T < \omega_D < +\pi/T$.

When using the LDS method, the z -domain end-to-end filter coefficients are extracted from the (best-fit or simplest-fit to the) directly measured analog TF(s) in the Laplace s -domain, the caveat being that these coefficients become very sensitive to possible errors in the data used for extracting the analog transfer function. This problem can then be at least partially corrected using the Dennis-Schnabel variant of the original algorithm proposed by Levi, which weights the data in the s -domain with respect to their expected accuracy.

Conversely, the mapping provided by the bilinear transform $z = (1 + sT/2)/(1 - sT/2)$ is not equivalent to the $z = \exp(sT)$ mapping used by the LDS method, since, for the former, the correspondence between the *analog* $\omega_{k,A}$ and the *digital* $\omega_{k,D}$ frequency is given by $\omega_{k,D} = (2/T)\arctan(\omega_{k,A} T/2)$. Therefore, when using the bilinear approximation, all features in $H_A(s)$ will still exist in $H_D(z)$, but at a somewhat different frequency, the difference being larger as the characteristic features [namely, the zeros and the poles in the analog TF(s)] become comparable to $1/T$. To force an exact correspondence (gain, phase shift) but only at one selected frequency ω_0 , the bilinear transformation can be implemented with *pre-warping*, namely, setting $\omega_A = (2/T)\tan(\omega_D T/2)$, so that

$$s \approx \frac{2}{T} \frac{z-1}{z+1} \bigg|_{\omega_0} \rightarrow s \approx \frac{\omega_0}{\tan(\omega_0 T/2)} \frac{z-1}{z+1}. \quad (5d)$$

The BIL algorithm presents one significant advantage over the LDS method, namely, it requires only the pole(s) $s_{p,k}$ and zero(s) $s_{z,k}$ frequencies used to fit $H_A(s)$, but these have to be in equal number (which is not always necessarily the case, hence typically additional fudge zeros have to be added) and sufficiently far away from f_{NYQ} ; otherwise, in this case, $\{|s_{p,k} T|, |s_{z,k} T|\} \sim 1$. For these reasons, the BIL algorithm is only used for calibrating the LTCC-3D data for comparison purposes, as the historical calibration of the TCV Mirnov probes uses this method.

The IID algorithm starts from the bilinear transformation and then accounts for the system having a finite response and showing a lag time at $t = 0$ when transients/impulses are present in the input signal. Transients and/or impulses are short-duration wave packets for which a frequency decomposition cannot be uniquely defined or such that $H_A(s) < \epsilon$ for $|s| \geq \pi/T$.³⁹ Therefore, the IID algorithm is only suited for very short time windows when transient phenomena occur. This is the typical case of ELMs or mode locking over sub-ms timescales or mode frequency chirping on the fast ion timescales.

However, the IID algorithm cannot be easily connected to the calibration performed using the LDS and BIL methods as the impulse signal must start and finish at the value = 0; therefore, some form of background subtraction is needed; hence, it is only used on an *ad hoc* basis.

In the [supplementary material](#) (Sec. F), we show some further details of the comparison between the different methods for obtaining the end-to-end transfer function in the digital z-domain, using the simulated data produced following the same scheme illustrated in the [supplementary material](#) (Sec. I). Since the setup before the DAQ modifications was used for only a relatively short period of time, while the one after the DAQ modifications is that currently in use, from now on, we will only show data obtained with the latter, and some results obtained with the former are provided in the [supplementary material](#) (Sec. F) for completeness.

Figure 8 shows the simplest best fit (obtained using the data up to 10 MHz) to the analog end-to-end direct⁵⁶ $\text{TF}_{\text{dirE2E}}(s)$ and the estimated error on it for the different LTCC-3D measurements in the frequency range [10 Hz \rightarrow 2 MHz]. This fit is obtained using the lowest order for the {numerator, denominator} of the rational function that reproduces well the data, i.e., not convoluting the rational functions for each of the individual terms making up the end-to-end TF(s). The frequency-dependence of $\text{TF}_{\text{dirE2E}}(s)$ is effectively determined by the $\text{NA}_{\text{EFF}}(\omega)$ filtering, which corresponds to the first, i.e., at the lowest frequency, pole (cutoff) at a relatively high frequency ~ 150 kHz. For the $\{\delta\text{B}_{\text{POL}}, \delta\text{B}_{\text{TOR}}\}$ measurements, we also need to account for the resonance in $\text{H1}(\omega)$ at ~ 550 kHz attenuated by the DAQ pole at ~ 780 kHz, while this is not necessary for the $\delta\text{B}_{\text{RAD}}$ measurement ($f_{\text{RES}} \sim 2.75$ MHz).

Therefore, it is practical to use the same order [$n_A = 0$, $n_B = 1$] for the {numerator, denominator} of the rational function fit in the analog s-domain, which corresponds to a single pole/cutoff, and carry the discrepancies between the measurement and fit as a frequency-dependent error in the ensuing routine data analyses. This approach is preferred for the numerical stability of the filter

coefficients in the digital z-domain, when unsupervised data analyses are performed, and the somewhat higher error introduced in the Laplace s-domain is carried over in the calibration procedure. The alternative approach, which uses the convolution of the individual TFs for all the $\{\delta\text{B}_{\text{POL}}, \delta\text{B}_{\text{TOR}}, \delta\text{B}_{\text{RAD}}\}$ measurements, leads to a rational function fit for the direct $\text{TF}_{\text{E2E}}(s)$ of the much higher order [$n_A = 0$, $n_B = 6$], which is quickly becoming unstable above ~ 850 kHz, as shown in the [supplementary material](#) (Sec. F). This approach is then used only for supervised data analyses, when it is important to reduce the estimated errors above ~ 700 kHz for the $\{\delta\text{B}_{\text{POL}}, \delta\text{B}_{\text{TOR}}\}$ measurements.

The estimated relative amplitude error on $\text{TF}_{\text{dirE2E}}(s)$ is rather small and only starts to become significant (i.e., around ~ 0.1) close to the resonant frequency at ~ 550 kHz (for the $\delta\text{B}_{\text{POL}}$ and $\delta\text{B}_{\text{TOR}}$ measurements) and above $\sim 0.95 \times f_{\text{NYQ}}$ (for all measurements). The absolute phase error typically remains below 10° even very close to f_{NYQ} . The notable exception is the $\delta\text{B}_{\text{TOR}}$ measurement in sector 16A, which shows a large error at around 120 Hz and a divergence in the phase error above f_{NYQ} , both clearly linked to the partially faulty connection at the in-vessel side of the feedthrough.

Figure 9 shows the overall estimated error on the end-to-end digital inverse⁵⁷ $\text{TF}_{\text{invE2E}}(z)$ for the different LTCC-3D measurements: these frequency-dependent errors also include the contribution from the end-to-end hardware simulations, described in the [supplementary material](#) (Sec. F), averaged over different model input datasets. Two sets of results are shown, labeled *LDSfit* and *LDSconv*, respectively: the *LDSfit* method uses the *unsupervised* [$n_A = 0$, $n_B = 1$] model for $\text{TF}_{\text{dirE2E}}(s)$, while the *LDSconv* method uses the *supervised* [$n_A = 0$, $n_B = 6$] model. More details are provided in the [supplementary material](#) (Sec. F). The relative magnitude error on $\text{TF}_{\text{invE2E}}(z)$ is obviously larger than the corresponding value on $\text{TF}_{\text{dirE2E}}(s)$, but, overall, it remains below 0.45, with a broad maximum in the frequency range between 250 kHz and 400 kHz. Apart from being close to f_{NYQ} , the absolute phase error remains well below 20° . The error with the *LDSconv* method has narrower features and is smaller overall, particularly the

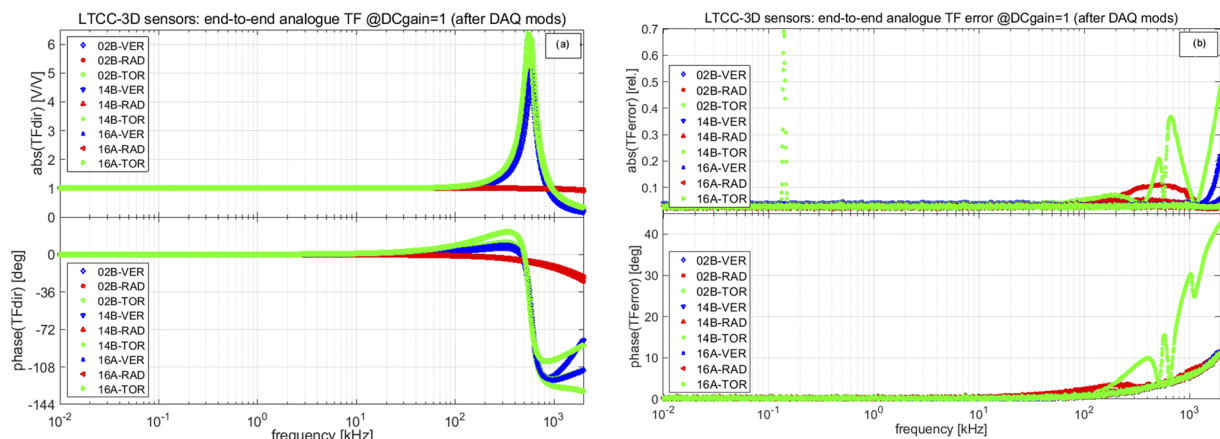


FIG. 8. The end-to-end analog direct $\text{TF}_{\text{dirE2E}}(s)$ (a) and its estimated error (b) for the different LTCC-3D measurements, after the DAQ modifications (the present setup).

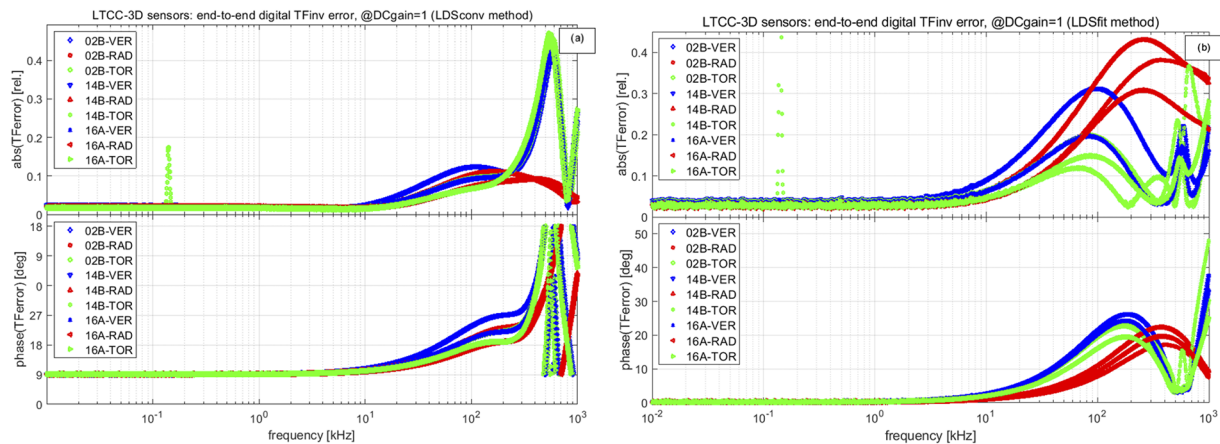


FIG. 9. The estimated error on the end-to-end digital inverse $\text{TFInv}_{\text{E2E}}(z)$ constructed using the *LDSconv* (a) and the *LDSfit* (b) methods for the different LTCC-3D measurements, in the frequency range between 10 Hz and 1 MHz, after the DAQ modifications (i.e., the current setup). As in the analog domain, the digital error for the signal 16A-TOR has a large spike at 120 Hz.

phase error. It is, however, larger around and beyond f_{RES} for the δB_{POL} and δB_{TOR} measurements, as it reproduces all the features in $\text{TFdir}_{\text{E2E}}(s)$ appearing at frequencies above f_{NYQ} by mapping them repeatedly over the unit circle $|z| = 1$. The error with the *LDSfit* method has broader features and is slightly higher, particularly the phase error.

We, therefore, conclude that, even using the lowest-order rational function fit for the analog TF, which captures only the essential features of the convolution of all the individual TFs, there is overall a good agreement between the simulated input and reconstructed output data, and this gives us the necessary confidence in using the digital filter coefficients obtained using this approach for the end-to-end calibration of the LTCC-3D measurements.

A precise evaluation of the results of the calibration procedure can be obtained by preparing an input frequency spectrum over a quasi-continuous time base (i.e., using a sampling time much higher than that actually used by the DAQ), simulating the continuous input spectrum of magnetic fluctuations picked-up by the magnetic sensors. This dataset is then fed into the analog simulation of the end-to-end hardware $[\text{TFdir}_{\text{E2E}}(s)]$ to obtain the *actual measurements*, which are then sampled at f_{sDAQ} . The resulting time series can finally be processed using $\text{TFInv}_{\text{E2E}}(z)$, and then, the frequency spectrum can be obtained, to be compared with the model input data. The estimated errors on the analog and digital end-to-end TFs are then used to provide a confidence interval for this simulation. In the [supplementary material](#) (Sec. F), an illustrative test result for the three δB components is shown.

The estimated error in $\text{TFInv}_{\text{E2E}}(z)$, which is built starting from the error on $\text{TFdir}_{\text{E2E}}(s)$, is then carried over as one of the elements of the overall error analysis. In the frequency domain, we use the actual frequency-dependent magnitude and phase errors, which include the contribution from the end-to-end hardware simulations. In the time domain, there is not an exact analytical formulation allowing the conversion of the frequency-dependent error on $\text{TFInv}_{\text{E2E}}(z)$; therefore, we have run a large number of simulations, similar to those shown in the [supplementary material](#) (Sec. F),

varying the input model dataset. We then use as an error estimate the overall rms value of the difference between the input and reconstructed time series, and the frequency-dependent relative difference in the Power Spectral Density (PSD).

F. End-to-end transfer function: Summary and conclusions, and the impact on the detection capabilities at high frequency

As stated in Sec. I, two of the most important aspects of the work intended at optimizing the measurement performance of a high-frequency magnetic diagnostic system lie in having (a) an end-to-end acquisition line with the highest possible system resonant frequency and (b) an analog response that is as simple as possible in {amplitude, phase} vs frequency.

Sections V A–V E show that the end-to-end system sensitivity $H_{\text{E2E}}(\omega)$ is very high for the LTCC-3D sensors and scales practically linearly with the frequency up to ~ 600 kHz for the δB_{POL} and δB_{TOR} measurements and then with a moderate resonance (gain ~ 4.5) and a small drop-off above this resonance (a factor of ~ 5 at 1 MHz). For the δB_{RAD} measurement, $H_{\text{E2E}}(\omega)$ scales practically linearly with the frequency up to at least 2 MHz. Therefore, the requirement (a) is clearly satisfied, and thus, we expect excellent detection capabilities up to the MHz range, namely, the signal acquired by the DAQ should remain well above the intrinsic noise level.

The analog response is relatively simple for the δB_{POL} and δB_{TOR} measurements: one resonance attenuated by the two poles/cutoffs in the effective area and the DAQ; it is even simpler for the δB_{RAD} measurements: only the pole/cutoff in the effective area practically matters. The modeling $\text{TFdir}_{\text{E2E}}(s) \rightarrow \text{TFInv}_{\text{E2E}}(z)$ is then relatively simple, and the ensuing calibration errors can be kept sufficiently small. Therefore, the requirement (b) is also satisfied, and thus, we expect a small error on the derived measurements of mode frequency, amplitude, and {toroidal, poloidal} mode numbers for discrete eigenmodes, and of spectral breaks (location and exponents) for the continuum spectrum.

The results of the very time-consuming and often very tedious hardware and software development work leading to satisfying (a) + (b) are best observed using a simulated time series: the input frequency spectrum is known, and thus, the accuracy of the output results is characterized best. This is precisely the purpose of the simulations shown in the [supplementary material](#) (Sec. I).

VI. BASIC DATA ANALYSIS PROCESSING

After pulling the raw data from the MDS repository, the data processing revolves around four main steps, each being briefly described in Subsections VI A–VI D. Subsection VI E then puts together all the elements of the error analysis for each individual step in the data processing.

A. Parasitic and mutual coupling contribution

As indicated above, the data obtained from the different measurement axes are not fully separated due to the parasitic areas and mutual inductances between the axes, so we must process the various contributions in such a way that each signal will be the single-axis-equivalent for the corresponding δB component. The equation to be solved involves the area (effective and parasitic) and the mutual inductance and takes the simplified matrix form

$$\begin{aligned} [V_{MEAS}] &= NA_{MUT} \times \frac{d}{dt} [\delta B_{MEAS}] - L_{MUT} \times \frac{d}{dt} [I_{MEAS}] \\ &= NA_{MUT} \times \frac{d}{dt} [\delta B_{MEAS}] - [Z_{MEAS}]^{-1} \times L_{MUT} \\ &\quad \times \frac{d}{dt} [V_{MEAS}], \end{aligned} \quad (6a)$$

where $\{[V_{MEAS}], [\delta B_{MEAS}], \text{ and } [I_{MEAS}]\}$ are the 3×1 column vector for the measured voltage, magnetic field, and current (i.e., the measured voltage divided by the impedance) in each sensor for each measurement axis, $[[NA_{MUT}]]$ is a 3×3 matrix with the effective (diagonal terms) and parasitic areas (off-diagonal terms) for each sensor, and $[[L_{MUT}]]$ is a 3×3 matrix with the mutual inductances between the different axes on the off-diagonal terms (the diagonal terms are exactly = 0). Note that the simplified form of Eq. (6a) does not include the capacitive coupling between adjacent wires, which is proportional to the time integral I_{MEAS} , and therefore, it is not valid in the presence of time-varying (quasi-)DC magnetic fields in vacuum, when capacitive coupling between the different measurement circuits becomes indeed the dominant contribution.⁵⁸

When including only the contribution of a frequency-independent parasitic area, Eq. (6a) can be solved exactly for $[X] = d([\delta B_{MEAS}]/dt)$ with $[Y_1] = [V_{MEAS,RAW}]$ and $[[A]] = [[NA_{MUT}]]$ as it takes the form $[Y_1] = [[A]] \times [X]$. Thus, the solution simply becomes $[Y_2] = \text{diag}([A]) \times [X]$, where $[Y_2] = [V_{MEAS,MCI}]$ corresponds to a single-axis-equivalent raw voltage measurement corrected for the parasitic area.

When also including the contribution of the mutual inductances, the problem becomes intrinsically more complicated since now we must find a method to deal with a time derivative and with the frequency-dependence of $Z_{MEAS}(\omega)$, which links $I_{MEAS}(\omega)$ to $V_{MEAS}(\omega)$. The actually exact and simpler approach would be to

work in Fourier space, thus obtaining

$$\begin{aligned} [V_{MEAS}(\omega)] &= (i\omega)[[NA_{MUT}(\omega)]] \times [\delta B_{MEAS}(\omega)] - [Z_{MEAS}(\omega)]^{-1} \\ &\quad \times (i\omega)L_{MUT} \times [V_{MEAS}(\omega)] \\ &\Rightarrow \{1 + (i\omega)L_{MUT} \times [Z_{MEAS}(\omega)]^{-1}\} \\ &\quad \times [V_{MEAS}(\omega)] \\ &= (i\omega)NA_{MUT}(\omega) \times [\delta B_{MEAS}(\omega)]. \end{aligned} \quad (6b)$$

Equation (6b) is exactly solvable for each frequency component in Fourier space, as it accounts exactly for the frequency-dependence of $Z_{MEAS}(\omega)$ and $NA_{MUT}(\omega)$, and can then be inverted to obtain the time sequence $\delta B_{MEAS}(t)$. However, Eq. (6b) cannot be practically used when willing to keep a high-temporal/high-frequency resolution as the Fourier decomposition requires time-binning weighted using an appropriate window; hence, the resulting value for $\delta B_{MEAS}(t)$ would be a weighted time average. As an example, using a Fourier decomposition over 16 time samples, the time average is over $16 \times 0.5 \mu s = 8 \mu s$, thus an effective DAQ sampling frequency = 125 kHz.

There are two methods that can be used to avoid the computation of the time derivative of the current flowing in each measurement circuit (I_{MEAS} is typically small, but its time derivative could have very large spikes unless heavily smoothed). Both methods need to use some approximation for the exact frequency dependence of $Z_{MEAS}(\omega)$ and $NA_{MUT}(\omega)$: the mathematical details are presented in the [supplementary material](#) (Sec. G). In summary, based on the analysis of multiple TCV discharges in different operating conditions, we approximate the time derivative $dV_{MEAS}/dt \sim V_{MEAS}/\tau$, where $\tau \sim [10 \rightarrow 100] \mu s$ represents the typical time scale for the temporal variation in V_{MEAS} associated with changes in the background plasma, and find two averages, therefore frequency-independent values for $\langle V_{MEAS}(\omega, t)/Z_{MEAS}(\omega) \rangle = \gamma(t)$ and $\langle NA_{MUT}(\omega) \times \delta B_{MEAS}(\omega, t) \rangle = \beta(t)$, and use them in Eq. (6a) to obtain

$$\begin{aligned} [V_{MEAS}(t)] &= NA_{MUT} \times \frac{d}{dt} [\delta B_{MEAS}] - [Z_{MEAS}]^{-1} \times L_{MUT} \\ &\quad \times \frac{d}{dt} [V_{MEAS}] \\ &= [[PMC(t)]]^{-1} \times \{[[NA_{MUT,DC}]] \times [[\beta(t)]]\} \\ &\quad \times \frac{d}{dt} [\delta B_{MEAS}(t)]. \end{aligned} \quad (6c)$$

In Eq. (6c), $[[NA_{MUT,DC}]]$ is the DC value of $[[NA_{MUT}]]$ and $[[PMC]]$ is a 3×3 matrix, in principle, time-dependent, with the frequency-integrated mutual coupling terms in the off-diagonal elements. The order of magnitude of this correction to the measurements is given by the sum over the two axes orthogonal to the one being processed of $\gamma L_{MUT}/\tau + NA_{PAR,DC}/NA_{EFF,DC} \sim [5 \rightarrow 15] \times 10^{-2}$; the relevant measurements and ensuing coefficients are shown in the [supplementary material](#) (Sec. G). This indicates that the parasitic + mutual coupling terms are at most contributing to $\sim 15\%$ of the raw signal for each measurement axis.

Note that the simplified approach used to account for the mutual coupling between the different measurement axes has been specifically optimized for the higher-frequency range in the $\delta B_{MEAS}(\omega, t)$ spectrum, as it does not consider capacitive coupling.

Therefore, we rely on a different and more efficient algorithm to remove the signal components that are due to the DC and lower-frequency components in the $\delta B_{\text{MEAS}}(\omega, t)$ spectrum, and this is presented in detail in Subsection VI C.

As an example of these mutual coupling calculations, we consider the measurements obtained for TCV discharge No. 53454, where Electron Cyclotron Heating (ECH) at the second harmonic (X2) was used together with Neutral Beam Heating (NBH) to produce a scenario where sawbones^{40,41} were observed during the NBH phase. As this discharge, and other very similar, will be used repeatedly in this work, Fig. 10 shows the main plasma parameters during the NBH phase.

The bursts appearing in the δB_{VER} data shown in Fig. 11 during the NBH phase are the sawbones, i.e., the variant of the well-known fishbones,⁴² which are produced when quasi-tangential (instead of quasi-normal) NBH is used. Then, it is experimentally observed that the sawbones invariably act as the sawtooth⁴³ precursor, while multiple fishbones can occur during a single sawtooth cycle. In TCV, which is indeed equipped with a quasi-tangential NBI system, sawbones are routinely observed during on-axis NBH experiments on all LTCC-3D δB components, and these bursts have a typical duration of 1 ms with a periodicity of 7 ms \rightarrow 10 ms corresponding to the sawtooth period.

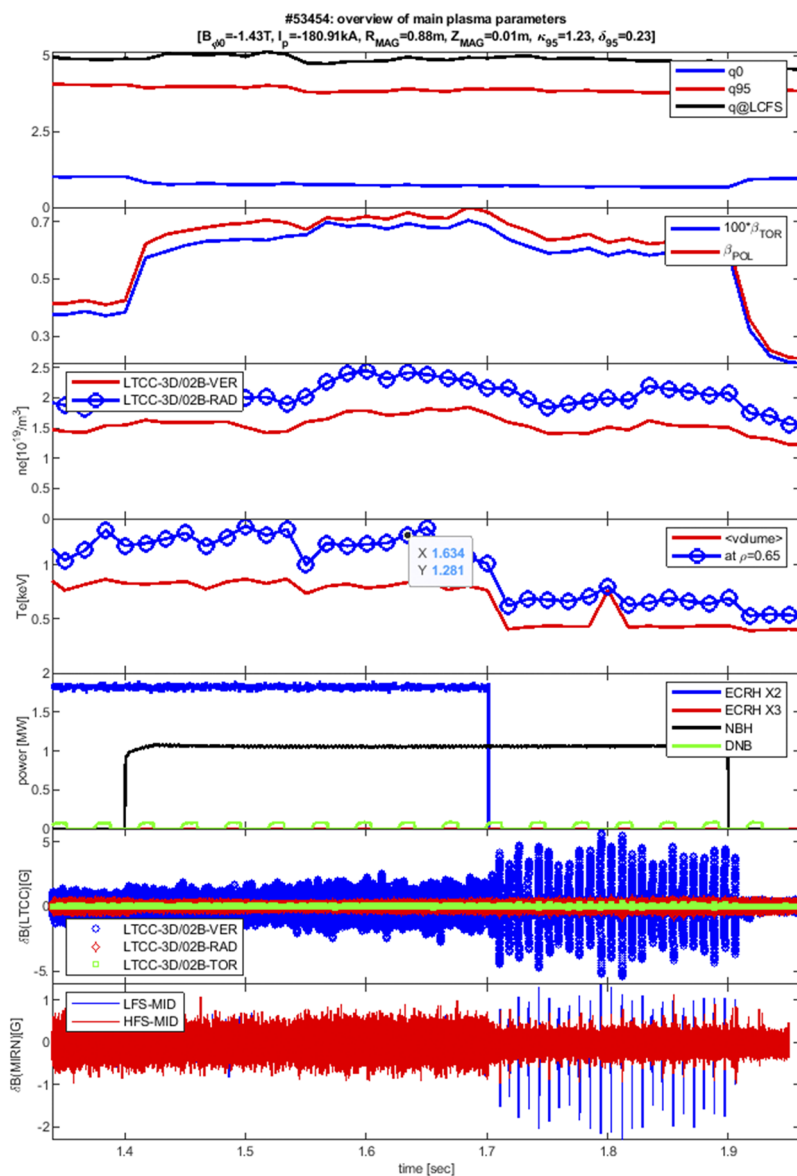


FIG. 10. The main plasma parameters for the TCV discharge No. 53454 during the NBH phase. The toroidal magnetic field and plasma current are $B_\phi = -1.43$ T and $I_p = -180$ kA, respectively; the plasma is centered at $Z_{\text{MAG}} \sim 1.2$ cm and has elongation $\kappa_{95} = 1.23$ and triangularity $\delta_{95} = 0.23$ at $\rho_{\text{POL}} = 0.95$, where ρ_{POL} is the TCV radial coordinate expressed in terms of the square root of the normalized poloidal flux. The bursts clearly apparent on the magnetic data (both for the Mirnov and LTCC-3D sensors are shown) are the sawbones, and the location of the $q = 1$ surface is $\rho_{\text{POL}} \sim 0.65$.

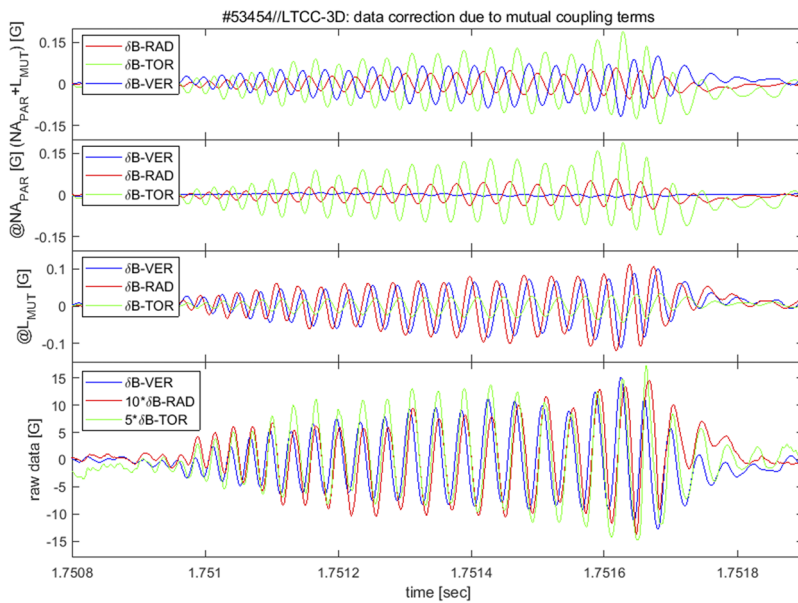


FIG. 11. Estimates of the correction to the raw $\delta B_{\text{MEAS}}(t)$ for one specific sawbone in the TCV discharge No. 53454. The raw/un-corrected data are shown in the bottom subplot; then, the corrections due to the mutual coupling and parasitic area separately are shown in the middle subplots; finally, the top subplot shows the total correction, i.e., adding these two terms, required to obtain the best estimate of the *true* $\delta B_{\text{MEAS}}(t)$. For clarity of presentation, the error bars on the data are not shown, as these are quite small, and hence would be completely masked by the datasets.

Figure 11 shows the LTCC-3D data for one individual sawbone in the TCV discharge No. 53454, with four different values for $\delta B_{\text{MEAS}}(t)$ obtained, respectively, first without both the parasitic and the mutual coupling (dubbed the *raw data*), then showing the correction obtained when including separately only the contribution of the mutual inductance, then only of the parasitic area, and finally the *true* value for $\delta B_{\text{MEAS}}(t)$, which is obtained when both terms are included in the calculation.

The removal of the parasitic and mutual coupling terms from the raw data only marginally change by at most 15%, the actual value of $\delta B_{\text{MEAS}}(t)$, confirming our estimates. This correction is relatively more important for the δB_{TOR} component due to the pick-up of the larger $\{\delta B_{\text{VER}}, \delta B_{\text{RAD}}\}$ components through the parasitic areas and similarly, but to a smaller extent, for the δB_{RAD} component through the parasitic pick-up of the δB_{VER} component. Note the small difference between these sets of data, particularly for the δB_{VER} component (which is typically much larger than the $\{\delta B_{\text{RAD}}$ and $\delta B_{\text{TOR}}\}$ components), since $NA_{\text{PAR}} \sim 3 \text{ cm}^2$ compared to $NA_{\text{EFF}} > 200 \text{ cm}^2$ and $\omega L_{\text{MUT}}/Z_{\text{MEAS}} > \sim [5 \rightarrow 20] \times 10^{-2}$.

We can now estimate the error introduced in the actual value of $\delta B_{\text{MEAS}}(t)$ when considering *only* the different approximations that we have used to obtain $[[NA_{\text{MUT}}]]$ and $[[PMC]]$, assuming that $V_{\text{MEAS}}(t)$ is exactly known as a starting point [this assumption will then be removed, and the estimated error on $V_{\text{MEAS}}(t)$ will be explicitly considered in Sec. VI E]. As the correction due to the $[[NA_{\text{PAR}}]]$ and $[[PMC]]$ is relatively small, as shown in Fig. 11, even a large estimated error only has a minimal impact on the overall error estimate for $\delta B_{\text{MEAS}}(t)$.

Conversely, the measurements and modeling leading to $\{\beta(t), \gamma(t), \tau\}$ are clearly non-trivial and would be very time-consuming had we to do it *on-the-fly* for each individual time window selected for the analysis. Hence, a one-off analysis of multiple TCV discharges was performed, giving nominal values for $\{\beta(t), \gamma(t), \tau\}$ as the rms value over this dataset, with the standard deviation then used

as an error estimate. Then, $\{\beta(t), \gamma(t), \tau\}$ all carry a relative error of ~ 0.5 , again conservatively estimated.

As stated in Sec. I, the third most important aspect of the work intended at optimizing the measurement performance of the LTCC-3D magnetic diagnostic system lies in (c) making sure that the single-axis equivalent measurements are efficiently and correctly decoupled from each other. The analysis presented here shows that the coupling between the different measurements is indeed non-negligible but neither dominant and can be determined efficiently (after extensive measurements and some intricate math), with ensuing additional errors in the total estimate of the true $\delta B_{\text{MEAS}}(t)$ that are sufficiently small. Therefore, the first criterion for satisfying the requirement (c) has been met.

B. Field-alignment of geometrical measurement axes

Having processed the raw data to subtract the mutual coupling between the measurement axes, we can now compare the results obtained when projecting the processed data from the geometrical, wall-aligned to the field-aligned components. As an illustration of this processing step, we consider again the TCV shot No. 53454 during the NBH time windows, when sawbones are present, and Fig. 12 shows the results of this analysis. For this discharge, the vertical position of the magnetic axis is $Z_{\text{MAG}} \sim 1.2 \text{ cm}$, the edge safety factor is $q_{95} \sim 3.5$, and the edge elongation and triangularity are $\kappa_{95} = 1.35$ and $\delta_{95} = 0.23$ at $\rho_{\text{POL}} = 0.95$, respectively. Therefore, for the radial and vertical components, we have a quasi-parallel alignment $\delta B_{\text{RAD}} \parallel \delta B_{\text{NOR}}$ and $\delta B_{\text{VER}} \parallel \delta B_{\text{POL}}$. As a further example, in the [supplementary material](#) (Sec. H), the comparison between the wall-aligned and field-aligned components for one on-axis, i.e., with $Z_{\text{MAG}} \sim 0 \text{ cm}$, vs one positive off-axis, i.e., with $Z_{\text{MAG}} \sim +26 \text{ cm}$, TCV discharges is shown to illustrate the importance of this correction to the measurements.

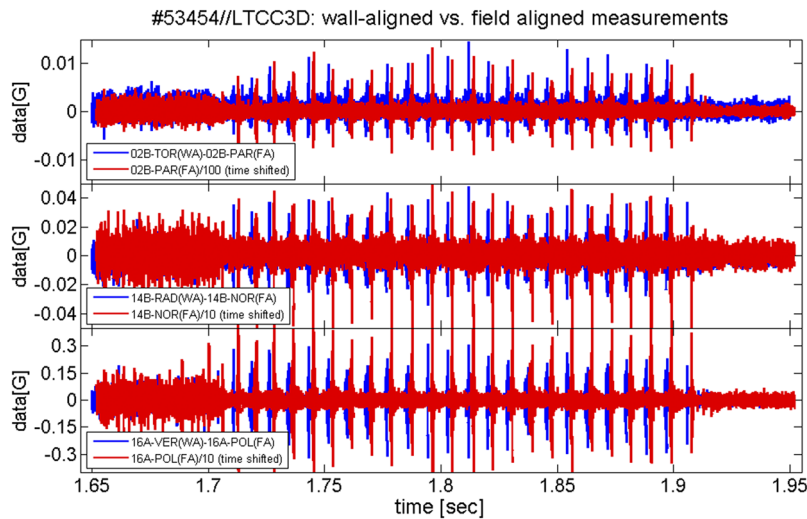


FIG. 12. Comparison between the wall-aligned and field aligned measurements for the TCV shot No. 53454 during the NBH time windows, when sawbones are present. The data are calibrated for the frequency-dependence, integrated, and high-pass filtered @300 Hz, and the mutual coupling between the different measurement axes was included in this analysis. Again, the error bars on the data are not shown, as these are comparable to, and hence would completely mask the small differences between the datasets. Also for clarity of presentation, the actual data have been time shifted by +2 ms and re-scaled by a factor of [10, 10, 100] for the $\{\delta B_{POL}, \delta B_{NOR}, \delta B_{PAR}\}$ components, respectively.

In TCV shot No. 53454, the difference between the wall-aligned and field aligned measurements is small for the $\{\delta B_{POL}, \delta B_{NOR}\}$ components, as typically it is not exceeding 15%, but not irrelevant, and therefore, this calculation should be explicitly performed if an accurate evaluation of the mode amplitude is to be undertaken. Conversely, this difference is negligible for the δB_{PAR} component, as typically it is $\sim 1\%$, completely within the measurement uncertainties.

The error on this correction to the measured $\delta B_{MEAS}(t)$ essentially depends on the accuracy of the actual installation with respect to the nominal position of the sensor given in the installation drawings (less than 1 mm) and the accuracy of the equilibrium reconstruction, specifically the position and orientation of the LCFS in front of the sensor and the value of q_{95} . This last term has been estimated by using different options for the TCV equilibrium reconstruction (the LIUQE code⁴⁴) and extracting the ensuing variance in the geometrical coefficients needed for this step of the analysis. The estimated error is very small, typically well below 10% of the difference between the wall-aligned and field-aligned components.

C. Removal of the signal components due to the equilibrium magnetic field and the in-vessel active stabilization coils

The setup of the LTCC-3D measurement system is sensitive to the pick-up of the equilibrium toroidal field since, for the typical TCV operational conditions, the nominal, unfiltered, signal component due to $B_\phi = 1.43$ T @120 Hz would be $V_{\phi, TOR} \sim 28.60$ V at the DAQ DC gain = 1 in the toroidal measurements, clearly saturating the DAQ. Some low-frequency filtering was already provided in the first version of the DAQ, and this was much improved in the second and currently operational setup, but the low-frequency signal components are still not completely removed. TCV is also equipped with a rather large number of ex-vessel coils (also operating at 120 Hz) for producing the equilibrium magnetic field (see Fig. 1 of Ref. 18 for the labeling). Using these coils in their various possible

combinations produces a signal component in the low frequency range up to a few hundred Hz. TCV also has two internal active stabilization coils (the so-called *G-coils*⁴⁵), supplied by a Fast Power Supply (FPS) operating in the Pulse Width Modulation (PWM) mode with a switching frequency = 10 kHz at its first harmonic. When the G-coils are active, there is a pick-up of the magnetic field that they produce at these relatively high-frequencies. Together with the low-frequency signal components due to the ex-vessel coils, these features are clearly apparent in the non-integrated data and should be removed to facilitate the ensuing analyses.

Similarly to the analysis reported in Ref. 18 for the Mirnov coils, the contribution of these ex-vessel and in-vessel coils can be evaluated for the LTCC-3D measurements during the so-called *stray* and *back-off* discharges, when these coils are individually activated with the pre-defined waveforms (user-programmable for back-off, standard for stray) and no plasma is produced. A stray shot is run daily before plasma operation starts; hence, the estimation of the signal components due to these different ex-vessel and in-vessel coils can be routinely performed.

Figure 13(a) shows the digitized waveforms for the coils' current for the TCV stray shot No. 61857, and Fig. 13(b) shows the result of *low-pass filtering* the raw LTCC-3D data acquired in this discharge for the three sensors in sector 14B as an attempt at removing the signal components due to these currents. The raw data are calibrated for the frequency-dependence and integrated, but the parasitic and mutual coupling between the different measurement axes was not included in this analysis to highlight the contribution of the signal due to the coils' current in all three δB components. The PSD spectrum for the raw data is also shown. There are three main observations to be made.

First, there is a large signal component in $\{\delta B_{VER}, \delta B_{TOR}\}$, and a smaller one for δB_{RAD} , for low-frequencies below the vessel R/L cutoff ~ 300 Hz, due to the activation of the ex-vessel coils, which should be removed from the raw data to avoid drifts and offsets when integrating. This removal is done using a simple fourth order Butterworth high-pass filter with user-selectable cut-off frequency f_c .

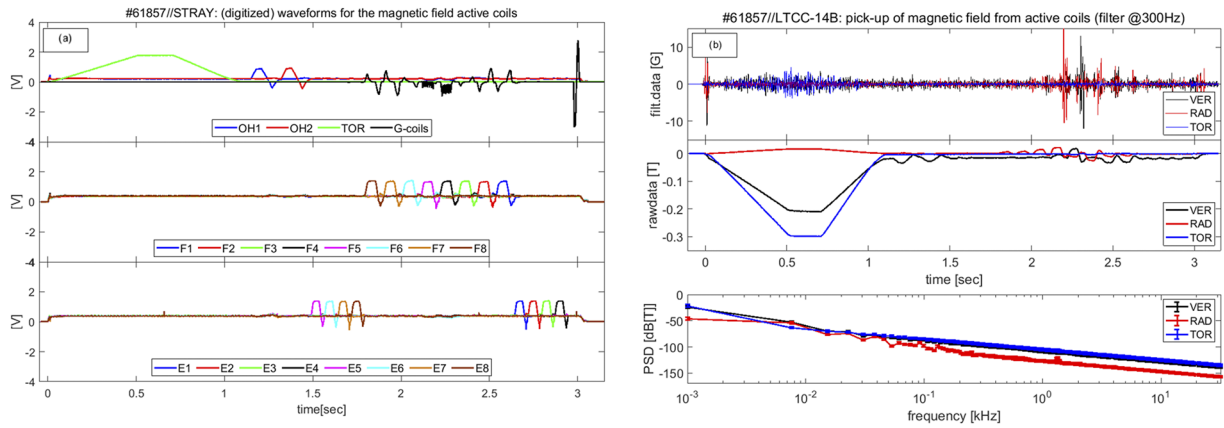


FIG. 13. (a) The digitized waveform for the coils' current for the TCV stray shot No. 61857. These are shown un-calibrated, thus in the range ± 10 V, as in their physical units (A), the range is very different between the coils. (b) The raw, i.e., calibrated and integrated, the corresponding PSD spectrum, and the filtered data for the LTCC-3D measurements for the TCV stray shot No. 61857 for the three sensors in sector 14B. The error bars on the raw and filtered data are not shown, as these would completely be masked by the datasets, but only on the PSD of the raw data.

As shown in this example, using $f_c = 300$ Hz, the filtered signal becomes well-conditioned and can be integrated to highlight the high-frequency components of physics interest (see the top plot in the top frame) for which the typical amplitude ~ 10 G would be completely masked in the raw signal ~ 2 kG.

Second, there is a clear pick-up on the toroidal sensor of the toroidal field waveform in the time window $[0 \rightarrow 1]$ s, with the measured value ~ 0.3 T being in excellent agreement with that produced by the toroidal coils. Note also the small pick-up on the radial and poloidal measurement of the magnetic field induced by the {F4, F5, F6} coils, which are located ex-vessel on the LFS and are the closest to the LTCC-3D sensors. The {OH1, OH2} waveforms are also seen on the poloidal measurements, and the measured poloidal field ~ 0.03 T is in good agreement with that expected.

Third, there is no appreciable signal component at the FPS main switching frequency of 10 kHz and the higher-order harmonics, which is not only due to the relatively large distance between the LTCC-3D sensors and the G-coils (for instance the Mirnov sensors at the same poloidal position of the LTCC-3D sensors show a much larger pick-up), but most importantly to having set up a correct ex-vessel grounding scheme for the DAQ. Conversely, as it will be shown later, there can be a very large pick-up of the FPS and G-coil signals for some of the Mirnov sensors, even those that are away from the G-coils due to an in-appropriate grounding scheme ex-vessel.

Coming back to the simplified approach we have used to account for the mutual coupling between the different measurement axes, we can now confirm the argument previously presented, namely, the need to rely on a different and more efficient algorithm to remove the signal contribution, which is due to the lower-frequency, quasi-DC components in the $\delta B_{MEAS}(\omega, t)$ spectrum, this purpose being served precisely by the analysis presented in this subsection. This is particularly apparent for stray shots during the time window where only the toroidal field coils are activated, as can be seen in Fig. 13(b) for the δB_{VER} and δB_{RAD} measurements.

In this situation, there is only a very small poloidal and radial field component, around 5 mT when also including the image current on the vacuum vessel, and the two δB_{VER} and δB_{RAD} signals are mostly due to the capacitive coupling of the time-varying quasi-DC voltage in the LTCC-3D toroidal measurement circuit since there is a finite dB_{TOR}/dt for the equilibrium field. Due to the distributed nature of the LTCC-3D sensor, the wires for the three measurement axes are in close proximity to each other in certain regions of the assembly, for instance, when the signal from the different modules are brought together to the alumina bars used for connecting the output in-vessel cables, which are ~ 3 cm long and only ~ 1 mm apart. The mutual capacitance C_{MUT} at the sensor (which then includes the contribution of the alumina bars) can be best estimated from the low frequency measurements of the parasitic area, which show a significant drop in the range from 10 Hz to 100 Hz. When using the DC resistance of the sensor, this indicates that $C_{MUT} \sim 300$ μ F. There is also a mutual capacitance at the feedthrough connection, where the two 10 cm long molybdenum pins are only ~ 1 cm apart, but adding a much smaller contribution ~ 10 pF,

$$\begin{aligned}
 NA_{EFF,1}B_{MEAS,1} &= \int dt V_{MEAS,1}(t) \cong c_1 + NA_{PAR,13}B_{MEAS,3} + Z_{DC,1} \\
 &\times \int dt \left(C_{MUT,12} \frac{dV_{MEAS,2}}{dt} + C_{MUT,13} \frac{dV_{MEAS,3}}{dt} \right), \\
 NA_{EFF,1}B_{MEAS,2} &= \int dt V_{MEAS,2}(t) \cong c_2 + NA_{PAR,23}B_{MEAS,3} + Z_{DC,2} \\
 &\times \int dt \left(C_{MUT,21} \frac{dV_{MEAS,1}}{dt} + C_{MUT,23} \frac{dV_{MEAS,3}}{dt} \right), \\
 \int dt V_{MEAS,3}(t) &\approx c_3 + NA_{EFF,3}B_{MEAS,3}. \quad (7)
 \end{aligned}$$

Solving for the capacitive coupling in the quasi-DC frequency limit and in the absence of a direct dB_{MEAS}/dt for the {vertical, radial} measurement axes, we obtain, for the integrated signals, the formulation given in Eq. (7). Here, index 3 indicates the toroidal

measurement axis, while indices {1, 2} are the vertical and radial axes, respectively, we must use the DC values for $\{Z_{\text{MEAS}}, N_{\text{Aeff}}, N_{\text{APAR}}\}$, and $\{c_1, c_2, c_3\}$ are integration constants determined by the condition that at $t = t_0$, when the current in the toroidal coils $I_{\text{TOR}}(t_0) = 0$, we have $B_{\text{MEAS}}(t_0) = 0$. When solving Eq. (7), the expected time traces and flat-top values $\delta B_{\text{VER}} \approx -0.17$ T, $\delta B_{\text{RAD}} \approx +0.014$ T, and $\delta B_{\text{TOR}} \approx -0.32$ T are in excellent agreement with the actual measurements $\delta B_{\text{VER}} \approx -0.21$ T, $\delta B_{\text{RAD}} \approx +0.017$ T, and $\delta B_{\text{TOR}} \approx -0.30$ T for the TCV stray shots.

The data shown in Fig. 13 are used for the calibration, the mutual coupling calculations, and the subtraction of precisely this EM pick-up from the non-integrated signals, which then significantly improves the overall analysis of high-frequency fluctuations. We understand that this is not something ever associated with the high-frequency measurements, and therefore, it is important to show these data precisely to illustrate their importance, thus in a tutorial sense.

D. Calibration of the data in the digital domain

In Subsections VI A–VI C, we have always implicitly used as the first processing step the actual calibration of the data in the digital domain, and it is now important to verify its role. Explicitly, when one considers the measurement chain, it is, in principle, possible to have the data in the correct physical units = [T] by simply considering a purely DC transfer function for the analog system, namely, dividing the raw voltage measurements by the DC gain in the DAQ and the DC value of the effective area, and then integrating.

This approach then completely neglects the frequency dependence of $\text{TFinv}_{\text{E2E}}(z)$, and the simplest method to evaluate if this approach is sufficiently correct is to again consider a stray shot, when the magnetic field waveforms are exactly known, and use the toroidal measurements during the phase when only the toroidal coils are active, thus minimizing the influence of the mutual coupling with the other measurement axes. The *calibrated* data should be in agreement with the magnetic field produced by the toroidal coils.

Again, as for the data shown in Fig. 13 for the EM pick-up of the active field coils, this step is essential to test the correctness of the end-to-end data analysis chain using actual measurements, which is obviously best done when the input signal is exactly known—the equilibrium toroidal field being precisely one such example. Again, we understand that this is not something ever associated with high-frequency measurements, and therefore, it is important to show these data precisely to illustrate their importance, thus in a tutorial sense.

Figure 14 compares the toroidal measurements for the stray shot No. 61857: the raw voltage data are calibrated with and without including the frequency-dependent $\text{TFinv}_{\text{E2E}}(z)$ but do not account for the parasitic and mutual coupling between the different measurement axes. The difference between the expected and the digitally calibrated value of the toroidal magnetic field is ~ 3 mT or, alternatively, $\sim 11\%$, a value that is compatible with NOT having considered the parasitic and mutual coupling terms. Conversely, there is a very clear difference, a factor of $\sim 2.5\times$, between the data obtained with and without applying $\text{TFinv}_{\text{E2E}}(z)$, even for these low-frequency signal components for which the magnitude of the analog $\text{TFdir}_{\text{E2E}}(s)$ is very close to = 1.

This most striking, and perhaps unexpected, difference can be explained as follows: The calibration performed when NOT using $\text{TFinv}_{\text{E2E}}(z)$ simply applies the same $\text{gainDC} = \text{gainDAQ} \times N_{\text{Aeff}}(\text{DC})$ to the raw voltage measurements $X(t_p)$ separately at each individual time point t_p so that the calibrated data are $Y(t_p) = X(t_p)/\text{gainDC}$. When using $\text{TFinv}_{\text{E2E}}(z)$, the *history* of X and Y is considered, as these data are first scaled by gainDC and then *filtered*⁵⁹ using $[Y, Z_{\text{FIN}}] = \text{filter}(B, A, X, Z_{\text{INIT}})$, where $\{B, A\}$ are the numerator and denominator coefficients of $\text{TFinv}_{\text{E2E}}(z)$, of length nb and na , respectively, and $\{Z_{\text{INIT}}, Z_{\text{FIN}}\}$ are the initial and final conditions for the filter's delays. The filter is a *direct form II transposed* implementation of the standard Finite Impulse Response (FIR) difference equation,

$$a(1)y(t_n) = [b(1)x(t_n) + b(2)x(t_{n-1}) + \dots + b(nb+1)x(t_{n-nb})] - [a(2)y(t_{n-1}) + \dots + a(na+1)y(t_{n-na})]. \quad (8)$$

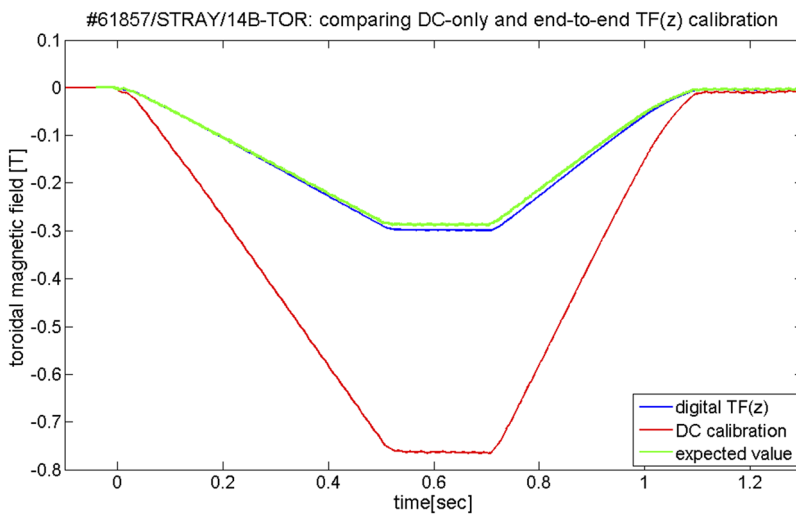


FIG. 14. Comparison between the DC-only and frequency-dependent calibration for the toroidal measurement 14B-TOR for the stray shot No. 61857 during the phase when only the toroidal coils are active, thus minimizing the influence of the parasitic and mutual coupling with the other measurement axes. As a reference, the toroidal field expected at the position of the LTCC-3D sensors is also shown.

From Eq. (8), it is easy to understand mathematically that the DC-only calibration would correspond to having $a(1) = 1 = b(1)$, with all other $\{a, b\}$ coefficients = 0, namely, an analog and correspondingly digital TF_{E2E} with $\text{abs}(TF_{E2E}) = 1$ and $\text{phase}(TF_{E2E}) = 0$ exactly up to frequencies $\gg f_{sDAQ}$. Having such $TF_{E2E}(s)$ means that all poles, zeros, and resonances are also at frequencies $\gg f_{sDAQ}$ so that their effect for frequencies $\leq f_{sDAQ}$ is completely negligible: $\text{abs}(TF_{invE2E}(z)) = 1$ and $\text{phase}(TF_{invE2E}(z)) = 0$. Physically, the frequency-dependent calibration accounts for the fact that at $t = t_p$, the measured signal $X(t_p)$ is the integral over the frequency of the entire spectrum digitized by the DAQ, which is acquired at f_{sDAQ} but contains all frequency components up to $f = \infty$, if not appropriately low-pass filtered. As different components have different time of flights over the line, these were not *born* at the same time in the plasma, and therefore, their *history* is needed to correctly recover the source spectrum. Note that if one low-pass filters the raw data with a sufficiently low cut-off frequency $f_c = O(1 \text{ kHz})$ and then acquires them at $f_{sDAQ} = 2f_c$, then a DC-only calibration is amply sufficient.

Together with the calibration tests shown in Sec. V, this result conclusively demonstrates that a sufficiently accurate evaluation of the mode amplitudes and mode numbers can only be performed when considering the end-to-end frequency-dependent $TF_{invE2E}(z)$ in the digital domain.

E. Overall error analysis for the LTCC-3D measurements

Having now discussed the four main steps of the initial data processing, we can now complete this section of our presentation by putting together all the elements of the error analysis, starting from the best error estimates for the end-to-end inverse transfer function in the digital domain, which were shown in Fig. 9 for the *LDSconv* and *LDSfit* methods.

As the initial step in this analysis, we evaluate the rms error on the δB measurements, which contains a number of contributions. First, we consider the rms error due to the mutual coupling

calculations, typically a very small value $\ll 2 \text{ mV/V}$. Second, we consider the rms error due to transforming the wall-aligned to the field-aligned components, typically an even smaller value $\ll 0.1 \text{ mV/V}$. Third, we consider the error introduced when applying the calibration on the raw voltage data. For this step, we initially add the rms error due to the best estimates on the DC value of NA_{EFF} and NA_{PAR} , and on the DAQ gains. This is the dominant contribution in the rms signal error, since its value is typically around 10 mV/V . Then, we add the frequency dependent calibration errors, best estimated using the uncertainties on the best-fit to the digital $TF_{invE2E}(z)$. These terms are shown in Table III.

Another source of error in the data analysis is the pick-up of spurious signal components (labeled *EM noise* in the following for simplicity) that are associated with different power supplies, both low- and high-voltage, but which are NOT intended to produce a magnetic field in-vessel. In TCV, we consider four different sources for this EM noise, i.e., (1) due to the low-voltage power supplies that are activated during the so-called Plasma Control System (PCS) discharges in TCV, namely, when only the acquisition for the different systems is enabled and (2–4) due to the high-voltage power supplies for the Diagnostic Neutral Beam (DNB), the Neutral Beam Heating (NBH), and the Electron Cyclotron Heating (ECH) systems, respectively, the latter having six gyrotrons operating at the second harmonic (X2, gyrotron No. 1 to No. 6) and three gyrotrons operating at the third harmonic (X3, gyrotron No. 7 to No. 9).

Figure 15 shows the LTCC-3D signals that are measured during a PCS and additional test TCV discharges without plasma (the so-called *back-off* shots) where the DNB, NBH, and ECH- $\{X2, X3\}$ are activated during different time windows when no magnetic field is present. This figure shows the rms signal level and its frequency spectrum, which was calculated using an Auto-Regressive (AR) model of order 100 for the PSD (i.e., attempting to find at least 50 possible peaks in the PSD signal). In Fig. 15, we also show for comparison the signal acquired by the *blind probe*, which is a very small winding loop (with a surface area $\sim 1 \text{ cm}^2$ aligned along the toroidal direction) sitting just at the in-vessel side of a feedthrough at the bottom of the tokamak. This signal is acquired together with

TABLE III. The relative error due to the mutual coupling calculations (MC), the transformation from wall-aligned to field-aligned components (WA to FA), and the relative calibration error due to the uncertainties on the DC value of NA_{EFF} , NA_{PAR} , and the DAQ gains, labeled *calDCgain*. For illustrative purposes, we also indicate the maximum rms relative error associated with the best-fit to the frequency-dependent, end-to-end measured analog $TF_{dirE2E}(s)$ and digital $TF_{invE2E}(z)$. For some signals, the relative error on $TF_{dirE2E}(s)$ is very small and does not have a strong frequency dependence; hence, it is labeled *typical* (and shortened as *typ.*) in a certain frequency range. For estimating the maximum rms relative error on $TF_{invE2E}(z)$, we do not consider the frequency range $> 0.85 \times f_{sDAQ}/2$, where divergences intrinsically occur in the modeling of $TF_{invE2E}(z)$.

Signal name	rms level MC (mV/V)	rms level WA to FA (mV/V)	rms level calDCgain (mV/V)	max (RelErr) $TF_{dirE2E}(s)$	max (RelErr) $TF_{invE2E}(z)$
02B-VER	± 0.70	± 0.05	± 11.30	Typ. $\pm 0.02 > 100 \text{ kHz}$	$\pm 0.15 @ 280 \text{ kHz}$
02B-RAD	± 0.10	± 0.05	± 11.14	Typ. $\pm 0.02 > 100 \text{ kHz}$	$\pm 0.19 @ 380 \text{ kHz}$
02B-TOR	± 0.10	± 0.03	± 12.26	Typ. $\pm 0.02 > 100 \text{ kHz}$	$\pm 0.07 @ 570 \text{ kHz}$
14B-VER	± 1.60	± 0.05	± 11.47	Typ. $\pm 0.02 > 100 \text{ kHz}$	$\pm 0.16 @ 103 \text{ kHz}$
14B-RAD	± 0.10	± 0.05	± 12.57	$\pm 0.03 @ 413 \text{ kHz}$	$\pm 0.21 @ 268 \text{ kHz}$
14B-TOR	± 0.40	± 0.03	± 13.39	$\pm 0.16 @ 682 \text{ kHz}$	$\pm 0.19 @ 682 \text{ kHz}$
16A-VER	± 1.00	± 0.05	± 11.41	Typ. $\pm 0.02 > 100 \text{ kHz}$	$\pm 0.09 @ 568 \text{ kHz}$
16A-RAD	± 0.10	± 0.05	± 8.87	Typ. $\pm 0.02 > 100 \text{ kHz}$	$\pm 0.08 @ 561 \text{ kHz}$
16A-TOR	± 0.20	± 0.03	± 10.24	$\pm 0.05 @ 515 \text{ kHz}$	$\pm 0.08 @ 589 \text{ kHz}$

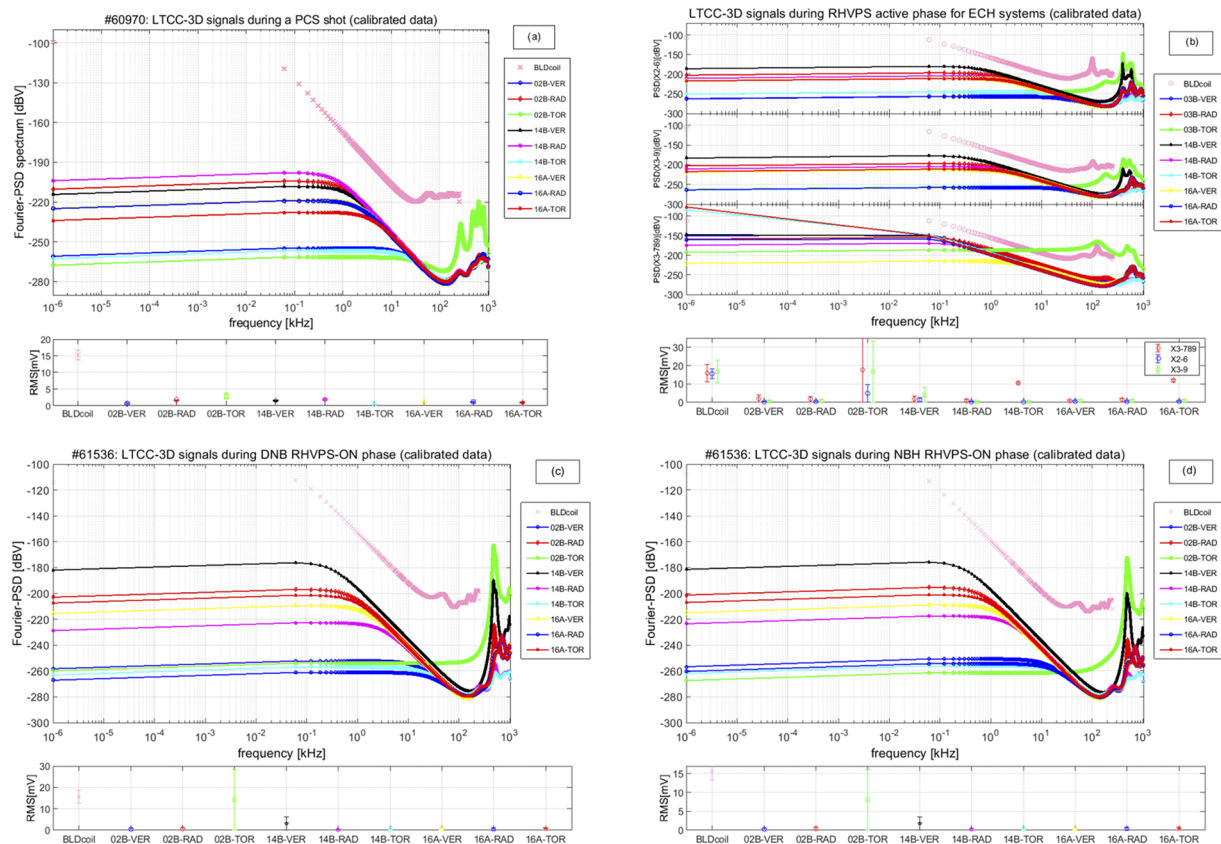


FIG. 15. The LTCC-3D signals measured during a PCS and additional back-off discharges without plasma, where the DNB, NBH, and ECH(X2, X3) systems are separately activated during different time windows when no magnetic field is present. These data show a typical value for the EM noise level on the LTCC-3D signals that must be compared with the actual measurements of the frequency spectrum of magnetic fluctuations to evaluate how much of the LTCC-3D signal could be due to the pick-up of this EM noise. We find that overall the level of this EM noise is sufficiently small for all signals and much lower than the test level for the blind probe. There are, however, some exceptions at certain frequencies (see, for instance, the clear peaks in the PSD around 450 kHz, most notably for 02B-TOR), and these must be addressed correctly in the ensuing data analysis.

the other Mirnov probes and saddle loops in the signal processing room, ~35 m (cabling length) outside the tokamak hall, and has a different earthing arrangement from the LTCC-3D sensors. The blind probe signal was previously used to estimate the EM noise level for the TCV Mirnov sensors.¹⁸

Table IV then shows the summary results for the estimated rms error on the raw data for the LTCC-3D sensors when considering these four sources of EM noise separately.

First, we consider a PCS shot, showing the end-to-end signal level corresponding to EM noise in the DAQ due to electronics and low-voltage power supplies. The rms signal level is very small, well below ± 3 mV. The frequency spectrum is flat (white noise) with a value around -200 dBV for frequencies below 1 kHz and then drops with a $1/f$ dependence (pink noise) to around -280 dBV for frequencies up to ~ 200 kHz. The increase in the PSD for higher frequencies is due to a deteriorating Common Mode Rejection Ratio (CMRR), and this feature will be discussed in more detail in Sec. VII A. The data for the 02B-TOR sensor are noisier and spikier than the other

LTCC-3D signals for frequencies above ~ 300 kHz but still remain below -220 dBV, which is of no particular concern for the ensuing data analysis. Finally, the signal level in the blind probe is significantly higher than that on the LTCC-3D sensors, and this is believed to be due to the different earthing arrangement.⁶⁰

Second, we consider back-off discharges during the time windows where only the ECH systems were activated. These systems are powered through 80 modules arrayed in parallel working with a dominant 5 kHz PWM carrier frequency, shifted between the different modules, so that, in principle, all 5 kHz harmonics between the dominant $= 5$ kHz and 80×5 kHz $= 400$ kHz could be present in the frequency spectrum measured by the magnetic sensors. In fact, the 100 kHz harmonic is clearly seen in the frequency spectrum for the blind probe, but much less on the LTCC-3D sensors. We note that when comparing different ECH systems, the pick-up of this EM noise is not purely additive and depends on which specific (combination of) gyrotron(s) has been activated. This is particularly clear comparing the 02B-TOR measurement, which is very sensitive to

TABLE IV. Estimated rms error on the raw data for the LTCC-3D sensors. This takes into account the (absolute) noise level during PCS shots (only the low-voltage power supplies for the acquisition systems are activated) and during back-off shots when only the HV sources for the DNB, NBH, and the ECH-{X2, X3} systems were separately activated in the absence of magnetic fields and plasma. For comparison purposes, the same measurements are also presented for the blind probe.

Signal name	rms level PCS shot (mV)	rms level DNB phase (mV)	rms level NBH phase (mV)	rms level ECH-X2-6 (mV)	rms level ECH-X3-9 (mV)	rms level ECH-X3-789 (mV)
02B-VER	± 0.63	± 0.44	± 0.28	± 0.23	± 0.49	± 1.96
02B-RAD	± 1.67	± 0.58	± 0.43	± 0.38	± 0.64	± 1.72
02B-TOR	± 2.90	± 14.15	± 8.03	± 4.79	± 16.69	± 17.54
14B-VER	± 1.48	± 3.10	± 1.84	± 1.28	± 4.12	± 1.28
14B-RAD	± 1.98	± 0.21	± 0.22	± 0.29	± 0.29	± 0.80
14B-TOR	± 0.60	± 0.16	± 0.15	$\pm 0.17V$	± 0.17	± 10.53
16A-VER	± 1.11	± 0.55	± 0.38	± 0.78	± 0.78	± 0.64
16A-RAD	± 1.13	± 0.50	± 0.32	± 0.71	± 0.71	± 1.23
16A-TOR	± 0.94	± 0.57	± 0.40	± 0.46	± 0.72	± 11.93
Blind probe	± 15.27	± 15.60	± 15.42	± 15.56	± 16.67	± 15.76

gyrotron No. 9 being activated, while the 14B-TOR measurement is not. Overall, and with these two notable exceptions, the rms signal level is relatively small, and the frequency spectrum has features similar to those observed during PCS discharges, specifically again being much smaller than that picked-up by the blind probe.

Finally, we consider back-off discharges during the time windows where only the DNB and NBH systems were separately activated. There is a clear frequency component around 430 kHz in the frequency spectrum but overall, with the exception of the 02B-TOR measurement, the rms signal level is very small and the frequency spectrum has features similar to those already mentioned.

For the data analysis for the selected TCV discharge and time window, the overall rms (absolute and relative) error is estimated using tabulated values for the PCS signals (as given in Table IV: these measurements are very reproducible; hence, this approach is sound and computationally much faster than using, for instance, the actual data for the closest PCS shot) and for the DC errors on NA_{EFF} , NA_{PAR} , the DAQ gains, and the different terms contributing to the mutual coupling calculations (as given in Table III). This best-estimate for the rms error is used for the data in the time domain.

The frequency-dependent (absolute and relative) error is then determined using tabulated values for the PSD of the PCS signals and for the best-fit errors on $TFin_{VE2E}(z)$. This error is used for all analyses in the frequency domain, for instance, providing confidence intervals for the PSD estimates and absolute errors on the total signal and individual mode amplitudes in Fourier space. However, due to the intrinsic variability in the operating conditions for the DNB, NBH and ECH systems, it is not possible to consistently use similarly tabulated values for an equivalent background subtraction for the LTCC-3D measurements when these systems are activated. The approach that has been taken is that of comparing the pre-determined PSD spectrum of the EM noise for these systems with that of the actual LTCC-3D measurements to visually evaluate, and then correspondingly subtract *ad hoc*, how much of the LTCC-3D signal could be due to the pick-up of this EM noise.

Finally, there are additional signal components due to the pick-up of the (quasi-DC, but varying in time) equilibrium magnetic field provided by the ex-vessel coils and of that driven by the in-vessel G-coils for the fast control of plasma instabilities. While the quasi-DC pick-up components can be very efficiently removed, when required, using a high-pass filter as described in Sec. VI C, the contribution from the G-coils cannot be exactly subtracted on-the-fly, as the sampling frequency is completely different (10 kHz for the G-coil data, 125 kHz for the FPS data, and 2 MHz for the LTCC-3D data). The current and voltage signals for the FPS are also very noisy; hence, a direct interpolation and extrapolation would be useless to perform an equivalent *background subtraction* for each time point. The approach that has been taken is that of using the pre-determined Green functions⁴⁶ to obtain the nominal [T/A] magnetic field components at the position of the LTCC-3D sensors, then include the contribution of the magnetic field due to image currents on the vacuum vessel, and then compare the PSD spectrum of these magnetic field components with that of the LTCC-3D measurements over the same time window. As per the {ECH, DNB, NBH} sources of EM noise, this allows us to evaluate the pick-up of the G-coils and other active coils, by the LTCC-3D sensors, and then correspondingly subtract these terms.

VII. SYSTEM MEASUREMENT PERFORMANCE

The main purposes of the LTCC-3D measurements are that of providing information on the higher frequency components (both coherent eigenmodes and, perhaps even more importantly, background incoherent fluctuations) for the vertical and radial magnetic field components, for which other measurements exist on TCV but with a lower bandwidth, and unique data for these fluctuations in the toroidal field component, for which no other diagnostic exist in TCV (or in other tokamak, to our knowledge). As the frequency increases, it is expected that the signal amplitude will drop significantly, and therefore, it is important to assess whether the measurement bandwidth that has been determined using the work on the end-to-end system calibration in the analog domain is actually still applicable when considering the signal to noise ratio in different frequency

ranges. This work is reported in this section, where we focus on three main elements: the CMRR analysis, the tests on the correct detection of modes, and finally the comparison of the data acquired for the δB_{POL} field component by Mirnov and LTCC-3D sensors located at the same poloidal position (but at different toroidal positions) in the frequency range where the bandwidth of these two systems overlaps.

A. The CMRR measurements, and comparison with the standard Mirnov sensors on TCV

The first important step in assessing the overall measurement performance of the LTCC-3D sensors is that of determining the sensitivity to the pick-up of EM noise, including that above f_{NYQ} , and this is best assessed using the CMRR measurements. Figure 16 shows the measurement setup and the CMRR results: here, we define $CMRR(dB) = 20 \times \log_{10}(\text{gain}_{DM}/\text{gain}_{CM})$. The LTCC-3D acquisition has a much higher CMRR than that for the Mirnov sensors, which is likely to be due to a combination of more modern electronics (that for the Mirnov sensor is ~20 years old) and a single earthing point at the torus potential for the LTCC-3D system, vs aging of components and a complex multi-point earthing arrangement for the Mirnov DAQ.

The consequence of the latter contribution to the CMRR for the Mirnov DAQ is a much larger surface area from which spurious CM signal components can be captured. The CMRR for the LTCC-3D system drops from a relatively constant value > 70 dBV

up to ~300 kHz to ~50 dBV at ~2.3 MHz (i.e., above $2 \times f_{NYQ}$ for the LTCC-3D system). For the Mirnov sensors, the CMRR is only ~40 dBV for frequencies < 10 kHz and drops to ~25 dBV at ~600 kHz, i.e., at a comparable value of the frequency with respect to the maximum $f_{NYQ} = 250$ kHz for this system. In particular, at frequencies where we find AEs in TCV, namely, in the 100 kHz–400 kHz range, the CMRR for the Mirnov sensors is ~20 dBV, while it is better than 70 dBV for the LTCC-3D sensors. We conclude that the LTCC-3D DAQ is better performing at rejecting CM signal components, even at frequencies above f_{NYQ} , and this is clearly beneficial for the high-frequency measurements that are the target of this system.

B. Testing the correct detection of modes

A second point in assessing the system measurement performance is the ability of *correctly detecting* individual components in the frequency spectrum of magnetic instabilities in the plasma. The [supplementary material](#) (Sec. I) illustrates in detail the computational aspects of this analysis, some of which are rather complex.

In summary, we generate a time series using a combination of a continuous spectrum with spectral breaks, various eigenmodes, spurious peaks due to the pick-up of EM noise from power supplies working in the PWM mode, and frequency-dependent diagnostic noise normalized to contain a certain fraction of the total energy

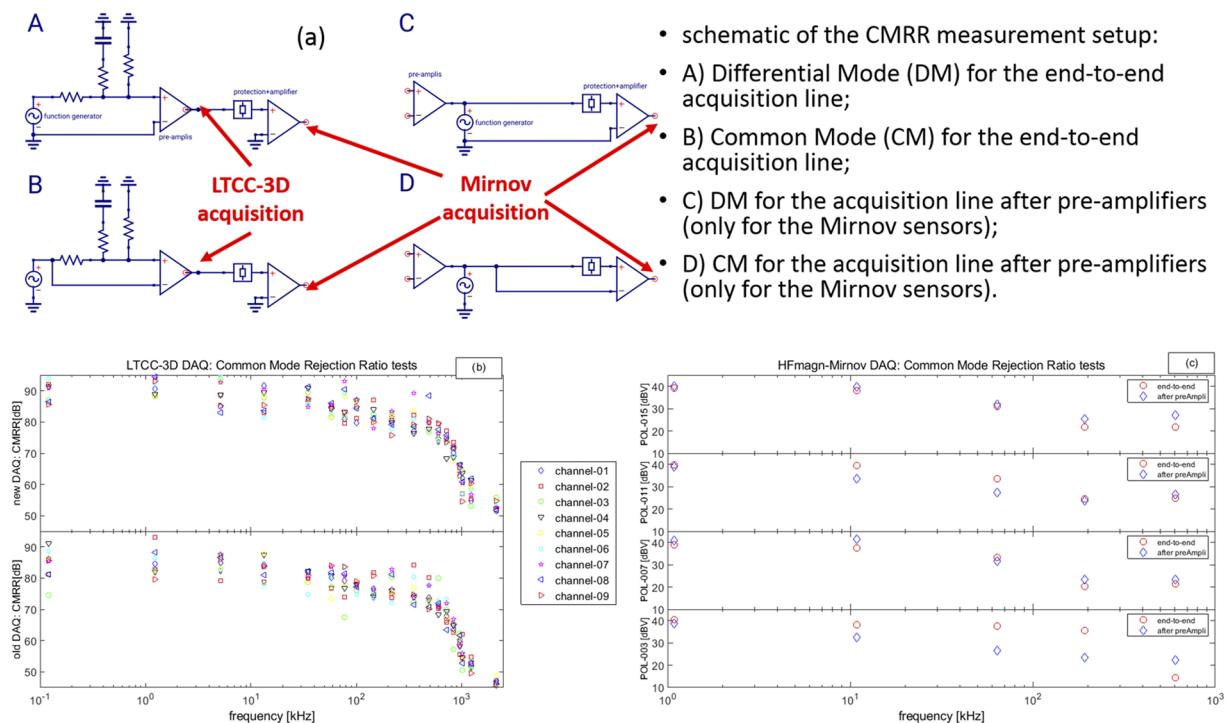


FIG. 16. (a) Setup for the CMRR measurements, obtained by feeding a voltage source at the input of the ex-vessel cabling after removing the connection at the feedthrough and collecting the data at the output of the d-Tacq cards. (b) Measurements for the CMRR for the LTCC-3D sensors; for comparison purposes, the CMRR data are also shown for the four groups of Mirnov sensors (c), which are grouped by the toroidal sector in which their pre-amplification crate is located in the TCV tokamak hall.

content in the continuous part of the input signal. The PSD-AR method is then used to detect the peaks in the signal, and their frequency and amplitude are matched to the input values to determine the overall success of the simulation, labeled *score*. The score is set to be 1.00 for perfect detection and is penalized as the square of the relative difference in the frequency and amplitude for each mode, with a further penalization for the overall score proportional to the number of *missed* peaks, i.e., eigenmodes in the input model signal that are NOT detected by the PSD-AR method.

In summary, Fig. 17 shows the score for individual mode frequencies covering the entire DAQ Nyquist range for the δB_{VER} measurements [those for the $\{\delta B_{\text{RAD}}, \delta B_{\text{TOR}}\}$ measurements and the run-time simulation parameters common to all simulations are shown in the [supplementary material](#) (Sec. I)], with the corresponding mode amplitudes set to vary in the range of the actual measurements. These results are averaged over a set of simulations that were performed varying the fractional energy content of the diagnostic noise between $[5 \times 10^{-3} \rightarrow 5 \times 10^{-2}]$. Twenty simulations were run for each pair of input modes {frequency, amplitude} in all cases including all sources of EM noise and using the *gray22* frequency dependence for the diagnostic noise.

For individual eigenmodes, the detection score improves with the mode frequency and amplitude: this analysis allows estimating the confidence in these quantities when analyzing real data. The detection score drops to <0.35 for mode amplitudes below ~ 1 mG and/or for mode frequencies for which the width of the peak is incorrectly estimated in the PSD. In these situations, the detection score has a large scatter even at the higher frequencies in this scan, which is clearly indicative of a significant sensitivity on the overall noise content (the fractional energy with respect to that in the continuum spectrum) and on its exact frequency spectrum.

C. Comparison with the Mirnov sensors for δB_{POL} measurements: The sawbones

To conclude this section on the evaluation of the measurement performance for the LTCC-3D magnetic diagnostic system, it is useful to compare the δB_{POL} measurements with those obtained with the standard Mirnov sensors located at the same poloidal but at a different toroidal position. A particularly illustrative example is provided by the sawbone, as this mode typically has multiple frequency components but only one dominant toroidal component at each mode frequency, and hence, the mode amplitude should be the same, within the uncertainties of the measurements, as a function of the toroidal position of the different sensors. This comparison is also statistically relevant as we have $3 \times$ LTCC-3D measurements and $6 \times$ corresponding Mirnov measurements of δB_{POL} .

As an example of this comparison, we can use the TCV discharge No. 55542, which has clear sawbones and has combined {NBH, ECH-X2 and ECH-X3} heating. Figure 18 shows the main plasma parameters and heating waveforms for this discharge, which will be repeatedly used in this work for physics analyses. Figures 19 and 20 then show the time series and the poloidal amplitude structure for one particular sawbone detected in the TCV discharge No. 55542. The LTCC δB_{POL} measurement in sector 02B is shown, in comparison with two Mirnov δB_{POL} measurements in sectors 03B and 15B (the closest toroidally), respectively. While for the first harmonic at ~ 25 kHz the agreement is excellent, discrepancies in the time series are evident and increasing for the second and third harmonics at ~ 50 kHz and ~ 75 kHz, respectively. This mode shows strong ballooning characteristics for the first and second harmonics. This is much less evident for the third harmonic, as the signal/noise ratio is very poor for the Mirnov data. For a correct comparison

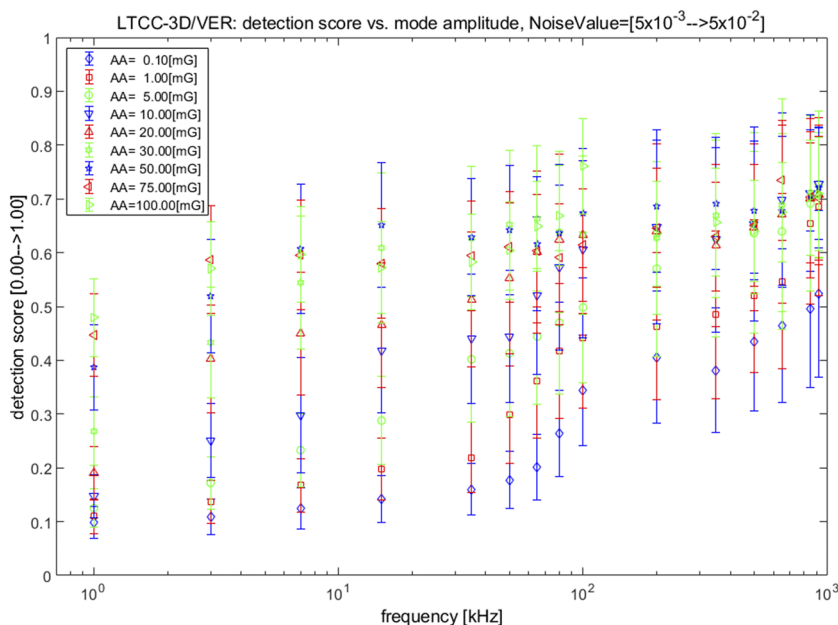


FIG. 17. The score for individual mode frequencies covering the entire DAQ range, with the corresponding mode amplitudes set to vary in the range of the actual measurements. The values of the error bar on the score are the {rms, STD} over the 20 simulations that were run for each pair of input modes {frequency, amplitude}.

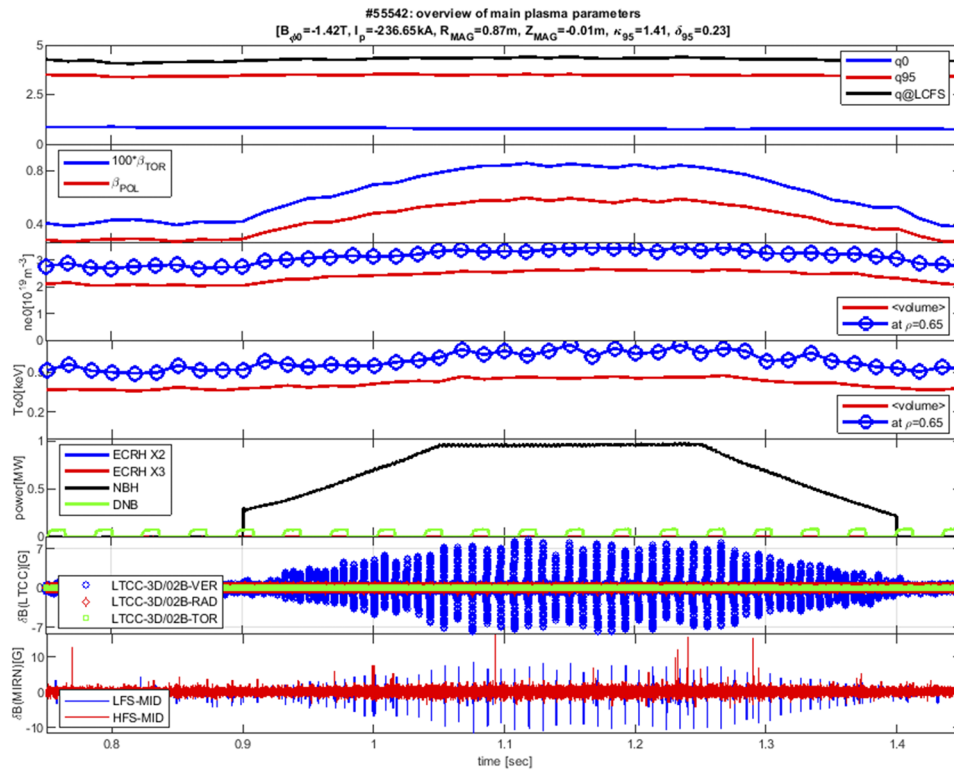


FIG. 18. The main plasma parameters for the TCV discharge No. 55542. The toroidal magnetic field and plasma current are $B_\phi = -1.42$ T and $I_p = -237$ kA, respectively; the plasma is centered at $Z_{MAG} \sim -0.1$ cm and has elongation $\kappa_{95} = 1.41$ and triangularity $\delta_{95} = 0.23$ at $\rho_{POL} = 0.95$. The sawbones are clearly visible, and the location of the $q = 1$ surface is $\rho_{POL} \sim 0.67$.

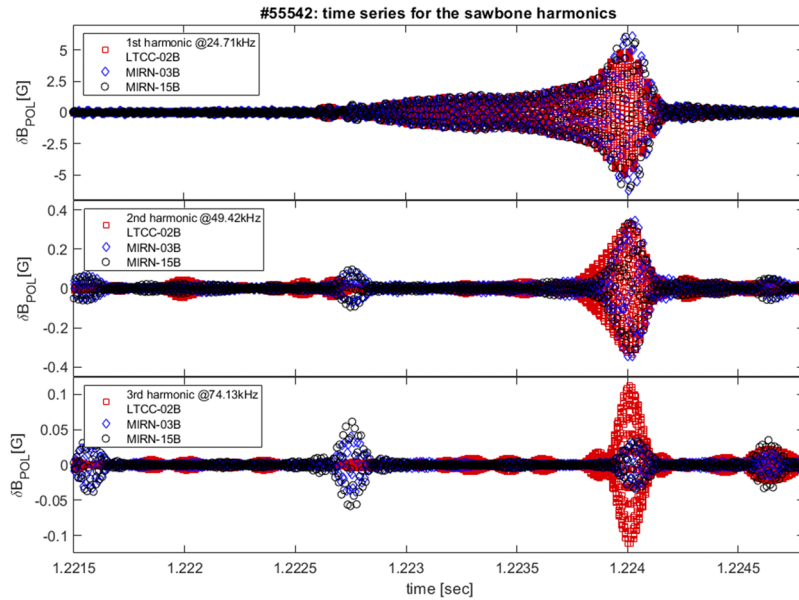


FIG. 19. Time series for one particular sawbone measurement for No. 55542: the data shown here are band-pass filtered at the frequencies of the three sawbones' harmonics, as determined using a PSD-AR analysis of the measurements, including the frequency width of the modes, $\sim \pm 5$ kHz. The bursts seen on the Mirnov data, particularly on sector 15B, at $t \sim [1.2215, 1.2227, 1.2247]$ s, are due to the pick-up of a partial arc-discharge to GND from the RF source of the DNB power supply, which indeed sits in sector 15.

between the Mirnov and LTCC δB_{POL} measurements, it is therefore important to account for the finite and different extension of the sensors, as (a) the mode amplitude strongly varies on the LFS around the position of the probes.

This is further complicated by two geometrical contributions, which also need to be accounted for (b) the angle between the poloidal field-aligned and the vertical probe-aligned directions and (c) the distance between the LCFS and the probe along the

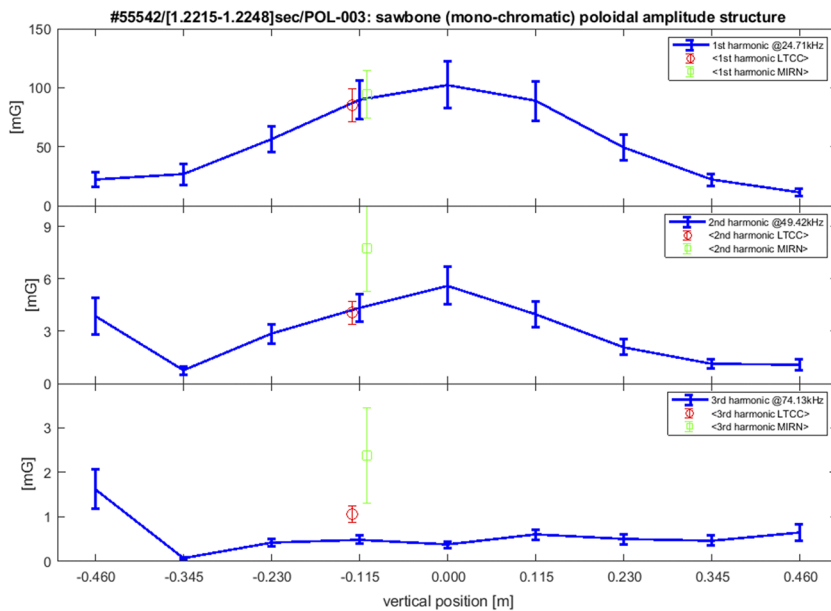


FIG. 20. Poloidal amplitude structure for the sawbone measurement shown in Fig. 19, using the LFS Mirnov measurements in sector 003 and comparing the data with the average mode amplitude and its scatter, shown as a vertical error bar for the $3\times$ LTCC and the $6\times$ Mirnov δB_{POL} measurements. The signal at $Z = -0.460$ m is due to the pick-up of the magnetic field from the very close-by G-coils, which are powered by the FPS in the PWM mode, hence showing strong signal components at integer multiples of $10\text{ kHz} \pm 1\text{ kHz}$. Due to the rapidly deteriorating CMRR for the Mirnov-DAQ for frequencies $>30\text{ kHz}$, the pick-up of the G-coil (and, in general, of all sources of EM noise) signal becomes progressively more apparent as the mode frequency increases.

normal to the LCFS, both terms changing over the finite and different extension of the sensors. The time series data shown in Fig. 19 only account for (b) + (c), while the frequency analysis shown in Fig. 20 also includes (a).

While for the first harmonic at $\sim 25\text{ kHz}$ the agreement between the Mirnov and LTCC δB_{POL} measurements is really excellent, discrepancies in the time series and monochromatic FFT amplitude (namely, the FFT signal integrated over the frequency width of the mode) become evident and are increasing for the second and third harmonics at $\sim 50\text{ kHz}$ and $\sim 75\text{ kHz}$, respectively. It is particularly striking that the scatter in the average amplitude measurements is practically the same for the first harmonic at $\sim 25\text{ kHz}$, while it becomes very different, specifically much larger and strongly increasing with frequency for the Mirnov but remains practically constant for the LTCC measurements.

This has prompted a very detailed investigation of the sources of this larger and frequency-dependent scatter in the data, both using actual measurements on plasma and back-off discharges and installing additional hardware. Figure 21 shows the comparison of the FFT monochromatic mode amplitude in the frequency ranges where modes can be observed on both the LTCC-3D and Mirnov δB_{POL} sensors. The ratio of the mode amplitudes, and its scatter, very strongly increases with the frequency for the un-corrected measurements. When accounting only for the ballooning mode structure averaged over the poloidal extension of the sensor, a sufficient agreement is obtained up to moderately high-frequencies $\sim 30\text{ kHz}$, as shown for the sawbone test case. However, above $\sim 50\text{ kHz}$ only when also including the pick-up of overall EM noise, the δB_{POL} measurements agree within $\pm 20\%$, i.e., the desired measurement accuracy on the mode amplitude. Conversely, above $\sim 50\text{ kHz}$, it is only with a very cumbersome and time consuming analysis procedure that the EM noise can be subtracted from the

Mirnov data. When accounting for the finite and different poloidal extension of the sensors, it can then be shown that the Mirnov and the LTCC-3D δB_{POL} measurements are in quantitative agreement up to $\sim 100\text{ kHz}$, the signal/noise ratio being then often too poor for the Mirnov signals to compare meaningfully the data at higher frequencies.

It is important to remark that on TCV, we have ~ 200 Mirnov sensors providing δB_{POL} measurements that work well up to $\sim 30\text{ kHz}$, their main limitations for providing reliable data on the amplitude of magnetic fluctuations at higher frequencies being the first set of pole (f_p) and zero (f_z) frequencies in their DAQ at [$f_p \sim 95\text{ Hz}$, $f_z \sim 3.5\text{ kHz}$], which cause a signal attenuation of $\sim 1/40$ above f_z , and the deteriorating CMRR for frequencies $>30\text{ kHz}$. There is therefore absolutely no need for the further $3\times$ LTCC δB_{POL} measurements in this relatively low frequency range up to $\sim 30\text{ kHz}$. Therefore, for practical purposes, we use the Mirnov sensors for magnetic fluctuation analyses up to $\sim 30\text{ kHz}$, where indeed the large majority of the TCV data are obtained. It is only recently, with the installation of the NBI system, that higher frequency coherent modes have been observed on TCV, even up to $\sim 400\text{ kHz}$, and it is for their analysis, and for the analysis of incoherent broadband magnetic fluctuations up to the MHz range, that the LTCC-3D measurements of δB_{POL} are used.

As stated in Sec. I, the third most important aspect of the work intended at optimizing the measurement performance of the LTCC-3D magnetic diagnostic system lies in (c) making sure that the single-axis equivalent measurements are efficiently and correctly decoupled from each other. For “correctly,” we now understand that the LTCC δB_{POL} measurements have to be in good agreement with the standard Mirnov measurements in the frequency range where we can meaningfully compare them. This defines a second criterion for satisfying the requirement (c), and this analysis shows that this criterion has also been met.

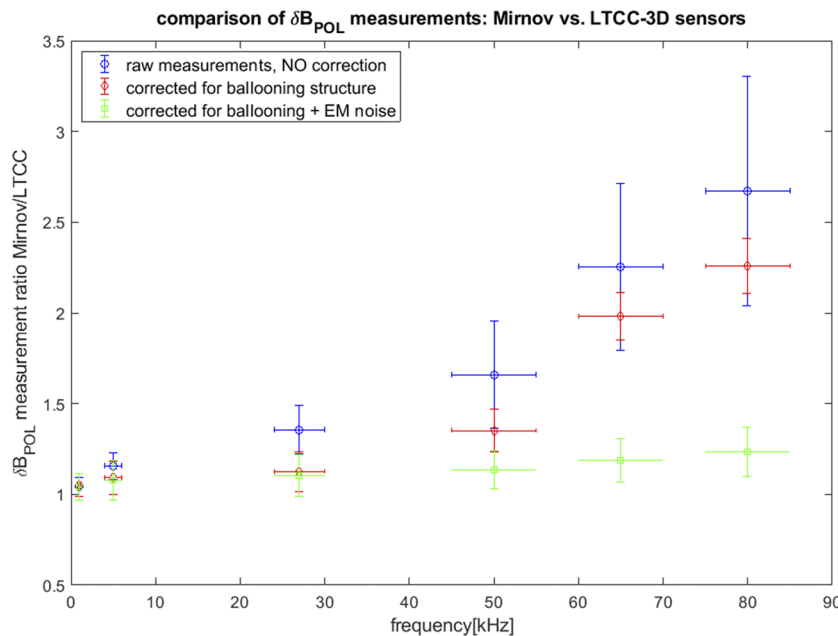


FIG. 21. Comparing the typical FFT monochromatic mode amplitude in different frequency ranges where modes can be seen sufficiently clearly on both LTCC and Mirnov δB_{POL} sensors.

VIII. SOME SELECTED INITIAL RESULTS

Having verified the overall measurement capabilities of the LTCC-3D sensors, we can now proceed to show some selected initial results, focusing specifically on measurements that would not be otherwise available on TCV.

A. A mini saddle loop: High frequency measurements of the δB_{RAD} component

In TCV, we have three sets of $8 \times$ saddle loops, located on the LFS at equi-spaced toroidal locations and centered at the vertical position = $[+0.335, 0.00, -0.335]$ m. The saddle loops are directly mounted on the wall and, therefore, have a bandwidth comparable to the inverse of the vessel current penetration time, thus typically providing measurements of δB_{RAD} at the most only up to ~ 3 kHz depending on the poloidal mode structure of the instability. The saddle loops are therefore specifically useful for detecting very low-frequency modes that may eventually become locked.

Similarly to the δB_{POL} measurements, the $3 \times$ LTCC δB_{RAD} sensors are not intended to provide additional results on such low frequency, possibly locked, modes with respect to those obtained with 24 saddle loops but are useful to provide information of the perturbation to the radial magnetic field component for higher frequency modes for which the saddle loops cannot be used.

One example already presented for otherwise unavailable measurements of δB_{RAD} is the sawbone instability, these data having already been shown in Fig. 11. An additional example is that of the relatively low-frequency TMs that are routinely obtained in TCV in the absence of NBI: these TMs have a frequency of typically $\sim [2 \rightarrow 5]$ kHz and thus often are not picked-up by the saddle loops.

Figure 22 shows an example of such measurements for an $m/n = 2/1$ TM slowly frequency sweeping from ~ 4 kHz to ~ 3 kHz: δB_{POL} is clearly observed on the Mirnov sensors, but δB_{RAD} is not seen on the saddle loops, only on the LTCC-3D sensors. This measurement allows us to determine the ratio between the amplitude of the perturbation to the different field component, in this particular case being $\delta B_{RAD}/\delta B_{POL} \sim 0.12$, practically constant in this rather small frequency range. Additionally, it also informs us on the upper limit to the bandwidth of the TCV saddle loops associated with their mounting directly on the wall, which clearly cannot exceed 3 kHz. These data then confirm one of the main goals of this work, namely, obtaining otherwise unavailable 3D measurements of the magnetic fluctuations, irrespective of their frequency range.

B. Perturbation of the toroidal field: High frequency measurements of the $\delta B_{||}$ component, and theoretical model for this result

TCV, and to our knowledge other tokamaks as well, was not previously equipped with inductive sensors measuring the perturbation to the toroidal field, the main practical reason being that this is a very problematic measurement as the raw voltage data are likely to be dominated by the pick-up of the equilibrium toroidal field. Furthermore, it is only recently that theoretical models⁴⁷ have shown that in the absence of a finite $\delta B_{||}$, certain classes of instabilities, essentially pressure-driven modes, are artificially stabilized by magnetic compression due to the energy required to bend the field lines.

Finally, from a purely theoretical point of view,⁴⁸ a finite $\delta B_{||}$ can, in fact, exist primarily due to the presence of a finite pressure gradient ∇p at the plasma edge, since $\delta B_{||} = \xi_{\perp} \cdot \nabla p - \mathbf{B}_0 \cdot [\nabla \xi_{\perp} + 2\xi_{\perp} \cdot \nabla \mathbf{B}_0]$, with ξ_{\perp} being the radial MHD displacement ($\xi_{\perp} = \nabla \times (\xi \times \mathbf{B}_0)$ with \mathbf{B}_0 the equilibrium (quasi-toroidal) magnetic field) and

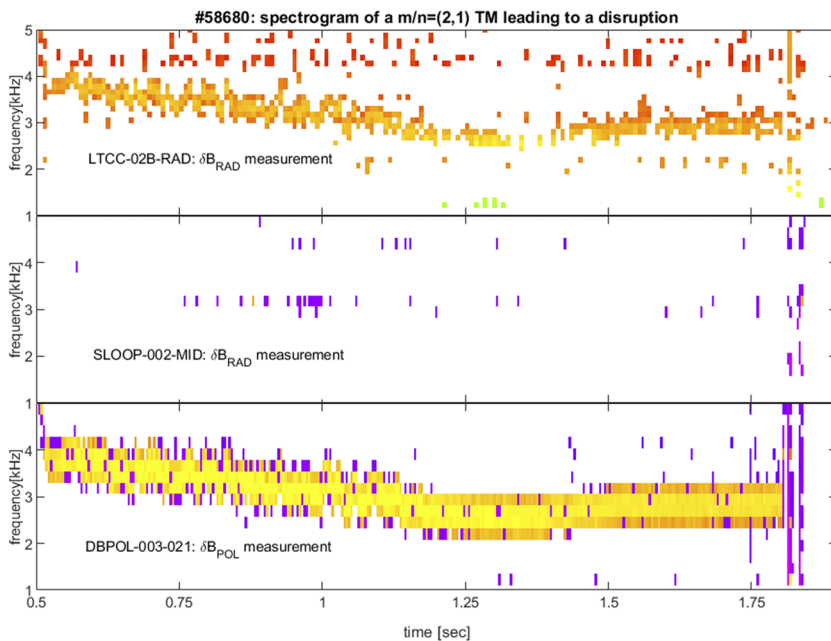


FIG. 22. Spectrogram for a $m/n = 2/1$ TM. The δB_{POL} component is clearly observed on the Mirnov sensors, but the δB_{RAD} component is not seen on the saddle loops, only on the LTCC-3D sensors.

$\kappa = (1/B^2)(\mathbf{B}_0 \cdot \nabla)\mathbf{B}_0$ being the field line curvature. Note that here the additional term $[\nabla\xi_L + 2\xi_L \cdot \kappa]$ in the expression for $\delta B_{||}$ is a stabilizing term that can, in principle, be set to $= 0$ when minimizing the MHD energy functional for the fast magnetosonic waves, as this corresponds to the energy needed for field compression, which also holds true for the fishbone instability, hence also for the sawbones.

In TCV, the closest proxy to a truly field-aligned $\delta B_{||}$ measurement is provided by the δB_{TOR} data obtained with the LTCC-3D sensors. As clear from Figs. 13(b) and 14, these measurements do obviously show a strong pick-up of the equilibrium toroidal field as produced by the PS of the toroidal field coils, and therefore, the δB_{TOR} data are only useful for frequencies above a few hundred Hz. In most cases, the δB_{TOR} signal at the frequencies for which clear modes are seen on the $\{\delta B_{POL}, \delta B_{RAD}\}$ components is just showing a continuous spectrum without peaks, hence indicating that $\xi_L \cdot \nabla p \sim 0$ or $\xi_L \cdot \nabla p = \mathbf{B}_0[\nabla\xi_L + 2\xi_L \cdot \kappa]$ at the plasma edge for those modes. This occurs, for instance, for the usual current-driven, core-localized TMs observed in TCV. The most notable occurrence of a δB_{TOR} measurement is again the case of the sawbone instability, and illustrative results are shown in Fig. 23. As for the results shown in Sec. VIII B, these data then further confirm one of the main goals of this work, namely, obtaining otherwise unavailable 3D measurements of the magnetic fluctuations, irrespective of their frequency range.

C. High frequency components in the δB_{POL} spectrum, not measurable with Mirnov probes

As a first illustrative example of the data that can be obtained with the LTCC-3D sensors and that could have not been otherwise obtained with the Mirnov sensors, we show recent measurements of coherent magnetic fluctuations in the Alfvén frequency range

during combined NB and EC-X2 heating discharges. Figure 24 shows the measurements obtained in No. 62117, where weak instabilities in the TAE frequency range @180 kHz and even weaker in the EAE frequency range @350 kHz were observed with the LTCC-3D sensors.

These modes start during the ohmic phase of the discharge before the ECH-X2 is switched on at $t = 0.5$ s and continue throughout the first 3 NBH pulses at $t = [0.70 \rightarrow 0.80]$ s, $t = [0.90 \rightarrow 1.00]$ s, and $t = [1.10 \rightarrow 1.20]$ s. These modes are not present during the last NBH pulse at $t = [1.40 \rightarrow 1.50]$ s, most likely due to the modifications of the current profile due to the combined EC and NB current-drive.

During the first 3 NBH pulses, the signal amplitude measured with the LTCC-3D sensors is $\delta B_{POL} \sim [2 \pm 0.3]$ mG and $\delta B_{POL} \sim [0.7 \pm 0.1]$ mG for the modes in the TAE and EAE frequency range, respectively, increasing from $\delta B_{POL} \sim [1 \pm 0.2]$ mG and $\delta B_{POL} \sim [0.3 \pm 0.05]$ mG during the ohmic phase. Although there is a clear effect of the NBI fast ions on the amplitude of these instabilities, their identification as AEs is not yet conclusive, the main evidence coming from the slowly decreasing frequency, consistent with an increasing overall plasma density and elongation, and their dominant toroidal mode number $n = 0$, the latter evidence pointing to global AEs and not TAEs or EAEs. During the ohmic phase and before the ECH-X2 additional heating is switched-on, these modes appear to rotate in the electron diamagnetic drift direction, i.e., they have a sub-dominant (accounting for $\sim 1/3$ of the total energy content in the mode) positive toroidal mode number $n = +2$ for the standard negative current and toroidal magnetic field configuration of TCV. During the NBH pulses, the sub-dominant component slowly transition to a negative $n = -2$ toroidal mode number, i.e., the mode rotates in the ion diamagnetic drift direction, consistently with a large drive coming from the fast ions. All these point to coupling between Alfvén waves and the EM component of

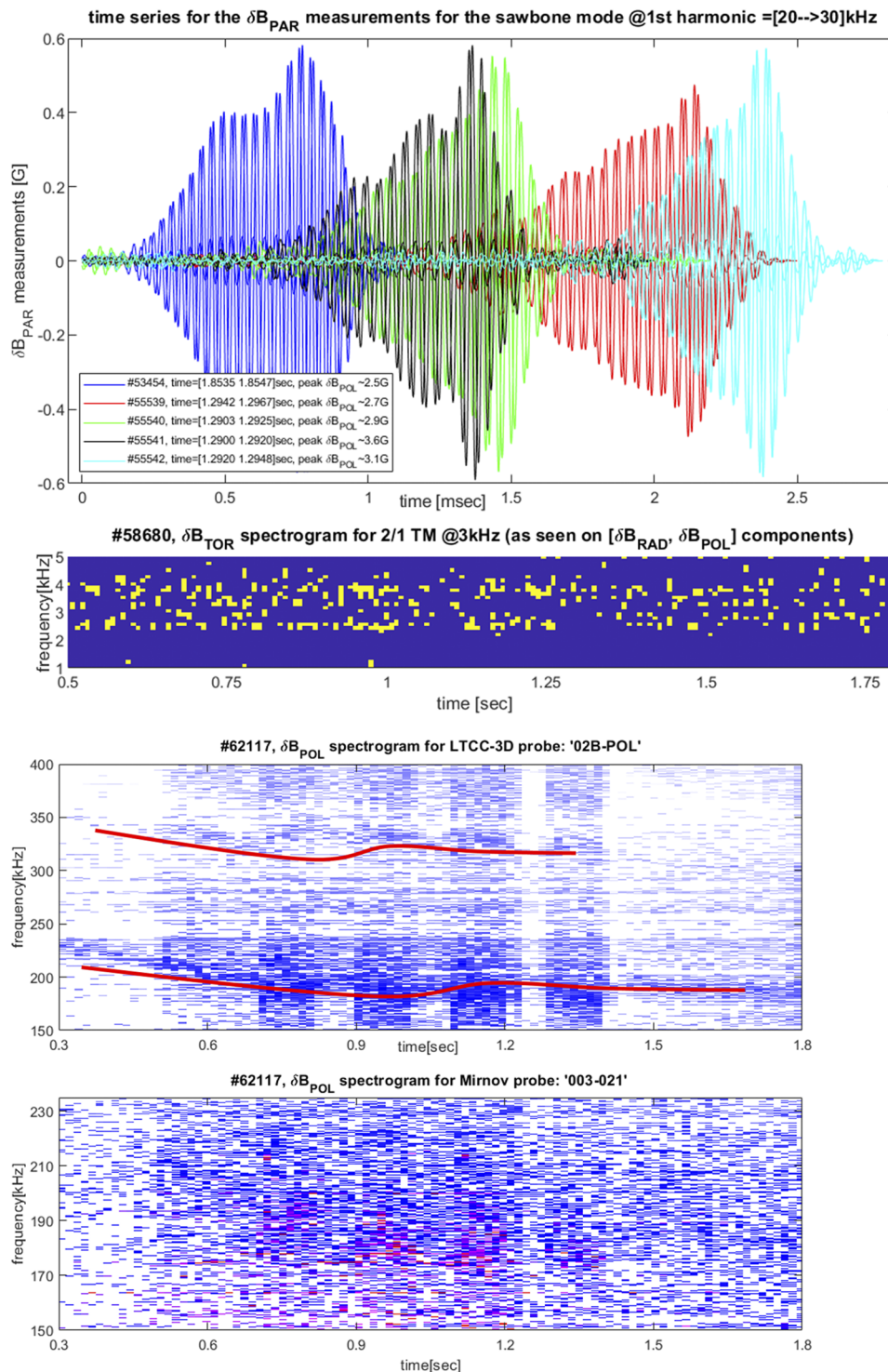


FIG. 23. (Top) Time series of some illustrative measurements of a finite δB_{PAR} component for the sawbone instability, in comparison with the absence of such a finite δB_{PAR} component for the 2/1 TM shown in Fig. 22. (Bottom) The spectrogram only shows uncorrelated pixels. For the sawbone instability at the first harmonic in the frequency range [20 → 30] kHz, we typically measure a ratio $\delta B_{PAR}/\delta B_{POL} \approx [0.10 \rightarrow 0.20]$ for the peak signal in the time series.

FIG. 24. High frequency δB_{POL} measurements obtained in No. 62117, where weak modes in the TAE frequency range @ ~180 kHz and even weaker in the EAE range @ ~350 kHz were observed (a red line is added to the spectrogram just below the modes' frequency to guide the eye for an easier identification). The two frames show the δB_{POL} spectrogram for the LTCC-3D sensor in sector 02B (top) and for the close-by Mirnov sensor 003-021 (bottom), the color coding being the same to allow for an easier comparison of the signal intensity. The mode at ~180 kHz should, in principle, have been detected by the Mirnov sensors but is actually not: in this example, the S/N ratio is too poor, and the mode is completely swamped by the background noise in the Mirnov DAQ.

drift-Alfvén turbulence as the main drive for the modes in the ohmic + ECH phase of the discharge.⁴⁹ Note that in this discharge, the Mirnov DAQ was running @500 kHz (the maximum available sampling rate), and therefore, only the modes in the TAE range could

have been observed. This, however, is not the case even with a DAQ DC gain 30× higher than that for the LTCC-3D sensors. In the bottom frame of Fig. 26, the spectrogram for a Mirnov sensor does not show any clear signal at ~180 kHz, consistently with an end-to-end

system sensitivity that is much smaller and rapidly decreasing with the frequency, as previously illustrated in Fig. 7, and a deteriorating CMRR for increasing frequency, as shown in Fig. 16. Hence, the mode's signal is completely swamped by the background noise.

Measurements of Alfvén eigenmodes in the few hundred kHz range is not a particularly new result: what, on the other hand, is new with these measurements is the determination of the actual amplitude of these modes in physical units with error bars, something which can only be obtained after going through all the steps described in Secs. IV–VII and the [supplementary material](#).

D. Power-law spectrum for high frequency fluctuations in the δB_{POL} spectrum, not measurable with Mirnov probes

As a final illustrative example of the data that can be obtained with the LTCC-3D sensors and that could have not been otherwise obtained with the Mirnov sensors, we can now look at the incoherent components in the δB_{POL} frequency spectrum picked-up by the LTCC-3D and Mirnov sensors.

The LTCC-3D system has been developed for MHz capabilities in view of forthcoming experiments where such magnetic fluctuations could be present. These not only include discrete eigenmodes, with high toroidal mode numbers up to $|n| \sim 20$, which may or may not exist depending on the operating scenario (and currently in TCV, discrete eigenmodes are observed only up to ~ 400 kHz with $|n|$ up to ~ 6), but most importantly EM broadband fluctuations, which are always there and are believed, based on the predictions for JET, TCV, ITER, and DEMO,^{21–30} and earlier measurements from the JET DTE1 experiment^{31,32} to significantly affect (and be affected by, with very important ensuing consequences on overall particles and heat transport mechanisms) fast ion confinement and overall turbulent transport mechanisms in certain regimes.

Therefore, in order to progress with quantitative analyses and calculations on this topic, it has now become of primary importance to provide absolute measurements and related error-bars also for the relevant quantities describing these broadband EM turbulent fields, namely, amplitude, power law scaling exponents, and spectral breaks, something that was not at all considered in previous experimental work on high-frequency magnetic fluctuations. Additionally, the fact that currently in TCV, we do not observe discrete eigenmodes or spectral breaks in the continuum spectrum for frequencies above ~ 400 kHz does not mean that we will not observe them later. The correct detection of all these features is therefore tested using the simulated data, as demonstrated in the [supplementary material](#) (Sec. I and specifically Figs. S40–S48).

An illustrative example using actual measurements is shown in Fig. 25 for No. 55542, where we plot the PSD-AR spectrum obtained using a rather low order $\text{AR} = 20$ to highlight the background component and its possible spectral break(s) while reducing the sensitivity to the individual coherent eigenmodes. Three different phases in this discharge are compared, respectively, before vs during vs after the NBH time window. We immediately note that the higher-frequency components of the signal picked-up by the Mirnov sensor are typically higher than those measured by the LTCC-3D sensors. Note also that the difference is further increasing with the frequency. Together with the sawbone analysis presented in Fig. 20, this was probably one of the first results that had prompted the investigation of the EM noise pick-up previously mentioned, leading to the results presented in Fig. 21.

Considering now the frequency spectrum measured by the LTCC-3D sensors, we note the presence of two clear spectral breaks, at around 10 kHz and 100 kHz before and after the NBH phase, but only one spectral break at around 20 kHz during the NBH phase. The corresponding power law indices are $\alpha_1 \sim -1.69 \pm 0.15 \approx -5/3$ between [10 kHz \rightarrow 100 kHz] and $\alpha_2 \sim -4.10 \pm 0.36$ between

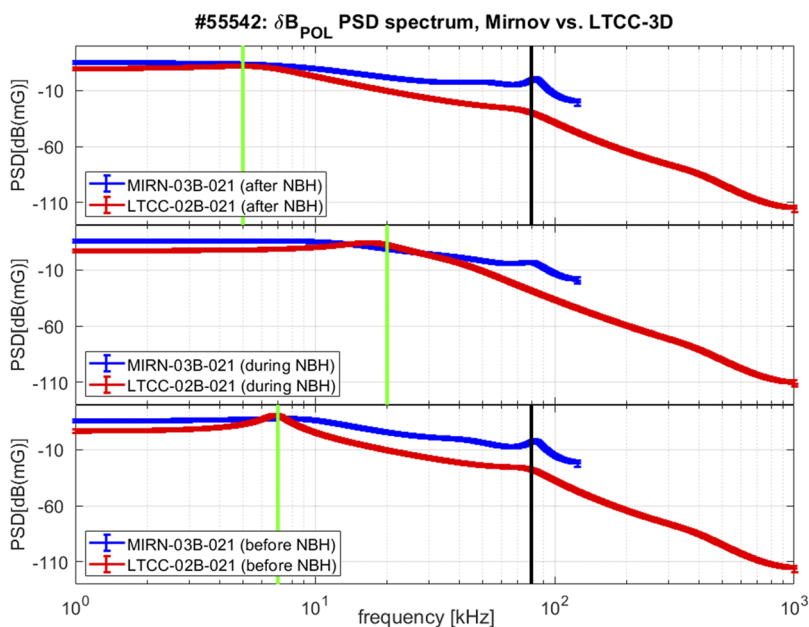


FIG. 25. The PSD-AR spectrum for No. 55542, comparing the three phases before/during/after the NBH time window: orderAR = 20 is used to highlight the background component and its possible spectral break(s). Clear spectral breaks are seen in the LTCC-3D data at around 10 kHz and 100 kHz before/after and at around 20 kHz during the NBH phase.

[100 kHz \rightarrow 1 MHz], respectively, with very similar values before and after the NBH phase, while $\alpha \sim -3.38 \pm 0.45$ during the NBH phase and for super-Alfvénic fluctuations. The value of the power law index α and its error $\sigma(\alpha)$ are, respectively, the rms and STD results over the $3 \times$ LTCC δB_{POL} measurements. For $\sigma(\alpha)$, we then also add the scatter determined using the propagation of error on the δB_{POL} measurements.

In the absence of NBH, we find the well-known value $\alpha_1 \approx -5/3$,⁵⁰ which shows that also in complex tokamak plasmas as TCV, the incoherent broadband magnetic fluctuations follow the Kolmogorov scaling in the inertial regime, hence its underlying physics, up to the Alfvénic frequency range ~ 100 kHz in the purely ohmic heating phase. Had we considered the Mirnov data, the corresponding power law index would have been $\alpha_1 \sim -0.80 \pm 0.25$, rather close to pink noise. During the NBH phase, and for super-Alfvénic fluctuations in ohmic plasmas, the measured power-law index is typically much higher, in the range $\alpha \sim -[3.3 \rightarrow 4.5]$ depending on the details of the experiment, indicating that we are well in the dissipation regime.

As a final note, the direct measurement of power law indices $\alpha_1 \approx -5/3$ and $\alpha_2 \approx -[3.3 \rightarrow 4.5]$ supports the approximations made in Sec. VI A to simplify the evaluation of the mutual coupling term $V_{MEAS} \approx L_{MUT} dI_{MEAS}/dt$ between the different measurement axes, which then also leads to Eqs. (G3) and (G4) of the [supplementary material](#) (Sec. G) when using $V(\omega, t) \sim V_0(t)(\omega/\omega_0)^{-\alpha(\omega, t)}$.

E. Improved toroidal mode number resolution spectra for δB_{POL} when combining Mirnov and LTCC-3D sensors

The $3 \times$ LTCC-3D sensors measuring δB_{POL} sit at the same vertical position ($Z = -115$ mm) of $6 \times$ Mirnov sensors on the LFS, thus making up a set of $9 \times$ non-uniformly spaced sensors that can

be used for toroidal mode number analysis. The only caveat in this analysis option is that the LTCC-3D data must be decimated [or down-sampled, but less effective in this case: see the [supplementary material](#) (Sec. I) for details] at the much lower acquisition frequency of the Mirnov sensors (250 kHz or 500 kHz for the Mirnov compared to 2 MHz for the LTCC-3D sensors).

Figure 26 compares the spectral window (SW) for different configurations of TCV magnetic sensors measuring the high frequency δB_{POL} spectrum on the LFS. These configurations include at most 17 Mirnov sensors, of which 16 are toroidally equi-spaced and the 17th is not, as it sits exactly at the middle position between two of the equi-spaced ones. Due to the installation of the NBI system, two of the equi-spaced sensors on the LFS midplane (sitting at $Z = 0$) had to be moved down to the vertical position of the LTCC-3D sensors @ $Z = -115$ mm. Consequently, at the LFS-top and LFS-bottom positions ($Z = \pm 345$ mm, respectively), we still have the original $17 \times$ not-equi-spaced Mirnov sensors, while at the LFS-mid, we only have $15 \times$ not-equi-spaced and $8 \times$ equi-spaced Mirnov sensors.

The configuration that includes the $6 \times$ Mirnov and the $3 \times$ LTCC sensors does not have any problematic toroidal mode number $n_{PER} \neq 0$ such that $SW(@n_{PER}) = 1$, namely, an exact toroidal periodicity for which the corresponding spatial Nyquist value is $n_{NYQ} = n_{PER}/2$, or any *bad* toroidal mode number n_{BAD} such that $SW(@n_{BAD}) > 0.85$, i.e., for which detection is seriously compromised.^{19,51,52} In principle, this allows detecting much higher n 's. This configuration has, however, a larger spectral noise content $SW > 0.25$ for certain toroidal mode numbers, which somewhat decreases the accuracy in the detection of the corresponding modes' amplitudes. All possible combinations of Mirnov-only sensors do have, on the contrary, various occurrences of problematic toroidal mode numbers n_{PER} and n_{BAD} , at $|n| = 8$ and $|n| = 16$ and their integer multiples, which effectively limits the toroidal mode number

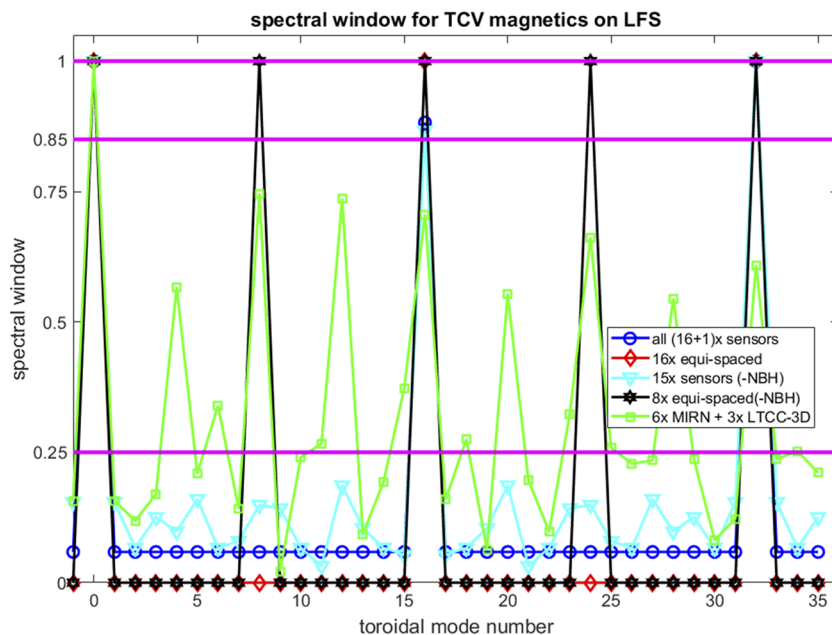


FIG. 26. The spectral window for different configurations of TCV magnetic sensors measuring the high frequency δB_{POL} spectrum on the LFS (see the main text for the corresponding nomenclature). The horizontal lines at $SW = 1$, $SW = 0.85$, and $SW = 0.25$ indicate the exact periodicity, bad detection, and intrinsic spectral noise limits, respectively.

TABLE V. Comparison of the measured and simulated mode amplitudes and toroidal mode numbers using two of the toroidal arrays in Fig. 26, namely, the $6 \times$ LTCC + $3 \times$ MIRN at $Z = -115$ mm (labeled LTCC) and the poloidally close-by $15 \times$ Mirnov sensors in the LFS-MID array (MIRN). The first five rows correspond to actual measurements; the last three rows show data from simulations similar to those in Sec. VII C and in the supplementary material (Sec. I).

Freq (kHz)	$\sigma(\text{freq})$ (kHz)	LTCC: δB_{POL} (mG)	LTCC: $\sigma(\delta B_{\text{POL}})$ (mG)	MIRN: δB_{POL} (mG)	MIRN: $\sigma(\delta B_{\text{POL}})$ (mG)	n_{TOR} LTCC vs MIRN
5.35	1.12	30.23	3.45	33.78	2.87	2 vs 2
25.16	3.45	104.65	7.56	112.09	10.84	1 vs 1
75.88	6.34	2.35	1.67	3.82	3.23	3 vs 3
180.98	7.23	3.24	1.45	4.15	2.71	2 vs 2
220.33	8.76	1.34	0.45	1.87	1.12	4 vs 4
180.00	5.00	4.67	0.68	5.12	1.27	Sym. input = 6 Sym. out: 6 vs 6
220.00	5.00	5.83	1.04	6.43	1.33	Sym. input = 12 Sym. out: 12 vs 11
220.00	5.00	6.12	1.57	4.54	1.87	Sym. input = 15 Sym. out: 15 vs 17

detection on the LFS to $|n| \leq 8$. These configurations have $SW < 0.25$ for all other toroidal mode numbers $1 \leq |n| \leq 7$, i.e., detection of the corresponding mode amplitudes is, in principle, more accurate.

Although representing, in principle, a clear improvement on the possibility of higher toroidal mode number detection, the configuration using the $6 \times$ Mirnov and the $3 \times$ LTCC-3D sensors sitting at $Z = -115$ mm is seldom used, and mostly only for verification purposes, essentially because so far we have seen no evidence on TCV of coherent modes with $|n| \geq 8$.

This, however, may not be the case in future TCV experiments due to the forthcoming installation of a higher energy NBH source and to scenario developments toward non-monotonic q-profiles. We argue that it is therefore of value to have already tested successfully the possibility of detecting such higher- $|n|$ modes using real and simulated data. The results of this analysis are shown in Table V. We find that only when accounting for all sources of EM noise (which is a very cumbersome procedure), agreement in δB_{POL} and $|n| \leq 6$ for actual measurements is satisfying. For the simulated data, hence immune from the different sources of EM noise, agreement in δB_{POL} is still good, while there are clear differences for frequencies > 200 kHz and an input $|n| > 10$ for the simulated data.

IX. CONCLUSIONS AND LESSONS LEARNT

The development of the LTCC-3D magnetic diagnostic system in TCV, which we carried over from designing and producing in-house the actual sensor to comparing different algorithms for mode detection, has given us the opportunity for completely testing anew, namely, not having to comply with the previous approaches, multiple aspects for improving and evaluating the end-to-end system measurement performance for high-frequency instabilities. Although very time consuming, this is a path that we believe should be taken for all further developments of magnetic diagnostics for high-frequency fluctuation measurements, if innovative and real quantitative insights that could advance our theoretical and

operational understanding of fusion plasmas are to be obtained from the data.

There were three main goals that we set up for this project—(a) essentially technical: manufacturing sensors with yields and reproducibility comparable to the best industrial standards and with electrical properties well-predicted by our design tools; (b) technical/scientific: optimize the different system's components so as to increase as much as possible the end-to-end system measurement performance for frequencies > 100 kHz, with a target bandwidth of 1 MHz; (c) scientific: develop and test algorithms for data processing so as to make the best possible use of the technical results. Our success in achieving these three separate goals is summarized below.

A. Manufacturing sensors with yields and reproducibility comparable to the best industrial standards and with electrical properties well-predicted by our design tools

The overall manufacturing yields for our LTCC-3D sensors are very good, comparable to the best industrial standards. For the alumina substrate, we achieved a 100% success rate, with 18/18 fully functioning modules. For the LTCC-1D modules, we achieved an overall production yield of 97.25%, with 354/364 fully functioning modules, including two different designs.

Regarding the main electrical properties (R_{SELF} , L_{SELF} , N_{Aeff}), for the alumina substrate and using the statistics on all 18 functioning modules, we have the design vs calculated vs measured values: $R_{\text{SELF}}[\Omega] = [15.00 \text{ vs } 17.45 \pm 0.32 \text{ vs } 16.84 \pm 0.17]$, $L_{\text{SELF}}[\mu\text{H}] = [7.60 \text{ vs } 7.48 \pm 0.91 \text{ vs } 7.79 \pm 0.10]$, and $N_{\text{Aeff}}[\text{cm}^2] = [215.00 \text{ vs } 209.54 \pm 3.45 \text{ vs } 210.07 \pm 3.14]$. The data agree with the estimates provided by the rectangular model for this circuit ($R_{\text{SELF}} = 17.10 \Omega$, $L_{\text{SELF}} = 8.03 \mu\text{H}$, $N_{\text{Aeff}} = 217.17 \text{ cm}^2$). For the LTCC-1D modules used for the final sensor (the V2 design), using the statistics on all 329 functioning modules, we have $R_{\text{SELF}}[\Omega] = [10.00 \text{ vs } 8.78 \pm 1.22 \text{ vs } 8.93 \pm 0.74]$, $L_{\text{SELF}}[\mu\text{H}] = [13.00 \text{ vs } 12.19 \pm 0.51 \text{ vs } 12.52 \pm 0.14]$, and $N_{\text{Aeff}}[\text{cm}^2] = [30.00 \text{ vs } 33.29 \pm 0.56 \text{ vs } 29.30 \pm 0.32]$. The data agree with the estimates from the elliptical model for this

circuit ($R_{\text{SELF}} = 9.40 \, \Omega$, $L_{\text{SELF}} = 12.55 \, \mu\text{H}$, $N A_{\text{EFF}} = 29.65 \, \text{cm}^2$). The reproducibility and agreement with the design specs and estimated model values is also very good, but this demanded the development of a non-trivial mathematical approach that includes terms such as distributed capacitances, partial inductances, and the solenoid filling factor. We conclude that our first, essentially technical, goal has been completely achieved, and this gives confidence in the ability to produce LTCC-1D sensors satisfying the very strict manufacturing tolerances that are requested by ITER for its LTCC-1D sensors, currently being procured.

B. Technical/scientific: Optimize the different system's components so as to increase as much as possible the end-to-end system measurement performance for frequencies >100 kHz, with a target bandwidth of 1 MHz

This has been a much more complex, and time consuming, goal to achieve, as it required testing different solutions for the assembly and on-board wiring for the final LTCC-3D sensors, for the electrical connection and brazing of the in-vessel cables onto the sensor, for the selection of the ex-vessel cabling, and finally for the optimization of the DAQ. A careful implementation of the on-board wiring and assembly of the LTCC-1D modules onto the alumina substrate was paramount to reduce the mutual and parasitic coupling between the three measurement axes. None of the individual steps mentioned above is solely on its own increasing the resonance frequency, hence the measurement bandwidth, by hundreds of kHz, but it is the sum of the incremental contributions of each one of them that does that. It is clear that only by optimizing, with a very time consuming process, all these different elements we were able to achieve an end-to-end bandwidth sufficiently close to our target value of 1 MHz, with an end-to-end system sensitivity that only starts deteriorating for frequencies >850 kHz. There are, however, two weak points that still need to be addressed: (a) what can be done to improve the electrical connection between the sensor-embedded winding pack and the in-vessel cabling, and (b) is a single 3D sensor really more useful than $3 \times 1\text{D}$ sensors.

Regarding (a), the solution that we have implemented to thermally decouple the in-vessel wiring from the ceramic sensor during the hot-brazing, with long and thin connection bars inserted into a ceramic holder and bonding using a glass paste, is clearly non-optimal, and indeed, ITER is looking at different approaches involving cold brazing (such as electron-beam welding). There is still a lot of work to find an optimized and very reproducible method to perform this electrical connection.

Regarding (b), the main drive behind a single 3D sensor is that the very small LTCC-1D modules need a base to be mounted onto for in-vessel installation, and therefore, why not use this base to provide an additional measurement axis? Then, from a 2D sensor, it seemed at the time a logical step to move directly to a 3D sensor, essentially *because we could make it just as easily*. However, it turns out that the extended overall surface of the sensor and the more complex parasitic and mutual coupling between the 3D axes are problematic for the data analysis, and this requires a much larger effort to be implemented sufficiently correctly. We believe that a more effective solution for the combined multi-D measurements would be simply developing $2 \times$ LTCC-2D sensors, with a base

providing the δB_{RAD} measurements and a second axis for the δB_{POL} and δB_{TOR} measurements, separately, the disadvantage being that we would now need four pairs of output wires and not three, hence more connections to be made available at the feedthrough and more DAQ channels.

Overall, we conclude that our second goal has been achieved, with some further work still needed, particularly in view of manufacturing and in-vessel assembly of the LTCC-1D sensors for ITER.

C. Scientific: Develop and test algorithms for data processing so as to make the best possible use of the technical results—3D measurements and high frequency

There are essentially four main new data processing steps that we have developed to make the best possible use of the LTCC-3D sensors. Essentially, what we believe to be missing from magnetic data for high frequency fluctuations is a meaningful estimate of the mode amplitude, provided with a reliable error analysis so that codes that use this value to infer anomalous transport coefficients can be better constrained with experimental values. This is important, as shown for the sawbone,⁴¹ when the mode radial eigenfunction is constructed combining through cross-correlation analyses the magnetic measurements at the LCFS with internal fluctuation data so as to obtain its absolute value across the plasma cross section. As a counter-example, the main weakness of the approach presented in Refs. 31 and 32 to explain the anomalous ion heating observed in the JET DTE1 experiments of 1997 through the suppression by fusion-born alpha particles of the ion temperature gradient turbulence is exactly the lack of such quantitative cross-correlation measurements, which prevents providing the radial profile of these fluctuations with the corresponding eigenfunction in physical units.

To achieve the goal of providing a meaningful estimate of the mode amplitude using the LTCC-3D measurements, we need first to account for the mutual and parasitic coupling between the different measurement axes, and this also includes the removal of the low-frequency signal components associated with the pick-up of the equilibrium magnetic field. Second, we need to consider the projection of the measurement from wall-aligned to field-aligned components as a function of the geometry of the LCFS and the sensor's orientation. Third, we need to develop a correct tracking of the errors coming from the different steps in the data analysis so that the final results on the mode amplitude are meaningful with reliable errors. Finally, we want to check the measurement capabilities, and thus, we need to build an algorithm to test the correct detection of modes in the presence of noise and including the effect of inverting the measurement of the continuous analog end-to-end transfer function into the discretized digital calibration up to the Nyquist frequency.

All these steps have been quite challenging to develop mathematically and implement numerically but have led to a number of general results that we suggest should be used for all high frequency magnetic diagnostics, not just our LTCC-3D system. First, the end-to-end calibration is essential for estimating correctly the mode amplitude (with errors): in this specific context, the bilinear digital calibration method is only applicable for frequencies

$\ll f_{sDAQ}/\pi$. Second, tracking the frequency-dependence of the end-to-end measurement errors is essential, as different sources of errors have a different frequency spectrum. Third, knowing the color of the diagnostic noise, the contribution of the CMRR, and the overall level of EM noise pick-up is essential to discriminate between and account for different sources of the input voltage measurement. This then helps when simulating the end-to-end system performance. Fourth, mode detection through a PSD is only an estimator, and as such, its accuracy bounds need to be carefully established. In particular, in the latter context, there are very clear differences in the results when comparing analyses using the PSD-AR with the FFT and other periodogram-based PSD methods: the PSD-AR approach is generally superior for detecting modes.

The mathematical development and implementation of all these steps have led to verifying the LTCC-3D δB_{POL} data with the corresponding Mirnov data and then to obtaining measurements that could have not been otherwise obtained for the δB_{POL} and the other two $\{\delta B_{RAD}, \delta B_{TOR}\}$ measurement components. Therefore, we conclude that our third goal regarding 3D measurements of magnetic fluctuations has also been fully achieved using actual data. Regarding the MHz capabilities, in TCV, currently we do not observe discrete eigenmodes or spectral breaks in the continuum spectrum for frequencies above ~ 400 kHz, but this does not mean that we will not observe them later. The correct detection of all these features is therefore tested using the simulated data, as demonstrated in the [supplementary material](#) (Sec. I): this then proves that our third goal regarding high frequency results has also been achieved.

SUPPLEMENTARY MATERIAL

This work is intended essentially as a practical tutorial for our younger colleagues on how to build such a diagnostic system, capable of providing quantitative measurements of magnetic fluctuations, in general, in absolute units and with error bars, up to the ~ 1 MHz range. While it is obvious that some elements are really and only TCV-specific most are not, and it is expected that the latter will provide the intended guidance. To achieve this goal, a lot of materials need to be shown, and the majority of these elements are described here. See the [supplementary material](#) for the design and manufacturing of the LTCC-3D magnetic sensors (Sec. A), the in-vessel sensor installation (Sec. B), the installation of the ex-vessel cabling up to the front-end electronics (Sec. C), the data acquisition electronics (Sec. D), the electrical characterization of the sensors (Sec. E), the comparison between different calibration methods (Sec. F), the mutual and parasitic coupling calculations (Sec. G), the transformation between wall-aligned to field-aligned magnetic field components (Sec. H), and the algorithm for simulating mode detection (Sec. I).

ACKNOWLEDGMENTS

This work has been carried out within the framework of the EUROfusion Consortium and has received funding from the Euratom research and training program 2014–2018 and 2019–2020 under Grant Agreement No. 633053. The views and opinions expressed herein do not necessarily reflect those of the European

Commission. This work was also partly supported by the Swiss National Science Foundation. The author would like to thank the contribution of the TCV team for their support to this project. The author is particularly indebted to M. Toussaint, R. Chavan, and J. B. Lister of the Swiss Plasma Center at the EPFL for their contribution to the initial development of the LTCC concept and to A. Corne, C. Jacq, T. Maeder, B. Ellenrieder, M. Stoeck, G. Farine, Y. Fournier, and M. Garcin of the EPFL Laboratoire de Production Microtechnique for their contribution to the final design and manufacturing of the LTCC-3D sensors. A number of colleagues from the TCV services have helped in the installation of the LTCC-3D sensors and the design and installation of the related DAQ: S. Antonioni, S. Couturier, F. Dolizy, P. Lavanchy, T. Leresche, X. Llobet, B. Marletaz, P. Marmillod, C. Moura, and U. Siravo. Finally, various students have contributed to this work during their time at the EPFL: L. Blondel, L. Perrone, and L. Stipani (SPC-EPFL), A. Iantchenko (exchange student from Chalmers University of Technology, 41296 Goteborg, Sweden), A. Tolio (exchange student from Politecnico di Milano, 20133 Milano, Italy), and P. Windischhofer (exchange student from Technical University of Wien, 1040 Wien, Austria). Finally, the author would also like to thank the reviewers for helping focusing the presentation toward a more user-friendly content.

DATA AVAILABILITY

The data that support the findings of this study are available from the corresponding author upon reasonable request.

REFERENCES

- ¹Y. Imanaka, *Multilayered Low Temperature Cofired Ceramics (LTCC) Technology*, Hardcover (Springer, 2004), ISBN: 0-387-23130-7.
- ²D. Testa, R. Chavan, J. Guterl, J. B. Lister, J.-M. Moret, A. Perez, F. Sanchez, B. Schaller, G. Tonetti, M. Toussaint *et al.*, “The magnetic diagnostic set for ITER,” in *Proceedings 23rd IEEE/NPSS Symposium on Fusion Engineering (SOFE 2009 Conference)*, San Diego, USA (IEEE Xplore, 2009).
- ³D. Testa, R. Chavan, J. Guterl, J. B. Lister, J.-M. Moret, A. Perez, F. Sanchez, B. Schaller, G. Tonetti, M. Toussaint *et al.*, “Baseline system design and prototyping for the ITER high-frequency magnetic diagnostics set,” in *Proceedings 23rd IEEE/NPSS Symposium on Fusion Engineering (SOFE 2009 Conference)*, San Diego, USA (IEEE, 2009).
- ⁴D. Testa, H. Carfantan, M. Toussaint, R. Chavan, Y. Fournier, J. Guterl, J. B. Lister, T. Maeder, J.-M. Moret, A. Perez *et al.*, “Assessment of the ITER high-frequency magnetic diagnostic set,” in *Proceedings 26th Symposium on Fusion Technology (SOFT 2010 Conference)*, Porto, Portugal, 27 September–1 October 2010 [*Fusion Eng. Des.* **86**, 1149 (2011)].
- ⁵M. Toussaint, D. Testa, N. Baluc, R. Chavan, Y. Fournier, J. B. Lister, T. Maeder, P. Marmillod, F. Sanchez, and M. Stöck, “Design of the ITER high-frequency magnetic diagnostic coils,” in *Proceedings 26th Symposium on Fusion Technology (SOFT 2010 Conference)*, Porto, Portugal, 27 September–1 October 2010 [*Fusion Eng. Des.* **86**, 1248 (2011)].
- ⁶D. Testa, Y. Fournier, T. Maeder, M. Toussaint, R. Chavan, J. Guterl, J. B. Lister, J.-M. Moret, B. Schaller, and G. Tonetti, “Prototyping a high frequency inductive magnetic sensor using the non-conventional, low temperature co-fired ceramics technology for use in ITER,” *Fusion Sci. Technol.* **59**(2), 376–396 (2011), URL: <http://epubs.ans.org/?a=11653>.
- ⁷Private communication from personnel from Fusion for Energy, Barcelona, Spain, and the ITER Organization, Cadarache, France.
- ⁸S. Coda, J. Ahn, R. Albanese, S. Alberti, E. Alessi, S. Allan, H. Anand, G. Anastassiou, Y. Andrébe, C. Angioni *et al.*, “Overview of the TCV tokamak program: Scientific progress and facility upgrades,” *Nucl. Fusion* **57**, 102011 (2017).

- ⁹G. Pucella, E. Alessi, L. Amicucci, B. Angelini, M. L. Apicella, G. Apruzzese, G. Artaserse, F. Belli, W. Bin, L. Boncagni *et al.*, "Overview of the FTU results," *Nucl. Fusion* **57**, 102004 (2017).
- ¹⁰C. Bourdelle, J. F. Artaud, V. Basiuk, M. Bécoulet, S. Brémond, J. Bucalossi, H. Bufferand, G. Ciraolo, L. Colas, and Y. Corre, "WEST physics basis," *Nucl. Fusion* **55**, 063017 (2015).
- ¹¹M. Baruzzo, A. Pironti, R. Albanese, R. Ambrosino, G. Artaserse, A. Castaldo, R. Cavazzana, C. Cianfarani, F. Crisanti, G. Marchiori *et al.*, *Conceptual Design of DTT Magnetic Diagnostics* (EPS, Milano, Italy, 2019).
- ¹²Private communication by personnel from Tokamak Energy LTD, a private UK company, <http://www.tokamakenergy.co.uk/>.
- ¹³Private communication by personnel from the European Space Agency and Swiss Space Center, framework program on European Space Technology Harmonisation.
- ¹⁴W. Biel, I. Bolshakova, I. Duran, D. Testa, E. Alessi, R. Ambrosino, M. Ariola, K. J. Brunner, M. Ceconello, S. Conroy *et al.*, "Overview on the development of the DEMO diagnostic and control system," Invited talk, 31th Symposium on Fusion Technology, Dubrovnik, Croatia, 20–25 September 2020.
- ¹⁵D. Testa, A. Corne, G. Farine, C. Jacq, T. Maeder, and M. Toussaint, "3D, LTCC-type, high-frequency magnetic sensors for the TCV tokamak," in Proceedings 28th Symposium on Fusion Technology (SOFT 2014 Conference), San Sebastian, Spain, 29 September–3 October 2014 [*Fusion Eng. Des.* **96–97**, 989–992 (2015)].
- ¹⁶D. Testa, A. Corne, C. Jacq, T. Maeder, M. Toussaint, S. Antonioni, R. Chavan, S. Couturier, F. Dolizy, P. Lavanchy *et al.*, "LTCC magnetic sensors at EPFL and TCV: Lessons learnt for ITER," in Proceedings 30th Symposium on Fusion Technology (SOFT 2018 Conference), Giardini Naxos, Italy, 16–21 September 2018.
- ¹⁷A. N. Karpushov, R. Chavan, S. Coda, V. I. Davydenko, F. Dolizy, A. N. Dranitschnikov, B. P. Duval, A. A. Ivanov, D. Fasel *et al.*, "Neutral beam heating on the TCV tokamak," in 29th Symposium on Fusion Technology (SOFT 2016 Conference), Prague, Czech Republic, 5–9 September 2016 [*Fusion Eng. Des.* **123**, 468 (2017)].
- ¹⁸J.-M. Moret, F. Buhlmann, D. Fasel, F. Hofmann, and G. Tonetti, "Magnetic measurements on the TCV tokamak," *Rev. Sci. Instrum.* **69**, 2333 (1998).
- ¹⁹D. Testa, H. Carfantan, M. Albergante, P. Blanchard, S. Bourguignon, A. Fasoli, A. Goodyear, A. Klein, J. B. Lister, and T. Panis, "Sparse representation of signals: From astrophysics to real-time data analysis for fusion plasmas and system optimization analysis for ITER and TCV," *Plasma Phys. Controlled Fusion* **58**, 123001 (2016), topical review paper.
- ²⁰W. W. Heidbrink, E. D. Fredrickson, T. K. Mau, C. C. Petty, R. I. Pinsker, M. Porkolab, and B. W. Rice, "High harmonic ion cyclotron heating in DIII-D: Beam ion absorption and sawtooth stabilization," *Nucl. Fusion* **39**, 1369 (1999).
- ²¹M. Albergante, J. P. Graves, A. Fasoli, F. Jenko, and T. Dannert, "Anomalous transport of energetic particles in ITER relevant scenarios," *Phys. Plasmas* **16**, 112301 (2009).
- ²²M. Albergante, J. P. Graves, A. Fasoli, and X. Lapillonne, "Microturbulence driven transport of energetic ions in the ITER steady-state scenario," *Nucl. Fusion* **50**, 084013 (2010).
- ²³M. Albergante, J. P. Graves, A. Fasoli, M. Jucker, X. Lapillonne, and W. A. Cooper, "Numerical modelling of electromagnetic turbulent transport of energetic ions in burning plasmas," *Plasma Phys. Controlled Fusion* **53**, 054002 (2011).
- ²⁴M. Albergante, J. P. Graves, A. Fasoli, S. Brunner, and W. A. Cooper, "Assessment of turbulent beam ion redistribution in tokamaks through velocity space-dependent gyrokinetic analyses," *Nucl. Fusion* **52**, 094016 (2012).
- ²⁵G. J. Wilkie, I. G. Abel, M. Landreman, and W. Dorland, "Transport and deceleration of fusion products in microturbulence," *Phys. Plasmas* **23**, 060703 (2016).
- ²⁶A. Di Siena, T. Görler, H. Doerk, E. Poli, and R. Bilato, "Fast ion stabilization of tokamak plasma turbulence," *Nucl. Fusion* **58**, 054002 (2018).
- ²⁷N. Bonanomi, P. Mantica, A. Di Siena, E. Delabie, C. Giroud, T. Johnson, E. Lerche, S. Menmuir, M. Tsalas, D. Van Eester *et al.*, "Turbulent transport stabilization by ICRH minority fast ions in low rotating JET ILW L-mode plasmas," *Nucl. Fusion* **58**, 056025 (2018).
- ²⁸J. Garcia, T. Görler, and F. Jenko, "Isotope and fast ions turbulence suppression effects: Consequences for high- β ITER plasmas," *Phys. Plasmas* **25**, 055902 (2018).
- ²⁹A. Di Siena, T. Görler, E. Poli, A. B. Navarro, A. Biancalani, and F. Jenko, "Electromagnetic turbulence suppression by energetic particles driven modes," *Nucl. Fusion* **59**, 124001 (2019).
- ³⁰A. Di Siena, T. Görler, E. Poli, R. Bilato, H. Doerk, and A. Zocco, "Resonant interaction of energetic ions with bulk-ion plasma micro-turbulence," *Phys. Plasmas* **26**, 052504 (2019).
- ³¹D. Testa and M. Albergante, "A phenomenological explanation for the anomalous ion heating observed in the JET alpha heating experiment of 1997," *Nucl. Fusion* **52**(8), 083010 (2012).
- ³²D. Testa and M. Albergante, "Evidence for a new path to the self-sustainment of thermonuclear fusion in magnetically confined plasmas," *Europhys. Lett.* **97**, 35003 (2012).
- ³³D. Testa, M. Toussaint, R. Chavan, A. Encheva, J. B. Lister, J. M. Moret, and F. Sanchez, "Prototyping conventional wound high frequency magnetic sensors for ITER," *Fusion Sci. Technol.* **61**(1), 19–50 (2012), URL: <http://epubs.ans.org/?a=13337>.
- ³⁴R. McCarty, *IEEE Trans. Magn.* **15**(6), 1494 (1979).
- ³⁵R. F. Heeter, A. F. Fasoli, S. Ali-Arshad, and J. M. Moret, "Fast magnetic fluctuation diagnostics for Alfvén eigenmode and magnetohydrodynamics studies at the Joint European Torus," *Rev. Sci. Instrum.* **71**, 4092 (2000).
- ³⁶E. C. Levi, "Complex-curve fitting," *IRE Trans. Autom. Control* **AC-4**, 37 (1959).
- ³⁷J. E. Dennis and R. B. Schnabel, *Numerical Methods for Unconstrained Optimization and Nonlinear Equations* (Prentice-Hall, 1983).
- ³⁸M. Abramowitz and I. A. Stegun, *Handbook of Mathematical Functions*, 9th ed. (Dover Publications, New York, USA, 1970); see Eq. (4.1.27), p. 68.
- ³⁹L. B. Jackson, "A correction to impulse invariance," *IEEE Sig. Process. Lett.* **7**, 273 (2000).
- ⁴⁰W. W. Heidbrink, H. H. Duong, J. Manson, E. Wilfrid, and C. Oberman, "The nonlinear saturation of beam-driven instabilities: Theory and experiment," *Phys. Fluids B* **5**, 2176 (1993).
- ⁴¹L. Stipani, D. Testa, A. Fasoli, M. Fontana, A. Karpushov, C. Marini, A. Merle, and L. Porte, "Fishbone and de-trapping of fast ions during NBH discharges on TCV," in Proceedings 15th IAEA TCM on Energetic Particles, Princeton, USA, 5–8 September 2017.
- ⁴²L. Chen, R. B. White, and M. N. Rosenbluth, "Excitation of internal Kink modes by trapped energetic beam ions," *Phys. Rev. Lett.* **52**(13), 1122 (1984).
- ⁴³S. von Goeler, W. Stodiek, and N. Sauthoff, "Studies of internal disruptions and $m = 1$ oscillations in tokamak discharges with soft-X-ray techniques," *Phys. Rev. Lett.* **33**(20), 1201 (1974).
- ⁴⁴F. Hoffman and G. Tonetti, "Tokamak equilibrium reconstruction using Faraday rotation measurements," *Nucl. Fusion* **28**, 1871 (1988).
- ⁴⁵A. Favre, J.-M. Moret, R. Chavan, A. Elkjaer, D. Fasel, F. Hofmann, J. B. Lister, J.-M. Mayor, and A. Perez, "Fast power supply for vertical stabilization of TCV tokamak plasmas," in *CERN EP2 Forum 1995* (CERN publication services, 1995), Vol. ETG 43.
- ⁴⁶J.-M. Moret, "A software package to manipulate space dependencies and geometry in magnetic confinement fusion," *Rev. Sci. Instrum.* **76**, 073507 (2005).
- ⁴⁷J. P. Graves, D. Zullino, D. Brunetti, S. Lanthaler, and C. Wahlberg, "Reduced models for parallel magnetic field fluctuations and their impact on pressure gradient driven MHD instabilities in axisymmetric toroidal plasmas," *Plasma Phys. Controlled Fusion* **61**, 104003 (2019).
- ⁴⁸R. B. White, *The Theory of Toroidally Confined Plasma*, revised 2nd ed. (Imperial College Press, 2006), see Eq. (4.28), p. 104, and the minimization of δW , ISBN: 1-86094-639-9.
- ⁴⁹M. Maraschek, S. Günter, T. Kass, B. Scott, and H. Zohm, "Observation of toroidicity-induced Alfvén Eigenmodes in ohmically heated plasmas by drift-wave excitation," *Phys. Rev. Lett.* **79**, 4186 (1997).
- ⁵⁰A. N. Kolmogorov, "The local structure of turbulence in incompressible viscous fluid for very large Reynolds numbers," *Dokl. Akad. Nauk. SSSR* **30**(4) (1941) [translated and reprinted in *Proc. R. Soc. London*, **434**, 9–13 (1991)].
- ⁵¹D. Testa, H. Carfantan, R. Chavan, J. B. Lister, J.-M. Moret, and M. Toussaint, "Functional performance analysis and optimization for the high-frequency magnetic diagnostic system in ITER—Part 1," *Fusion Sci. Technol.* **57**(3), 208–237 (2010), URL: <http://epubs.ans.org/?a=9468>.

⁵²D. Testa, H. Carfantan, R. Chavan, J. B. Lister, J.-M. Moret, and M. Toussaint, “Functional performance analysis and optimization for the high-frequency magnetic diagnostic system in ITER—Part 2,” *Fusion Sci. Technol.* **57**(3), 238–273 (2010), URL: <http://epubs.ans.org/?a=9469>.

⁵³The following convention is used throughout this work to label the 3D $\delta\mathbf{B}$ measurements in field-coordinates: the parallel field component δB_{PAR} is aligned with the equilibrium magnetic field at the LCFS, namely, the component with the same pitch as the safety factor q at the LCFS (q_{LCFS}), which is effectively very close to the toroidal geometrical component δB_{TOR} for values of $q_{\text{LCFS}} > 2$ and a small aspect ratio tokamak $\epsilon = a/R_0 \sim 0.25$ (as TCV), since the equilibrium field is $B_{\text{POL}} < B_{\text{TOR}}$. The poloidal δB_{POL} and normal δB_{NOR} components are aligned onto the two directions orthogonal to the parallel one: these are then obtained from the geometrical δB_{VER} and δB_{RAD} measurements, respectively, using knowledge of the shape of the LCFS and of the position and orientation of the sensor as actually installed in-vessel.

⁵⁴Throughout this work, we use the following nomenclature for the parasitic and mutual coupling between the different measurement axes. The *parasitic* coupling is due to winding misalignment, creating a surface area on one axis that is capturing magnetic flux from (any of) the other two directions. The *mutual* coupling is due to the distributed structure of the 3D sensor that is then built-up into one single assembly so that a mutual inductance (and also a mutual capacitance, however, only important for very low frequency measurements) exists between the

different individual components. Additionally, the on-board wiring connecting all the different components of the LTCC-3D sensors up to the measurement output has to be added, as it produces both a parasitic and a mutual coupling.

⁵⁵This high sensitivity at high frequency is the reason for simply reducing the overall gain in the DAQ to avoid saturation, not using a complex filter to preserve the high-frequency response while reducing the overall signal amplitude.

⁵⁶The analog end-to-end direct $\text{TF}_{\text{DirE2E}}(s)$ converts the frequency-dependent voltage measured by the probe to the signal acquired at the end of the acquisition chain, which is then sampled at f_{sDAQ} and stored in the data repository.

⁵⁷The digital end-to-end inverse $\text{TF}_{\text{InvE2E}}(z)$ converts the signal stored in the MDS repository back to the actual time series for the magnetic field measured by the probe.

⁵⁸As it will become apparent later, the capacitive coupling is particularly important for the so-called *stray* and *back-off* shots, namely, when the individual coils providing the equilibrium magnetic field are activated in vacuum to test their operation. In this situation, the approach to the mutual coupling calculations presented here become ill-defined: most of the measured signals are actually $V_{\text{MEAS}} \approx (1/C_{\text{MUT,DC}}) \times \int I_{\text{MEAS}} dt$ but incorrectly interpreted as $V_{\text{MEAS}} \approx N A_{\text{EFF}} \times d\delta B_{\text{MEAS}}/dt$.

⁵⁹Here, we are using the Matlab notation for the functions *filter* and *filtfilt*.

⁶⁰This observation will be discussed in detail in a forthcoming contribution on the status of the TCV Mirnov probes.